Doctoral Dissertation
Politecnico di Torino
Doctoral Program in Electronics Engineering (29th Cycle)
Université Paris-Saclay
École doctorale Electrical, Optical, Bio-physics and Engineering
Spécialité Génie électrique

Design and integration of a dynamic IPT system for automotive applications

By

Vincenzo Cirimele

Supervisors:
Fabio Freschi, Associate Professor, Politecnico di Torino
Lionel Pichon, Directeur de Recherche, CNRS

Doctoral Examination Committee:
Christian Vollaire, Referee, Professeur des Universités, École centrale de Lyon
Piergiorgio Alotto, Referee, Associate Professor, Università degli studi di Padova
Adel Razek, Directeur de Recherche Emérite, CNRS
Michele Tartaglia, Full Professor, Politecnico di Torino
Nunzio Salerno, Associate Professor, Università degli studi di Catania

Politecnico di Torino
February 2017

Declaration

I hereby declare that, the contents and organisation of this dissertation constitute my own original work and does not compromise in any way the rights of third parties, including those relating to the security of personal data.

<div align="right">

Vincenzo Cirimele

February 2017

</div>

Abstract

Keywords: inductive power transfer, electric vehicles, recharge systems

Inductive power transmission (IPT) for electric vehicles (EVs) is a promising emergent technology that seems able to improve the electric mobility acceptance. In the last two decades many researchers have proved its feasibility and the possibility to use it to replace the common conductive systems for the charge of the on-board battery. Many efforts are currently aimed to extend the IPT technology towards its use for the charge during the vehicle motion. This application, commonly indicated as dynamic IPT, is aimed to overcome the limit represented by the long stops needed for the recharge introducing also the possibility of reducing the battery capacity installed on vehicle.

An IPT system is essentially based on the resonance of two magnetically coupled inductors, the transmitter, placed on or under the ground, and the receiver, placed under the vehicle floor. The typical operating frequency range for the EVs application goes from 20 kHz to approximately 100 kHz. The coupling between the two inductors takes place through a large air-gap, usually about 10-30 cm.

This thesis presents the results of the research activities aimed to the creation of a prototype for the dynamic IPT oriented to the private transport. Starting from an analysis of the state of the art and the current research projects on this domain, this work presents the development of a circuit model able to describe the electromagnetic phenomena at the base of the power transfer and the interface with the power electronics. This model provides the information at the base of the design and the implementation of a dedicated low cost-high efficiency H-bridge converter for the supply of the transmitter side. A general architecture of the power electronics that manages the receiver side is proposed together with the additional protection circuits. A methodology for the integrated design of the magnetic structure is illustrated covering the aspects of the matching with the power electronics, the integration on an existing vehicle and the installation on the road infrastructure. A series of activities aimed to the implementation of a dedicated test site are presented and discussed. In particular, the activities related to the creation of the electrical infrastructure and the issues and methods for the embedding of the transmitters in the road pavement are presented. The final goal is the creation of a dedicated IPT charging line one hundred

meters long. Finally, a methodology for the assessment of the human exposure is presented and applied to the developed solution.

Résumé

Mots-clés: transmission inductive, véhicules électriques, systèmes de recharge

La transmission inductive de puissance (IPT) pour les véhicules électriques est une technologie émergente prometteuse qui semble capable d'améliorer l'acceptation de la mobilité électrique. Au cours des deux dernières décennies, de nombreux chercheurs ont démontré la faisabilité et la possibilité de l'utiliser pour remplacer les systèmes conducteurs classiques pour la charge de la batterie à bord du véhicule. Actuellement de nombreux efforts visent à étendre la technologie IPT vers son utilisation pour la charge pendant le mouvement du véhicule. Cette application, généralement appelée IPT dynamique, vise à surmonter la limite représentée par les arrêts prolongés nécessaires pour la recharge introduisant également la possibilité de réduction de la capacité de la batterie installée à bord du véhicule.

Un système IPT est essentiellement basé sur la résonance de deux inducteurs magnétiquement couplés, l'émetteur, placé sur ou sous le sol, et le récepteur, placé sous le plancher du véhicule. La gamme de fréquence de fonctionnement typique pour les applications automobiles va de 20 kHz à environ 100 kHz. Le couplage entre les deux inductances s'effectue à travers un entrefer important, généralement d'environ 10-30 cm.

Cette thèse présente les résultats des activités de recherche visant à la création d'un prototype pour l'IPT dynamique orienté vers le transport privé. A partir d'une analyse de l'état de l'art et des projets de recherche en cours dans ce domaine, ce travail présente le développement d'un modèle de circuit capable de décrire les phénomènes électromagnétiques à la base du transfert de puissance et l'interface avec l'électronique de puissance. Les analyses effectuées à travers le modèle développé fournissent la base pour la conception et la mise en oeuvre d'un convertisseur dédié à faible coût et efficacité élevée pour l'alimentation du côté transmetteur. Une architecture générale de l'électronique de puissance qui gère le côté récepteur est proposée avec les circuits de protection supplémentaires. Une méthodologie pour la conception intégrée de la structure magnétique est illustrée. Cette méthodologie couvre les aspects de l'interface avec l'électronique de puissance, l'intégration sur un véhicule existant et l'installation sur l'infrastructure routière. Une série d'activités visant à la réalisation

d'un site d'essai dédié sont présentées et discutées. En particulier, les activités liées à la création de l'infrastructure électrique ainsi que les questions et les méthodes d'implantation des émetteurs dans le revêtement routier sont présentées. L'objectif final est la création d'une ligne de recharge IPT dédiée de 100 mètres de long. Enfin, une méthodologie d'évaluation de l'exposition humaine est présentée et appliquée à la solution développée.

Acknowledgements

Contents

List of Tables

List of Figures

Chapter 1

Introduction to the work

The "E-mobility Index", a study realised by fka and the Roland Berger Strategy Consultant [1], has analysed the current situation of the electro-mobility in the seven world leading automotive economies[1] pointing out as the share of electric cars of the market in each country is lower than 1%. Despite that, the trend is upward and more car manufacturers are introducing their electric models into the market. According to the report, Japan is the leader in electro-mobility penetration to the transportation market. This is thanks primarily to the lower cost of electric vehicles (EVs) and then to the more mature charging infrastructure. In fact, battery manufacturers in Japan and in South Korea dominate the entire battery production value chain resulting in a competitive advantage for these countries. In the U.S.A., the company Tesla Motors is trying to follow a similar approach by means of the creation of a "gigafactory" lithium-ion batteries which is expected to lower the production costs of 30% reducing hence the EVs cost [2].

These results distinctly indicates as the major barrier to the electro-mobility diffusion is the cost of the batteries. The economic aspect is accompanied by the important issue of the long time requested for the charge that makes the use of the electric vehicles not practicable on the long distances.

In Europe, the parliament of the Union, passed a resolution in 2013 that requires to the member states to install a specified number of electric vehicle charging stations by 2020. Germany has set its target to 86000, Italy will install 72000, and the UK is planning to build a minimum of 70000 EV recharging points [3]. These actions are related to the efforts of researchers and manufactures in the development of technologies able to reduce the charging time and simplify the daily use of the electric cars.

In addition to the plug-in systems for the recharge, the development of a series of market-ready products for the charge of electric vehicles without any electrical contact is ongoing. This technology is commonly indicated as wireless power transmission (WPT) or, more properly, inductive power transmission (IPT). A functional block

---

[1]These economies are China, France, Germany, Italy, Japan, Korea and the U.S.

diagram of an IPT system is depicted in Fig. 1.1. It consists basically in the inductive coupling of a coil fixed on or under the ground pavement, named transmitter, and a movable second one placed under the vehicle floor called receiver. The transmitter is powered through a power electronics converter providing a high-frequency current, the produced field links with the receiver allowing the transfer of electrical power. The receiver can be connected, by means of a rectification stage, to the battery of the vehicle allowing its charge. In general, auxiliary material are used to build a mechanical and magnetic structure for the coils. The resulting objects are frequently indicated as pads.
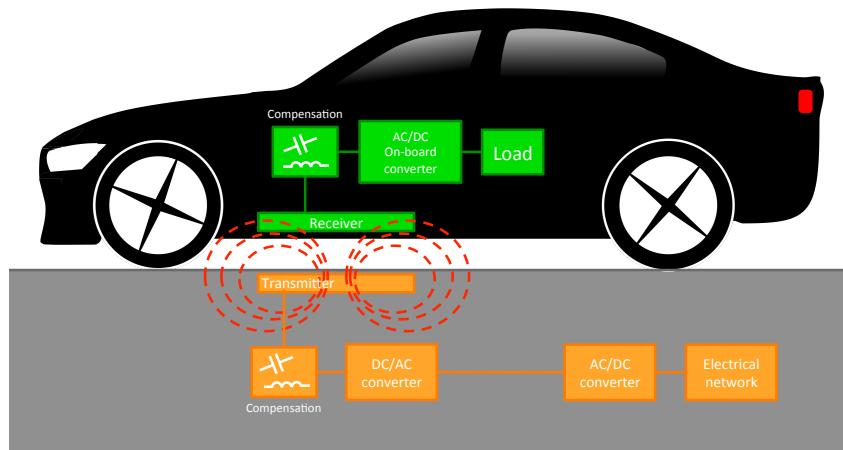
Figure 1.1: Scheme of the general components of an IPT system for electric vehicles

Thanks to the absence of electrical contacts, the two part of an IPT system can be independently enclosed without any requirements of external installations. The recharge process can be started automatically when the vehicle is over the transmitter without any human interaction with a relevant increase in the safety of the operations and being protected against any possibility of act of vandalism. Moreover, the system is naturally protected and its operations are not effected by environmental conditions as water, dirt, chemicals etc. etc. This means to have a very robust system that eliminates other classical problems of the electrical contacts as electrical erosion and dust deposition strongly reducing the necessity of maintenance.

In the short term, this technology, indicated as *static* as the vehicle is parked or stopped during the charge, will probably substitute the conductive systems. However, the absence of mechanical constraints is leading the possibility to use the inductive transfer during the motion of the vehicle toward the *dynamic IPT*.

The installation of dynamic IPT systems into the road infrastructure will eliminate the necessity of stops for the recharge and, in the near term, this application could lead to a strong reduction of the on-board installed battery capacity. The success in the demonstration of the feasibility of this technology can indicate a practicable way to improve the electric mobility acceptance and solve the most critical aspects

in the use of electric vehicles. The present thesis illustrates the results of three years
of work dedicated to the study of the physical phenomena involved in the IPT that
have led to the construction of a prototype for the dynamic IPT oriented to private
transports. The analysis of the state of the art summarised in Chapter 2 provided the
background information on the domain of the IPT for automotive applications indi-
cating the current developments and the open issues of this technology. The researcher
activities started with the identification of a circuit model matching the description
of the magnetic field related phenomena and the interface with the power electron-
ics. The results, illustrated in Chapter 3 and Chapter 4, have provided indications
on the main principles of IPT and the topological arrangement of the components
giving the bases for the design of the power electronics and the magnetic structure.
The contributions on the design and testing of the power electronics are presented in
Chapter 5. In Chapter 6 is described the part of the work that has focused on the
design of the magnetic structure and its manufacturing aimed to the integration on an
existent electric vehicle and in the road infrastructure. The activities related to the
integration of the transmitter in the road infrastructure is presented Chapter 7. The
issue of human exposure to the involved electromagnetic fields is presented in Chap-
ter 8 together with the development of a dedicated methodology for the assessment
with respect to the international standards.

The presented research activities have been financed by two european project
eCo-FEV and FABRIC [4, 5] set in the seventh Framework Program for Research
and Technological Development (FP7) and conducted in the Department of Energy
of the Politecnico di Torino. One year of activity has been conducted in the CNRS
laboratory Génie électrique et électronique de Paris (GeePs) in France through a co-
tutelage agreement between the Politecnico di Torino and the Université Paris-Saclay.

Chapter 2

Energy transmission without contacts: technical evolution

Since the dawn of the electrical engineering and the diffusion of the electrical energy as the most common vector for the energy carriage, people started to think about a way to transmit this energy in absence of contacts. This desire is testified by the Farady's experiments about the electromagnetic induction and the transmission through different fluids [6] followed by the applications of the radio frequencies investigated by Hertz [7] arriving to the famous Tesla's experiments about the electric energy transmission at large distances [8].

In the last decades, the scientific community has indicated the different mechanisms apt for the transfer of energy at distance through the generic expression *wireless power transmission* frequently shorten through the acronym WPT. Today this definition covers several technologies in a widespread range of applications, powers and distances. Fig. 2.1 schematically shows the most common technologies devoted to WPT involving electromagnetic mechanisms [9]. The present work is dedicated to a particular technology on the domain of WPT called *resonant inductive power transmission* (IPT) in its application oriented to the charge of electric vehicles.

2.1 The birth of the concept

The two fundamental principles that govern the IPT are the Ampere's law of 1820 and the principle of magnetic induction discovered by Faraday in 1831. While Ampere proved that a current can produce a magnetic field, Faraday showed the duality between the magnetic and the electric field demonstrating that a time-varying magnetic field interacting with an electrical circuit can to induce into it an electromotive force. These two laws allowed a countless number of applications leading the development of the modern electric machines.

The first real improvement in the direction of IPT arrived with Tesla's studies.
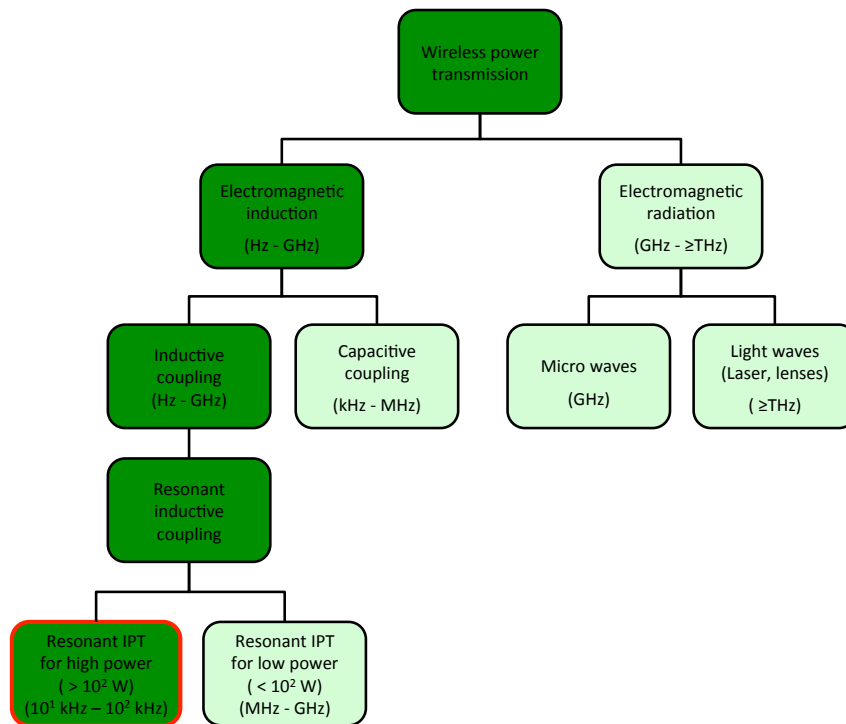
Figure 2.1: Different methods for the WPT using electromagnetic fields and waves.

Tesla coined the definition *wireless power transmission* [10] and demonstrated a first example of transmission without contact at the World Exposition of Chicago of 1893. Seven years later Tesla obtained the patent for a system for the wireless transmission over long distances (Fig. 2.2) using inductors in which he pointed out two important cornerstones of the inductive transmission [11]:

1. the necessity to operate at higher frequencies with respect to the tens of hertz typically adopted for the other electrical machines.

2. the use of capacitors (a Leyden jar in the Tesla's prototype) connected to the coils in order to work at the resonance frequency improving the efficiency of the transmission.

These concepts remained applied uniquely to the Tesla's prototypes according to his well know health problems but also due to some practical limitation of the system as the very high operating voltages of the coils and the related safety problems, the poor efficiency related to the losses at high frequency (skin effect) but, above all, the absence of an effective technology able to control and use this wirelessly transmitted energy.
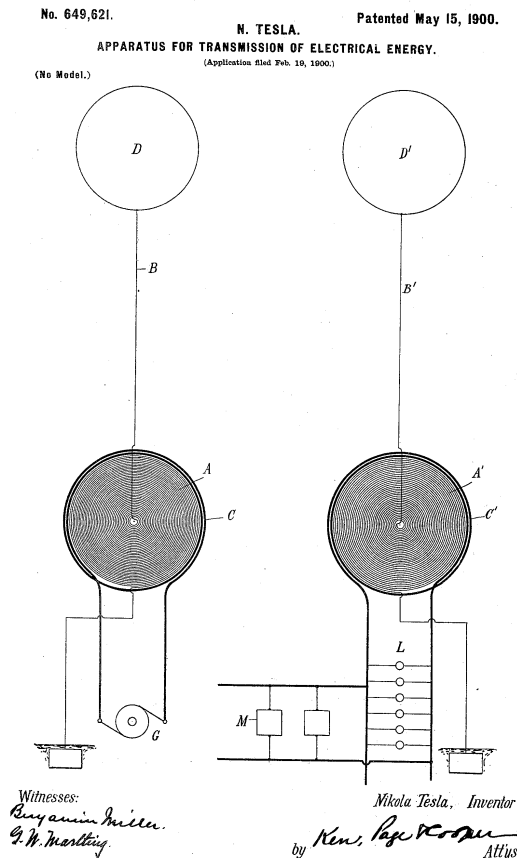
Figure 2.2: Illustration extracted from the Tesla patent of 1900.

2.2   The advent of the power electronics

A first real application of the inductive transmission arrived from the soviet electrical engineer Georgiy Babat. Back in 1943 Babat built an electric car, named *HF automobile* supplied through IPT! The system was composed by copper tubes forming a series of paths buried under the asphalt and a receiver placed under the vehicle at about 20 cm from the ground. The system was supplied through an electron-tube oscillator [12] providing a current of hundreds of ampere with a frequency of 50 kHz. Fig. 2.3 provides an idea about the huge dimensions of the equipment. The induced current was rectified and used to directly supply a 2 kW motor. This first prototype had only 4% of efficiency but it was the first working implementation of an IPT system for electric vehicles [9, 13].

    The first system adopting solid state devices appeared in a patent deposited by D.V. Otto in 1974 [14]. Otto proposed an IPT system for an electric vehicle supplied through a silicon controlled rectifier (SCR) inverter currying a current of 2000 A at 10 kHz. In this case the resonance of the receiver was assured through a series connected capacitor and connected to a DC motor by means of a rectification stage. The work was abandoned in the same year [15].
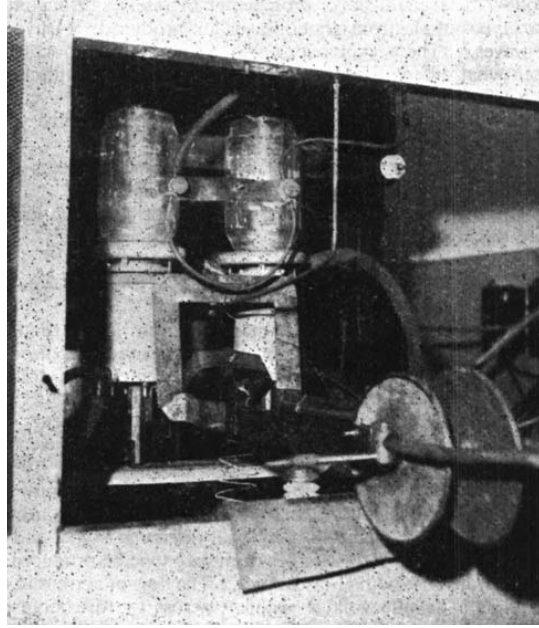
Figure 2.3: Photography of the electron tube adopted by Babat. In the lower right-hand corner are visible the two water cooled plates forming the tuning capacitor of the HF feeder.

In the 1980s, a first working IPT system with a moving vehicle was designed within the PATH project in California [16]. The goal of the project was the development of a segment of electric roadway to inductively power a small electric bus. The system operated with a variable air-gap between 5 and 10 cm and provided a power of 200 kW through a maximum current of 2000 A generated by an electrical machine working at the fundamental frequency of 400 Hz. The particularity of this prototype was the way to control the power transmission as variable capacitors were employed to detune the receiver resonant frequency. The achieved efficiency was of about 60%, but the prototype presented different critical aspects such as the huge dimensions and weight of the coils: the receiver was 4.5 m long and 1 m large with a weight of 850 kg [15]. A photography of the components is reported in Fig. 2.4.

Figure 2.4: Cross-section of the buried transmitter and the on board receiver of the PATH prototype.

In the 90s the massive interest of researchers and industries on the IPT technology started according to the improved performances of the power electronics devices at frequencies above the tens of kHz with currents between tens and hundreds of ampere.

At the end of the last century the diffusion of IPT systems for the charge of hybrid and electric buses began.

In 1997, the german Wampfler AG implemented a first commercialised IPT system for public transport based on the patents developed by the University of Auckland [17, 18]. This system was conceived to charge stationary buses and the technology named *static IPT*. The system planned the alignment of the receiver through a camera placed under the vehicle floor and the subsequent swiping down of the receiver obtaining a gap of about 4 cm with respect to the buried transmitter (Fig. 2.5). Electric buses wirelessly charged during parking, in an automated fashion, operate in Genoa and Turin since 2002 [19].

The Wampfler system operates at a frequency of about 15 kHz with a rated current of 80 A transmitting a rated power of 30 kW. The small air-gap between transmitter and receiver guarantees a good magnetic coupling and reduced stray fields level. Wampfler continued to work on these applications of the IPT as Conductix and in January 2014 it spun off as IPT Technology.

(a)

(b)
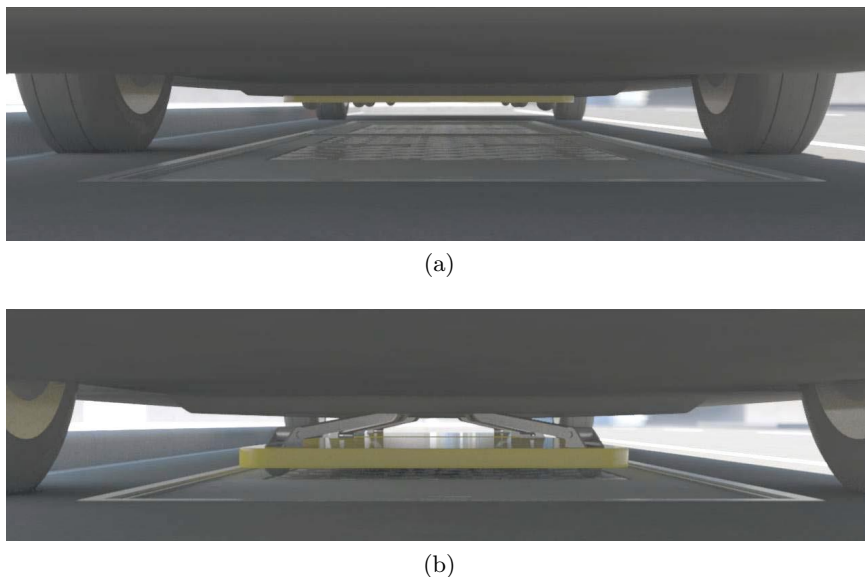
Figure 2.5: Position of the receiver in the Conductix system. Lifted receiver (a), receiver position during the charge (b).

2.3 The state of the art

Over recent years several companies and research centres have proposed their systems to improve the electrical mobility through the IPT.

WAVE, a startup born within the Utah State University, commercialises its IPT technology for the recharge of electrical buses. The first demonstration prototype has been implemented in a campus shuttle equipped with a receiver having the same dimensions of the transmitter embedded in the pavement of the bus stations. This

system allows the transfer of 25 kW at 20 kHz at each bus stop. The transfer takes place over an air-gap of 15-25 cm obtaining an efficiency of 90% [20].

Bombardier has announced in 2015 the development of a suite of solutions for IPT involving buses, light commercial vehicles and private cars called PRIMOVE. The implementation of the PRIMOVE IPT system for electric buses is ongoing in the cities of Mannheim and Berlin (Germany) and in the city of Bruges (Belgium). The presented solution works during the bus stops transferring a power of about 200 kW [21].

The only well demonstrated working system of dynamic IPT is the Shaped Magnetic Field In Resonance (SMFIR) system developed by the Korea Advanced Institute of Science and Technology (KAIST) since 2009. The SMFIR concept is based on the use of a massive quantity of ferrite to force the flux to come across a defined path as shown in Fig. 2.6.
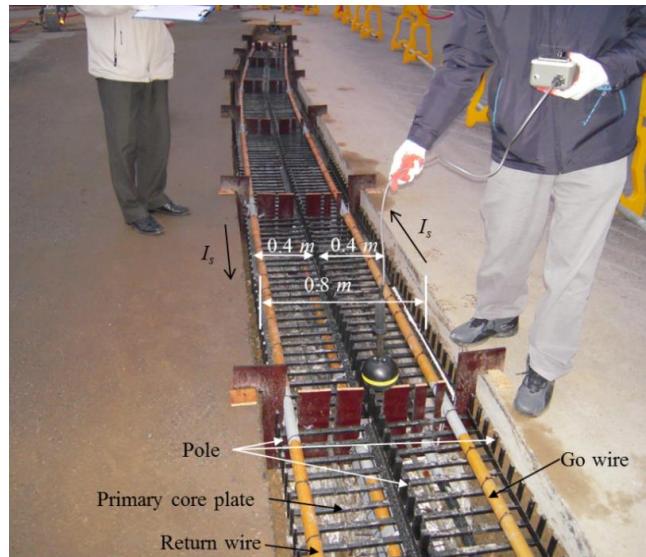
Figure 2.6: Road embedded ferrite track of the OLEV system.

This concept was applied to the OLEV (online electric vehicle) bus in 2011 and, currently, two OLEV buses are active in the KAIST campus in the cities of Daejeonn and Gumi, both in South Korea [22]. As shown in Fig. 2.7, the system consists of a roadside power conversion stage that rectifies the power received by the electrical network and supplies the buried power tracks (i.e. transmitters) at a frequency of 20 kHz. The road embedded power tracks are installed in sections of 122.5 m in length and each section is divided into segments the length which of can range from 2.5 m to 24 m [22]. A system of complex active and passive shielding solutions are installed on the bus with the purposes of confining the magnetic field along the desired path improving the electromagnetic compatibility (EMC) and reducing the electromagnetic field (EMF) emissions. An example of shielding system is depicted in Fig. 2.8 where a series of copper twisted brushes is used to create a closed conductive shielding path

[23].
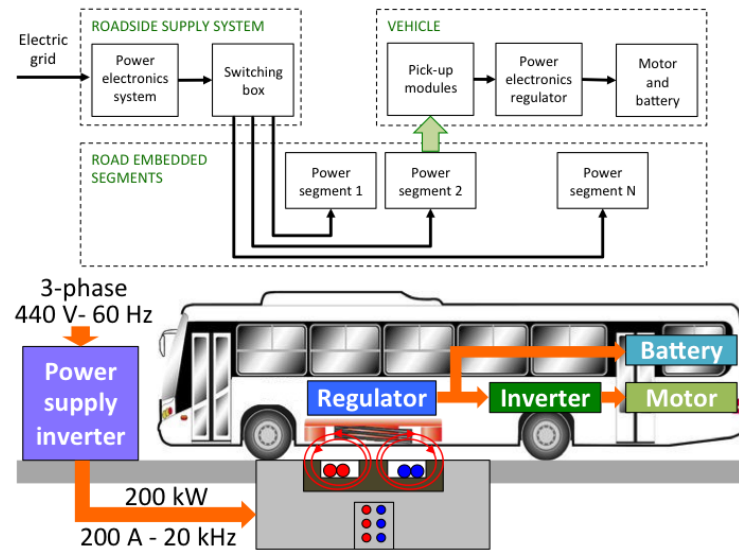
Figure 2.7: Scheme of the architecture of the OLEV bus IPT system.

KAIST developed different versions of OLEVs. The last one (3G) reached a maximum power transfer of about 200 kW with an efficiency of 74% [24].

In the automotive sector several products for the static IPT will be soon available on the market.

In 2011, Qualcomm acquired HaloIPT, a New Zealand company spun off by the University of Auckland. The HaloIPT developed IPT solutions in a power range between 3.3 and 20 kW and in 2011 it became partner with Rolls Royce which proposed the IPT technology to charge the luxury Phantom EV [25].

A spin off of the Massachusetts Institute of Technology (MIT), WiTricity, that develops wireless power transfer systems for various industries and applications, proposes also a solution for the static IPT. A 3.3 kW system has been proven to be functional but it is not yet commercially available. However, Toyota has licensed the WiTricity wireless system and started trials and verification tests for their Electric and Hybrid models [26].

Another ready product is the Plugless Power, a 3.3 kW IPT stationary charger developed by EVATRAN and commercialised in partnership with Bosch. It consists of a system adaptable to each EV model with a transmitter side composed by a control panel containing the power electronics directly linked to the electrical LV network and a transmitter pad that can be placed on a parking or garage floor. The Plugless Power were successfully tested with the Chevrolet VOLT and the Nissan Leaf EVs [27].
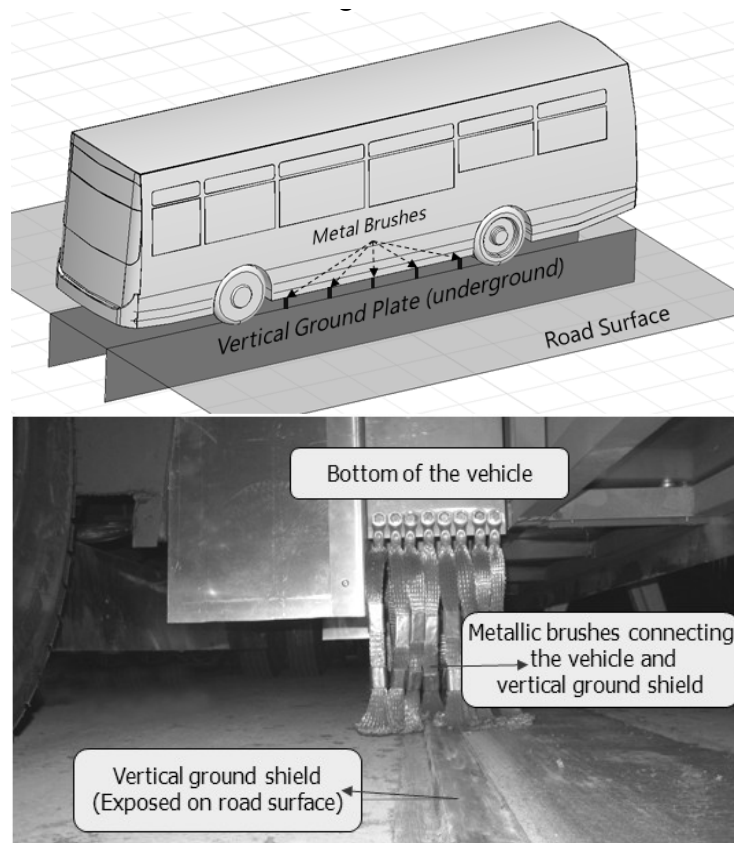
Figure 2.8: Illustration of a passive shielding solution applied to the OLEV bus.

2.4 Current standardisation processes

IPT systems, as the electric cars industry, involve several fields of engineering therefore the related standards and guidelines cover a large number of aspects.

As pointed out in the previous section, several commercial stationary IPT technologies exist but most of them are not compatible with each other due to the absence of standards by the time they were developed. Nevertheless, there are several active groups working now in the standardisation of stationary wireless charging systems.

The U.S. Society of Automotive Engineers (SAE International), a globally active professional association and standards organisation for engineering principally focused on transport industries, is providing the standards SAE J2954 and UL 2750 [28] and pairs them to other related standards as SAE J2847/6, SAE J2931/6 and SAE J2836/6 [29]. SAE published a Technical Information Report (TIR) J2954 for Wireless Power Transfer for Light-Duty Plug-In/ Electric Vehicles and Alignment Methodology for stationary charging applications on 2016 that is planned to be standardised within 2018 [30]. The International Electrotechnical Commission (IEC) has created in the 90s the subcommittee TC69 that is working on a dedicated standard for electric vehicles equipped with IPT systems which is intended to be published as IEC 61980. The

IEC 6190 reached the Committee Draft stage in 2000 and, since 2013, the standard has been in a "circulated as committee draft with vote" phase [31] and his "Part 1: General Requirement", is now in the Publication being printed (BPUB) state [32]. ISO started his activities on a new ISO standard, the ISO/AWI PAS 19363, in February 2014 [33]. The group responsible for the drafting is subcommittee TC22/SC2 "Road Vehicles-Electrically propelled Road Vehicles" [34]. The main activities of the different standardisation committees can be summarised as follows:

- Vehicle alignment methods.

- Interoperability of the different solutions.

- Frequency and power levels.

- Location of the receiver or receivers in the vehicle.

- Different aspects of safety such as the obstacle detection, electric shock protection, reference standard for the magnetic field levels, EMC.

- Communication protocols between power grid, vehicle and IPT infrastructure.

- Testing of the solutions.

Despite these processes evolve very fast, there are no published standards on EV IPT at the present. The same is for dynamic IPT. On this side, the IEEE Standards Association Industry Connection Activity has recently approved a working group for pre-standardisation aimed to be a complement to the activities of the SAE J2954. This is currently the only group working on dynamic IPT [35].

During the development of the works presented in this thesis, different aspects of the integration of an dynamic IPT solutions have been taken into account according to the creation of an on-road test site. A brief list of the adopted reference standards is reported in the following.

- ISO 15118. This Standard is titled "Road Vehicles-vehicle to grid communication interface" and specifies the communication between electric vehicles and power supply equipment.

- SAE J1100, titled "Surface vehicle recommended practice", represents the reference for the mechanical integration of the receiver on vehicle board with respect to the ground clearance.

- ICNIRP Guidelines for limiting exposure to time-varying electric and magnetic field (1 Hz -100 kHz) in the last version of 2010 has been the reference for the evaluation of the problem of the human exposure to the magnetic field involved in the developed application.

- IEC 61000 Electromagnetic Compatibility (EMC) has been the reference for the problems of interfacing of the IPT system with respect to the electric network.

- ISO 16750, ISO 26262 and ISO 6469 are all adopted standard related to safety specifications for electric and electronic devices for electrically propelled road vehicles.

- Since coils and related electrical components could be part of the road surface, their installation must follow the same regulations of the road. Regarding these aspects, the references are dependent on the country in which the system is installed and the material adopted for the paving. A list of standards can be found in [36].

This list is far to be exhaustive about the huge amount of standards that can be involved in a entire process of industrialisation of a dynamic IPT solution but it provides an idea about the complexity of the problem.

2.5   Current research projects

To respond to the necessity of additional investigations about the broad aspects of the dynamic IPT, several dedicated research projects are being conducted thanks to both public and industry funding. While the University of Auckland and the MIT are trying to extend their static applications toward the dynamic IPT with their spin offs HaloIPT and WiTricity, other research centres and universities are involved in joint projects all over the world.

In the United States, the biggest efforts on this domain are being conducted at the Oak Ridge National Laboratory (ORNL). The ORNL is the largest multi-program, science and energy laboratory in the U.S., funded mainly by United States Department of Energy (DOE). The ORNL has carried out research on static and dynamic inductive power transfer and is presently developing know-how on coupling coil design, power flow regulations, leakage field minimisation, misalignment tolerance and interoperability. The ORNL is stressing on the use of a single power electronics stage that supplies the different transmitters (as done by KAIST) determining the relative position of the vehicle by a radio communication system coupled with optical sensors as backup verification. Transmitters and receiver coil are constituted by the same circular pad [37]. A picture of the prototype under study is visible in Fig. 2.9.

At the same time, the KAIST is continuing toward the development of the sixth generation of OLEV trying to improve the efficiency investigating new solutions for the transmitter section layout and the design of the receiver structure. [31].

In the European Union, a series of research projects are being funded within the seventh Framework programme of Research (FP7) to investigate possible improvements of the electric mobility by developing solutions for the inductive charge.

Figure 2.9: Picture of the laboratory prototype developed at ORNL.

The projects Fastincharge and UNPLUGGED, both born in 2012, have been dedicated to the investigation of the impact of different charging solutions (i.e. plug-in, static and dynamic IPT) on the public acceptance of the electric mobility. In both projects different solutions for the static inductive charge have been proposed investigating the different aspects of economic feasibility, safety and standardisation. An analysis of the extension of these solutions toward the dynamic IPT was also performed [38, 39]. Both projects demonstrated a good efficiency of about 90% of two different static IPT solutions in condition of perfect alignment between transmitter and receiver together with the communication between the different components of the charging infrastructure. These results indicated as the use of IPT can really represent an effective way to overcome the actual problems related to range and size of the on-board storage.

At the end of the 2012 the eCo-FEV project began [4]. eCo-FEV intended to create an electric mobility platform for the integration of electric vehicles into a cooperative infrastructure systems. This platform would allow the information exchange between multiple infrastructure systems including road IT infrastructure, parking infrastructure, public transportation operators and vehicle charging infrastructure. This would assist user on trip planning decreasing range anxiety (i.e. the fear that the electric vehicle has insufficient range to reach its destination). The research leading the development of the present thesis is born within eCo-FEV during which the team of the Department of Energy of the Politecnico di Torino (POLITO) developed a first rough prototype for the dynamic IPT dedicated to a light commercial vehicle. In the project contest, a dedicated electrical infrastructure was developed together with a data infras-

tructure. The IPT prototype was installed without embedding the transmitters that were installed in cable wireways placed over the road pavement as shown in Fig. 2.10. The five transmitters have been supplied by a single power electronics supply composed by six inverter legs. The vehicle presence was identified solely through optical sensors. The system has been tested only for a limited power and limited speed but has provided important results in terms of management of the charging infrastructure in presence of a complex environment comprising electric vehicles, energy providers and data infrastructure [40].

Figure 2.10: Picture of the POLITO system developed inside the e

In Spain the researches on the IPT are continuing through the project Victoria [41]. The project started in 2013 with a consortium that comprises different industrial and academic partners. The aim is to double the range of electric buses without affecting operating times adopting IPT in static and dynamic developing a solution directly applied on an bus in the city of Malaga.

The research started under the eCo-FEV project is now continuing under the FABRIC project [5]. FABRIC started in 2014 as a systematic feasibility analysis of different on-road charging technologies for the range extension of electric vehicles. Different technology suppliers, research institutes and industrial partners are developing their solutions [42]. The POLITO team is improving the functionality of its system that is the one illustrated in the next chapters of the present thesis.

2.6   Open issues

Although several aspects related to the static IPT are still only roughly solved, it seems that the standardisation process will lead to an agreement in a short term period. Differently, in the dynamic IPT, the research activities are just started and a huge number of technical problems are still open issues. As has happened for the different solutions for the static, there is not a clear agreement on the shape of the

transmitter and receiver magnetic structure as well as the position of the receiver under the vehicle. As example, KAIST is continuing in the direction of a long track transmitter in the order of a hundred meters [43]; the Auckland team is proposing the adoption of small pads composed by more overlapped coils practically with the same dimension for both transmitter and receiver [44]; the ORNL is investigating the use of small circular pads [45] on both sides; Bombardier is proposing a track forming a three phase magnetic field distribution [46].

The same also happens for the choice of power levels and frequency. These two parameters impact the technology of the electronic switches, the relationships between coils dimension, transmittable power and air-gap [44]. In particular, the value of the frequency should pass the scrutiny of the electromagnetic compatibility (EMC) analysis in reference to on-board electric devices and electric power network. This analysis seems still not specifically investigated.

Another relevant problem for the dynamic IPT is the identification of the vehicle when it approaches a transmitter and the management of the passage between subsequent transmitters. Also in this case, different techniques are under investigation such as the use of auxiliary coils for the vehicle detection [47], optical sensors, radio communications [45] or cable data links between the power electronics converters.

Directly related to all previous issues there is the aspect of the protection against the exposure to the magnetic fields generated in the IPT applications. Few substantial studies have been conducted in this domain [48–50] and, in the dynamic IPT, standard measurement conditions, reference cases and proposed technical standards are still missing.

Finally there are the huge amount of challenges represented by all the aspects related to the creation of the road infrastructure, the inclusion of the transmitter section in the road surface, the choice of the material for the pavement, the handling of rainwater, the necessity of communication with the related management infrastructure.

The present works has tried to answer some of these problems in the way that will be explained in the following pages.

Chapter 3

Circuit modelling

This chapter illustrates the basic principles of the IPT technology. An equivalent circuit representation is derived starting from the different physical laws and components. This model provides a coupling between magnetic field and circuit also considering the interface with the power electronics elements.

3.1 Inductive power transmission basics

The physical mechanism at the base of the IPT is the magnetic induction.
With reference to Fig. 3.1, if a coil of N_1 turns is interested by the flow of a time-varying current $i_1(t)$, it generates a time-varying magnetic flux $\Phi_1(t)$. The relation between the generated flux, the current i_1 and the voltage at the coil terminals is expressed through equation (3.1) where the parameter L_1 is the *self-inductance* of the coil and is defined as in (3.2):

$$v_1(t) = N_1 \frac{\mathrm{d}\Phi_1}{\mathrm{d}i_1} \frac{\mathrm{d}i_1}{\mathrm{d}t} = L_1 \frac{\mathrm{d}i_1}{\mathrm{d}t} \tag{3.1}$$

$$L_1 = N_1 \frac{\mathrm{d}\Phi_1}{\mathrm{d}i_1} \tag{3.2}$$
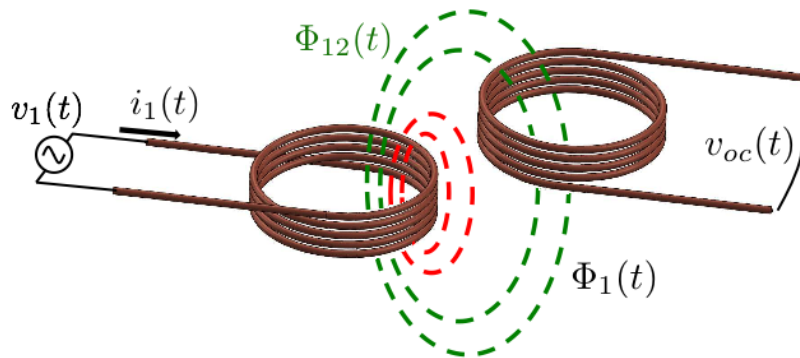
Figure 3.1: Representation of the magnetic induction between two coils.
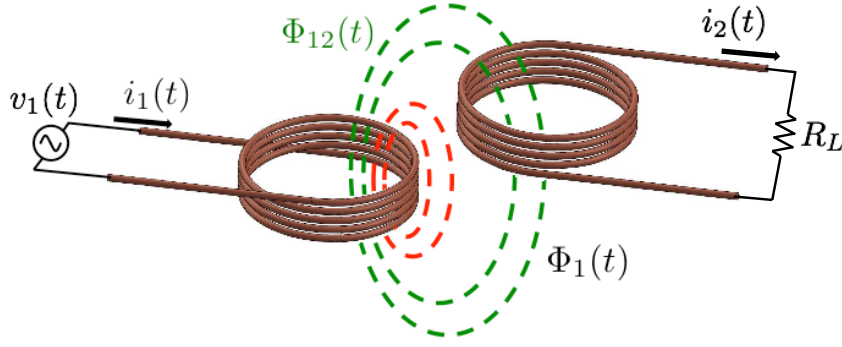
Figure 3.2: Illustration of the mechanism of inductive power transmission.

If another coil of N_2 turns is placed in the proximity, it links a part $\Phi_{12}(t)$ of the flux $\Phi_1(t)$ so, according to Faraday's law, a time-varying voltage can be measured at the terminals of the coil. This voltage is here called *open-circuit voltage* $v_{oc}(t)$ as it can be directly measured at the coil terminals under no-load conditions. The open-circuit voltage is expressed as

$$v_{oc}(t) = N_2 \frac{\mathrm{d}\Phi_{12}(t)}{\mathrm{d}i_1}\frac{\mathrm{d}i_1}{\mathrm{d}t} = M\frac{\mathrm{d}i_1}{\mathrm{d}t} \tag{3.3}$$

M is the *mutual inductance* between the two coil defined as

$$M = N_2 \frac{\mathrm{d}\Phi_{12}}{\mathrm{d}i_1} \tag{3.4}$$

If a load R_{L} is connected to the receiver, as shown in Fig. 3.2, a current i_2 can flow through the second coil meaning that a power transfer between the two coils can take place. A time-dependent model describing the system proposed in Fig. 3.3 can be formulated through the equations (3.5):

$$\begin{cases} v_1(t) = R_1 i_1(t) + L_1\frac{\mathrm{d}i_1}{\mathrm{d}t} - M\frac{\mathrm{d}i_2}{\mathrm{d}t} \\[2mm] M\frac{\mathrm{d}i_1}{\mathrm{d}t} = R_2 i_2(t) + L_2\frac{\mathrm{d}i_2}{\mathrm{d}t} + R_{\mathrm{L}} i_2(t) \end{cases} \tag{3.5}$$

The resistances of the two coils R_1 and R_2 are introduced. L_2 is the self-inductance of the second coil that can be derived similarly to (3.2) supplying this coil through a time-varying current i_2.

It can be proved that the value of the mutual inductance obtained supplying the second coil is the same as in (3.4) [51, 52].

The relation between the mutual inductance and the self-inductances of the two
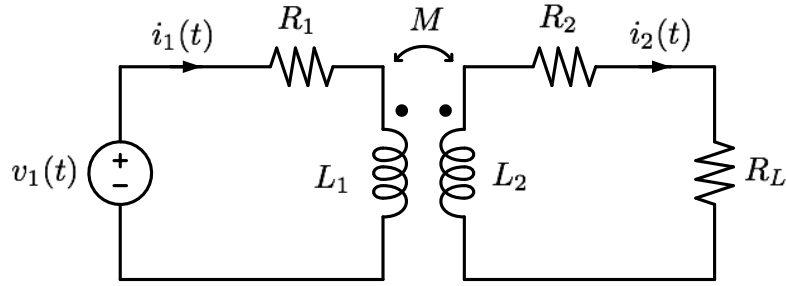
Figure 3.3: Circuit representation of the system illustrated in Fig. 3.2.

coils is expressed through the *coupling coefficient k*:

$$k = \frac{M}{\sqrt{L_1 L_2}} \tag{3.6}$$

This coefficient expresses the fraction of the flux emanating from one coil that links the other coil, then its value can range from zero to one:

$$0 \leq k \leq 1 \tag{3.7}$$

In the following, the first coil is named transmitter and every related parameter is indicated by the index 1 while the second coil is named receiver and the related parameters are indicated by the index 2.

3.2   First harmonic approximation

The energy transmitted by an IPT system can be stored in a battery or used to supply a device by means of power conversion. All these possibilities assume the presence of a rectifier connected to the receiver. The rectification is usually carried out by a diode bridge [53–57] or an active synchronous rectifier [58–60]. These components force the input voltage and the current to be in phase so, with reference to Fig. 3.4, the ratio between the first harmonic (1h) of the voltage $v_r(t)$ and the current $i_r(t)$ can be represented through the resistor R_L defined as

$$R_L = \frac{v_{r,1h}}{i_{r,1h}} \tag{3.8}$$

The same approximation can be done for the source v_1 meaning that the system is considered as working at one single frequency. These assumptions allow the use of the phasor representation. This means that the equation set (3.5) can be rewritten as
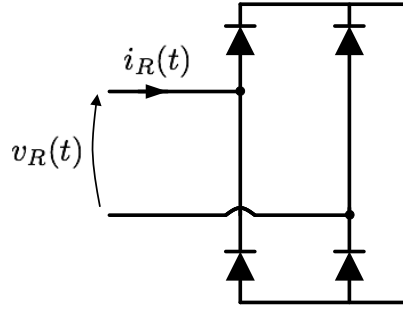
Figure 3.4: Voltage and current at the input of a diode bridge.

(3.9) where ω is the angular frequency of the source:

$$
\begin{cases}
\hat{V}_1 = R_1\hat{I}_1 + j\omega L_1\hat{I}_1 - j\omega M\hat{I}_2 & (3.9) \\[2mm]
j\omega M\hat{I}_1 = R_2\hat{I}_2 + j\omega L_2\hat{I}_2 + R_\mathrm{L}\hat{I}_2 & (3.10)
\end{cases}
$$

Expressing $\hat{I}_2$ in terms of $\hat{I}_1$ in (3.10) and substituting it into (3.9), it is possible to find the ratio between the source voltage $\hat{V}_1$ and current $\hat{I}_1$. This ratio describes the equivalent impedance that the system shows to the source. This impedance is called *total impedance* $\hat{Z}_\mathrm{T}$ and it is expressed as:

$$
\hat{Z}_\mathrm{T} = \frac{\hat{V}_1}{\hat{I}_1} = (R_1 + j\omega L_1) + \left(\frac{\omega^2 M^2}{R_2 + j\omega L_2 + R_\mathrm{L}} \right)
\tag{3.11}
$$

The first term of (3.11) is the impedance of only the transmitter in absence of coupling and it is indicated as:

$$
\hat{Z}_1 = R_1 + j\omega L_1
\tag{3.12}
$$

The second term represents the effect that the coupled receiver has on the transmitter. It is called *reflected impedance* and it is defined as:

$$
\hat{Z}_\mathrm{R} = \frac{\omega^2 M^2}{R_2 + j\omega L_2 + R_\mathrm{L}}
\tag{3.13}
$$

With reference to Fig. 3.5, it is worth noting that the denominator of the reflected impedance is equivalent to the impedance that the receiver shows to the dependent source $\hat{V}_\mathrm{oc}$ defined in (3.3):

$$
\hat{Z}_2 = R_2 + j\omega L_2 + R_\mathrm{L}
\tag{3.14}
$$

The above defined impedances are basic parameters for the study of the system. In fact, they describe the relationships between currents and voltages on both sides of the system. By means of these parameters it is possible to express the powers S_1 and S_2 that are the apparent power provided by the source and the power inductively
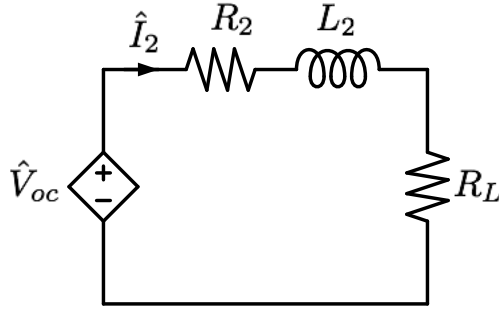
Figure 3.5: Equivalent representation of the receiver.

transferred to the receiver:

$$S_1 = V_1 I_1 = Z_{\mathrm{T}} I_1^2 \tag{3.15}$$

$$S_2 = V_{\mathrm{oc}} I_2 = V_{\mathrm{oc}} \frac{V_{\mathrm{oc}}}{\sqrt{(R_2 + R_{\mathrm{L}})^2 + (\omega L_2)^2}} =$$
$$= \frac{\omega^2 M^2}{\sqrt{(R_2 + R_{\mathrm{L}})^2 + (\omega L_2)^2}} I_1^2 = Z_{\mathrm{R}} I_1^2 \tag{3.16}$$

3.3   Introducing resonance

Thanks to the definitions of supplied and transmitted powers, it is possible to explain the motivations that lead to the introduction of the capacitive compensation.

On the receiver side, the impedance ωL_2 strongly reduces the current I_2 meaning a strong limitation in the power transfer capability as shown through (3.16). On the transmitter side, the presence of the impedance ωL_1 implies to have an apparent power higher than the provided active power P_1. In other words, the condition $S_1 \gg P_1$ means that the power rating of the source has to be much higher than the active transmitted power. The two directly related implications are a higher cost of the power electronic switches of the source and the necessity to work in strong hard-switching conditions decreasing the system efficiency [54,61,62]. These reasons justify the introduction of capacitors on both sides in order to achieve the cancellation of the inductive components of the impedances $\hat{Z}_1$ and $\hat{Z}_2$.

The capacitors have to be selected in order to obtain the effect of the cancellation at a common frequency for both sides. Clearly, there are several possibilities to obtain this result, but the basic ways consist of the simply connection of the capacitors in series or in parallel with the coils. Fig. 3.6 illustrates the four basic topologies. Each topology is indicated with two letters. The first letter refers to the transmitter and the second one to the receiver. The letter S is used for the series connection and the letter P for the parallel connection. For the sake of simplicity, the relations for the choice of the compensation capacitors are conducted considering as negligible the coil losses as commonly done in literature [53–55,63,64].

(a) SS

(b) SP

(c) PS

(d) PP
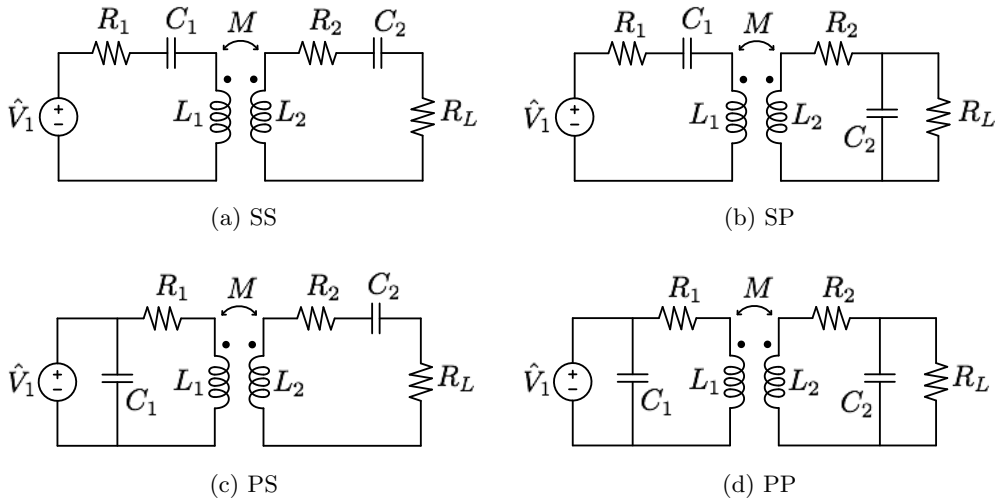
Figure 3.6: Circuit representation of the four basic compensation topologies.

Since the final goal of the compensation is the maximisation of the power transfer capability, the capacitive compensation on the receiver side can be interpreted as a sort of application of the *maximum power transfer theorem* to the only reactive elements. It is possible to demonstrate (see Annex B) that, for both series or parallel connections, the maximisation of the power transfer leads to the basic definition of a resonant system:

$$\omega^2 L_2 C_2 - 1 = 0 \tag{3.17}$$

Indicating as ω_0 the angular frequency that allows condition (3.17) to be fulfilled, the relation for the selection of the capacitor C_2 connected to the receiver coil is:

$$\boxed{C_2 = \frac{1}{\omega_0^2 L_2}} \tag{3.18}$$

ω_0 is called *resonance angular frequency*. It is related to the resonance frequency f_0 through the well known expression $\omega_0 = 2\pi f_0$.

The effect of the coupling of the receiver on the transmitter, can be represented through the reflected impedance obtaining the representations depicted in Fig. 3.7. In order to completely cancel the inductive component of the impedance presented by the circuit, the capacitor C_1 has to be chosen in order to compensate the self-inductance of the transmitter plus the imaginary component of $\hat{Z}_R$ at the same resonance frequency of the receiver. The general definition of the reflected impedance at the resonance is:

$$\hat{Z}_R = \frac{\omega_0^2 M^2}{\hat{Z}_2} \tag{3.19}$$

Its dependence on $\hat{Z}_2$ points out the dependence on the compensation topology of the receiver.

(a) Series compensated transmitter (b) Parallel compensated transmitter
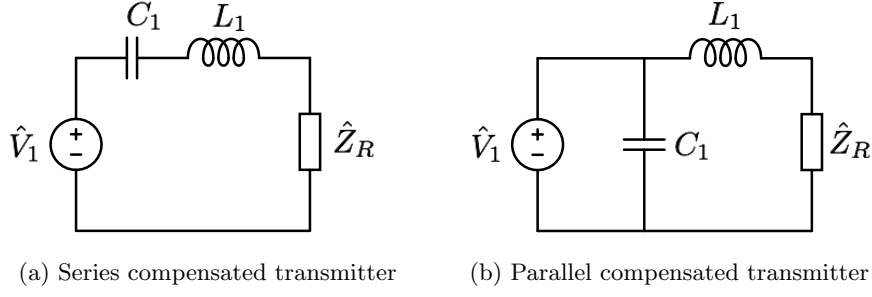
Figure 3.7: Transmitter in presence of coupled receiver.

For a parallel compensated receiver, $\hat{Z}_2$ is defined as

$$\hat{Z}_2 = j\omega_0 L_2 + \frac{R_{\mathrm{L}}}{1 + j\omega_0 R_{\mathrm{L}} C_2} \tag{3.20}$$

then $\hat{Z}_R$ can be written as

$$\hat{Z}_{\mathrm{R}} = \frac{\omega_0^2 M^2}{j\omega_0 L_2 + \dfrac{R_{\mathrm{L}}}{1 + j\omega_0 R_{\mathrm{L}} C_2}} \tag{3.21}$$

Finally, (3.21) can be expressed using only the inductive parameters by substituting C_2 through the relation (3.18):

$$\hat{Z}_{\mathrm{R}} = \frac{\omega^2 M^2 + j\omega R_{\mathrm{L}} \dfrac{M^2}{L_2}}{j\omega L_2} \tag{3.22}$$

It is possible to separate the real and imaginary parts of the impedance obtaining

$$\begin{cases} Re(\hat{Z}_{\mathrm{R}}) = R_{\mathrm{L}} \dfrac{M^2}{L_2} & (3.23) \\[2em] Im(\hat{Z}_{\mathrm{R}}) = -\omega \dfrac{M^2}{L_2} & (3.24) \end{cases}$$

According to (3.24), if the capacitor C_1 is placed in parallel with the receiver, its values has to satisfy the relation

$$Im\left[\left(\frac{1}{j\omega_0 C_1} \right) // \left(j\omega L_1 + \hat{Z}_{\mathrm{R}} \right) \right] = 0 \tag{3.25}$$

that means to choose:

$$C_1 = \frac{L_1 - \dfrac{M^2}{L_2}}{\left(\dfrac{M^2 R_L}{L_2} \right)^2 + \omega_0^2 \left(L_1 - \dfrac{M^2}{L_2} \right)^2} \tag{3.26}$$

If C_1 is placed in series with the receiver:

$$C_1 = \frac{1}{\omega_0^2 \left(L_1 - \dfrac{M^2}{L_2}\right)} \tag{3.27}$$

For a series compensated receiver $\hat{Z}_2$ is expressed as:

$$\hat{Z}_2 = j\omega L_2 + \frac{1}{j\omega C_2} R_L \tag{3.28}$$

then, again according to (3.18):

$$\begin{cases} Re(\hat{Z}_R) = \dfrac{\omega_0^2 M^2}{R_L} & \tag{3.29} \\[4mm] Im(\hat{Z}_R) = 0 & \tag{3.30} \end{cases}$$

(3.30) shows an important property of the series compensation of the receiver that is the ability to cancel the reflected imaginary part of $\hat{Z}_R$. If the capacitor C_1 is placed in parallel with the receiver, it has to satisfy the same condition of (3.25) that means to choose the capacitor according to:

$$C_1 = \frac{L_1}{\left(\dfrac{\omega_0^2 M^2}{R_L}\right)^2 + \omega_0^2 L_2^1} \tag{3.31}$$

If C_1 is connected in series, it has to simply compensate the self-inductance of the transmitter independently of the effect of the coupling:

$$C_1 = \frac{1}{\omega_0^2 L_1} \tag{3.32}$$

The found relations are here reported as summary:

$$\begin{cases} C_1^{SS} = \dfrac{1}{\omega_0^2 L_1} & \tag{3.33} \\[6mm] C_1^{SP} = \dfrac{1}{\omega_0^2 \left(L_1 - \dfrac{M^2}{L_2}\right)} & \tag{3.34} \\[6mm] C_1^{PS} = \dfrac{L_1}{\left(\dfrac{\omega_0^2 M^2}{R_L}\right)^2 + \omega_0^2 L_2^1} & \tag{3.35} \\[8mm] C_1^{PP} = \dfrac{L_1 - \dfrac{M^2}{L_2}}{\left(\dfrac{M^2 R_L}{L_2}\right)^2 + \omega_0^2 \left(L_1 - \dfrac{M^2}{L_2}\right)^2} & \tag{3.36} \end{cases}$$

It is worth noting that (3.33) is the only relation where load and mutual inductance do not appear. This indicates that, for a chosen value of capacitance, in the case of an SS compensation, the condition of resonance remains stable at the same frequency independently of the variations of M and R_L. On the other hand, the parallel compensation on the primary side is effected by both dependencies making these topologies not advisable for applications with a moving receiver that can cause frequent variations of the coupling.

3.4 Total impedance

The expressions of the total impedances derived in the previous section are here grouped:

$$
\begin{cases}
\hat{Z}_\mathrm{T}^{SS} = j\left(\omega L_1 - \dfrac{1}{\omega C_1}\right) + \dfrac{\omega^2 M^2}{\left(R_\mathrm{L} + j\left(\omega L_2 - \dfrac{1}{\omega C_2}\right)\right)} & (3.37) \\[3em]
\hat{Z}_\mathrm{T}^{SP} = j\left(\omega L_1 - \dfrac{1}{\omega C_1}\right) + \dfrac{\omega^2 M^2}{\left(j\omega L_2 + \dfrac{R_\mathrm{L}}{1 + j\omega R_\mathrm{L} C_2}\right)} & (3.38) \\[3em]
\hat{Z}_\mathrm{T}^{PS} = \left(\dfrac{1}{(j\omega L_1) + \dfrac{\omega^2 M^2}{\left(R_\mathrm{L} + j\left(\omega L_2 - \dfrac{1}{\omega C_2}\right)\right)}} + j\omega C_1\right)^{-1} & (3.39) \\[3em]
\hat{Z}_\mathrm{T}^{PP} = \left(\dfrac{1}{(j\omega L_1) + \dfrac{\omega^2 M^2}{\left(j\omega L_2 + \dfrac{R_\mathrm{L}}{1 + j\omega R_\mathrm{L} C_2}\right)}} + j\omega C_1\right)^{-1} & (3.40)
\end{cases}
$$

The different expressions point out a resulting different behaviour with respect to the variation of the system parameters. Considering a condition of very weak coupling ($M \to 0$), the resulting values of $\hat{Z}_\mathrm{T}$ are:

$$
\hat{Z}_\mathrm{T}^{SS} \approx \hat{Z}_\mathrm{T}^{SP} \approx j\omega L_1 + \frac{1}{j\omega C_1}
$$

$$
\hat{Z}_\mathrm{T}^{PS} \approx \hat{Z}_\mathrm{T}^{PP} \approx \left(\frac{1}{j\omega L_1} + j\omega C_1\right)^{-1}
$$

(3.41)

These equations describe the impedances of a series and a parallel LC circuit respec-

tively. This means that, at the resonance frequency, the series compensated transmitter tends to behave as a short circuit while the parallel one tends to an open circuit. For a general case with $M \ll 1$ but not zero, the topologies with parallel compensated transmitter need a higher voltage of the source to transmit the same power with respect to the case with a series compensated transmitter. Two examples are provided in [65] and [66]. The first work presents a system for static IPT with parallel compensation. The system transfers a rated power of 2 kW with an air-gap of 0.2 m. The power supply of the application operates at a voltage level of 1.6 kV. Conversely, in the second work, a series-series compensated system is presented. It transfers the same power with an air-gap of 0.15 m but with a rated voltage of the source of 500 V. The principal benefit of the parallel compensation is represented by its intrinsic protection against the sudden absence of the receiver. In this case the system behaves as an open-circuit simply forcing the current of the source to zero.

The difference between SS and SP is understandable by observing the value of the total impedance at the resonance ($\omega = \omega_0$):

$$
\begin{cases}
Z_{\mathrm{T}}^{SS} = \dfrac{\omega_0^2 M^2}{R_{\mathrm{L}}} & (3.42) \\[2ex]
Z_{\mathrm{T}}^{SP} = R_{\mathrm{L}} \dfrac{M^2}{L_2} & (3.43)
\end{cases}
$$

For a load consisting in a low R_{L}, the SS compensation presents a higher impedance than the SP compensation. This suggests that the SP compensation is well suited for application at high voltage and low currents at the receiver, as in the applications illustrated in [67–72] that are generally not dedicated to the automotive IPT.

3.5   Hybrid compensation topologies

As conclusive part of this chapter, more complex compensation topologies are briefly introduced. All these topologies start from the idea to combine the properties of series and parallel compensation constituting *hybrid topologies* [73]. Two hybrid topologies have been proposed in [55] and [56] with the circuit configurations shown in Fig. 3.8.

The combination of the characteristics allow to improve the tolerances with respect to the misalignment and the regulation of the value of the total impedance through a proper selection of the capacitors [56, 73]. Nevertheless, the dependency of the resonance condition on coupling and load variations remains due to the presence of the parallel capacitors. This practically implies the adoption of control techniques at variable frequency to maintain a high efficiency of the transmission. The variation of the frequency leads to an increase of the rated power of the power electronics in order to provide the necessary reactive power when the system works out of resonance [56].

The more critical aspect is represented by the necessity to introduce additional

(a)

(b)
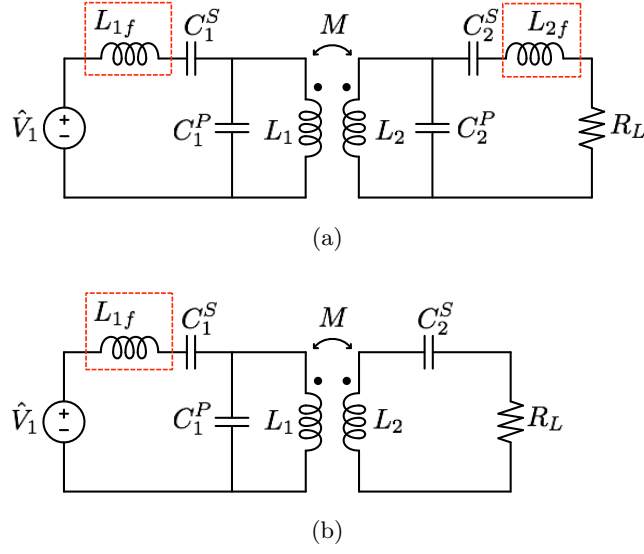
Figure 3.8: Hybrid compensation configurations. Symmetric (a) and only on transmitter side (b). In the red box the additional filter inductor for the commutation.

inductive elements, L_{1f} and L_{2f}, in order to prevent current peaks during the voltage transitions since a square voltage source is applied to the group of reactive elements [56]. The additional inductors and the use of more capacitors, imply an increase of costs, volumes and complexity of the connections.

3.6   Efficiency

A complete evaluation of an IPT system should consider several components and phenomena that determine losses (e.g. the capacitor ESRs, the hysteresis losses in the ferromagnetic elements, the losses in the conductive materials in the vicinity of the coils, the conductive and switching losses in the power electronic converters etc.). This clearly indicates that a compete analytical expression of the efficiency is practically unfeasible. Nevertheless, a simplified expression of the efficiency referred to the coils is proposed here. It can be derived by using the circuit models shown in Fig. 3.6 where the coil resistances are considered. A general expression of the efficiency can be derived indicating as I_{L1} and I_{L2} the currents flowing in the inductors and as I_{L} the current that flows in the load:

$$\eta = \frac{R_{\mathrm{L}} I_{\mathrm{L}}^2}{R_1 I_{L1}^2 + R_2 I_{L2}^2 + R_{\mathrm{L}} I_{\mathrm{L}}^2} \tag{3.44}$$

According to the compensation topologies on the transmitter side, it is possible to express the current I_{L1} as

$$\hat{I}_{L1} = \hat{I}_1 \tag{3.45}$$

for the series compensation and as

$$\hat{I}_{L1} = \hat{I}_1 - j\omega C_1 \hat{V}_1 \tag{3.46}$$

for the parallel compensation.

The same can be done for the currents on the receiver side I_{L2} and I_{L}:

$$\hat{I}_2 = \frac{j\omega M \hat{I}_1}{\left(R_2 + R_{\mathrm{L}} + j\left(\omega L_2 - \dfrac{1}{\omega C_2} \right) \right)} \tag{3.47}$$

$$\hat{I}_{\mathrm{L}} = \hat{I}_2 \tag{3.48}$$

for the series compensated receiver and

$$\hat{I}_2 = \frac{j\omega\left(1 + j\omega R_{\mathrm{L}} C_2\right)}{R_{\mathrm{L}} + \left(R_2 + j\omega L_2\right)\left(1 + j\omega R_{\mathrm{L}} C_2\right)} \hat{I}_1 \tag{3.49}$$

$$\hat{I}_{\mathrm{L}} = \frac{1}{\left(1 + j\omega R_{\mathrm{L}} C_2\right)} \hat{I}_2 \tag{3.50}$$

for the parallel compensated one.

Substituting the expressions of the currents in (3.44), it is possible to obtain two expressions of the efficiency that are dependent only on the compensation topology of the receiver:

$$\eta_{\mathrm{SS,PS}} = \frac{R_{\mathrm{L}}}{\left(R_{\mathrm{L}} + R_2\right)\left(1 + R_1 \dfrac{R_2 + R_{\mathrm{L}}}{\omega_0^2 M^2}\right)} \tag{3.51}$$

$$\eta_{\mathrm{SP,PP}} = \frac{R_{\mathrm{L}}}{R_{\mathrm{L}} + R_2 + \dfrac{R_2 R_{\mathrm{L}}^2}{\omega_0^2 L_2^2} + \dfrac{R_1 R_2^2}{\omega_0^2 M^2} + \dfrac{R_1 L_2^2}{M^2}} \tag{3.52}$$

Both expressions indicate that the efficiency of the system can be increased by minimising the coil resistances and by increasing the mutual inductance and the resonance frequency. Naturally, the increase of the frequency has to be managed through the selection of proper components, materials and constructive techniques in order to minimise the losses increase due to phenomena of skin and proximity effect or induced losses in the nearby components. This considerations provide the basis for the design of the coils.

3.7 Conclusions

This chapter described the mechanism of inductive power transmission. It explained the motivations for the introduction of the compensation capacitors that make the IPT systems resonant systems. Electromagnetic phenomena and components have

been coupled in an equivalent circuit model that can be used for the study of the characteristic of the power transfer and for the system design. This model provided the key results here summarised:

- The behaviour of the system and its matching with the source can be described by means of the total impedance $\hat{Z}_T$

- The introduction of the compensation capacitors introduces several benefits that are:

    - Increase of the power transfer capabilities

    - Decrease of the VA rating of the power electronics of the system supply

    - Possibility to adopt techniques of soft-switching commutations that can strongly reduce the commutation losses. This aspect is more detailed in Chapter 5

Finally, the study of the different topologies for the compensation indicates that each compensation presents different properties in terms of $\hat{Z}_{\mathrm{T}}$, tolerances to the variation of the coupling and the load. Each topology is better suited for certain applications and certain architectures of the power electronics demanding also different approaches in terms of control and protection.

Chapter 4

Frequency behaviour

In this chapter the study in the frequency domain of the model proposed in the previous chapter is presented. This study provides the last information useful to the definition of the power electronics requirements. The analysis is carried out for an SS compensated system, but the results can be extended to every basic topology by means of an equivalent series representation [74, 75]. Due to the complexity of the system that contains five reactive elements, the model without losses is considered.

4.1 Quality factor

The description of the coupled resonant systems in the frequency domain can be usefully represented by means of three main parameters. The first two are the coupling coefficient k and the resonance angular frequency ω_0 already defined in Section 3.3. The third parameter is the *quality factor Q*. This parameter has multiple definitions [76]. The one adopted in this work is the ratio between the stored energy E_{reactive} and the dissipated energy E_{active} during each period in a resonant circuit at the angular frequency ω_0:

$$Q = 2\pi \frac{E_{\text{reactive}}}{E_{\text{active}}} \tag{4.1}$$

The stored energy at the resonance is constant and equivalent to the magnetic energy stored in the inductor or the electrostatic one stored in the capacitor. In the IPT system the quality factor for each side, in its own right, is defined as:

$$Q_1 = \frac{\omega_0 L_1}{R_1} = \frac{1}{\omega_0 C_1 R_1} \tag{4.2}$$

$$Q_2 = \frac{\omega_0 L_2}{R_2 + R_{\text{L}}} = \frac{1}{\omega_0 C_2 \left(R_2 + R_{\text{L}}\right)} \tag{4.3}$$

Considering the approximation $R_{\text{L}} \gg R_{1,2}$, the relation (4.3) can be expressed as:

$$Q_2 \approx \frac{\omega_0 L_2}{R_{\text{L}}} = \frac{1}{\omega_0 C_2 R_{\text{L}}} \tag{4.4}$$

and the relation

$$Q_1 \gg Q_2 \tag{4.5}$$

holds true for a general case.

4.2 Amplitude behaviour: the multiple peaks

The coupled resonant circuits were studied for the first time in the radio frequencies domain where these circuits were investigated as band-pass filters. The results acquired in that domain pointed out as the transfer function between the output voltage, measured at the output resistor terminals (equivalent to R_L), and the input voltage, can present two maxima with respect to different values of angular frequency and under specific conditions of Q and k [75, 77].

This phenomenon can be explained qualitatively by observing the first expression of the total impedance (3.11) given in Section 3.2. The presence of the coupled inductance L_2 leads to a reduction of the inductive reactance of $\hat{Z}_T$ while the presence of the compensation capacitor C_2 tends to increase this component as one can see from (3.37). This means that, at frequencies below resonance, $\hat{Z}_R$ is inductive while the self-impedance of the transmitter $\hat{Z}_1$ is capacitive. The effect of the coupling lowers the value of Z_T that, for a certain value of $\omega = \omega_1$, reaches a minimum remaining inductive. The dual behaviour occurs for frequencies above resonance where $\hat{Z}_R$ is capacitive and compensates the inductive reactance of $\hat{Z}_1$ reaching another minimum at $\omega = \omega_2$. At that point, the behaviour of $\hat{Z}_T$ is capacitive. Two maxima of the currents correspond then to ω_1 and ω_2. A detailed analysis was provided by Terman in [77] that formulates the two angular frequencies as:

$$\omega_{1,2} = \omega_0 \frac{1}{\sqrt{1 \pm k\sqrt{1 - \frac{1}{2k^2}\left(\frac{1}{Q_1^2} + \frac{1}{Q_2^2}\right)}}} \tag{4.6}$$

According to (4.5), the same relation can be approximated neglecting the terms in which Q_1 appears:

$$\omega_{1,2} = \omega_0 \frac{1}{\sqrt{1 \pm k\sqrt{1 - \frac{1}{2k^2}\frac{1}{Q_2^2}}}} \tag{4.7}$$

This expression admits real solutions only if

$$k \geq \frac{1}{\sqrt{2}Q_2} \tag{4.8}$$

In Fig. 4.1 it is depicted the behaviour of the two angular frequencies versus variations

of the quality factor of the receiver and for different values of coupling. This graph points out that the values of the two angular frequencies is not symmetric with respect to the resonance angular frequency and that, for values roughly bigger than 20 it is possible to introduce the approximation $Q_2 \to \infty$ that means the position of the two peaks depends only on the coupling according to the relation

$$\omega_{1,2} = \omega_0 \frac{1}{\sqrt{1 \pm k}} \tag{4.9}$$
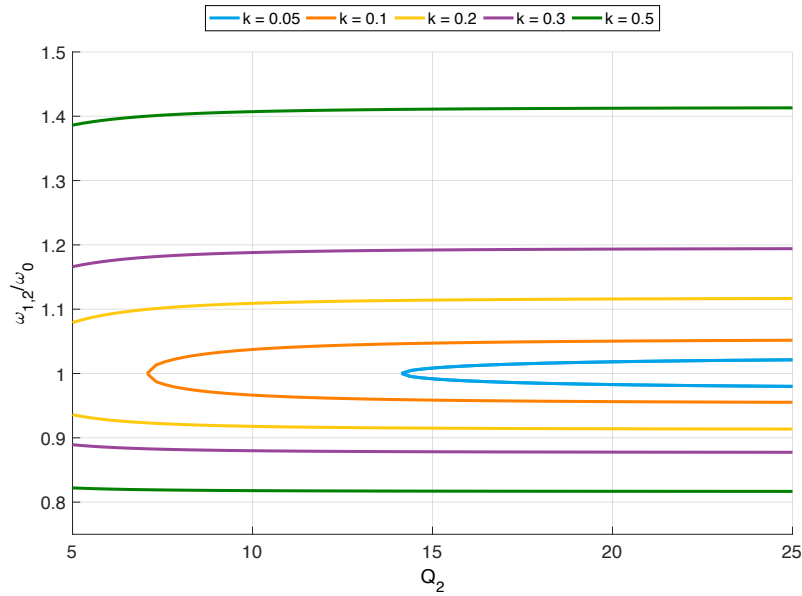
Figure 4.1: Map of angular frequencies $\omega_{1,2}$ for variation of the receiver quality factor at different couplings.

Finally, in Fig. 4.2a and Fig. 4.2b the effect of the coupling variation on the transmitter and receiver currents is depicted. It is worth noting that, for an increase in the coupling, the peaks of I_1 become lower and the width of the curve remains practically constant. Conversely, the peaks of the current I_2 tend to remain at the same amplitude and the curve tends to become wider.

In correspondence with ω_1 and ω_2, the phase of $\hat{Z}_T$ is far from zero, consequently, it is impossible to transfer power in optimal condition of efficiency and minimum rated power from the point of view of the power electronics.

4.3   Phase response: the multiple zero crossing

The behaviour of the phase of $\hat{Z}_T$ is one of the peculiar aspects of IPT systems. In fact, the phase can rapidly vary for frequencies slightly different from the resonance one, crossing the zero degrees axes at more than one point. This means that $\hat{Z}_T$ can show a resistive behaviour in three different points and between them its equivalent behaviour

(a)

(b)
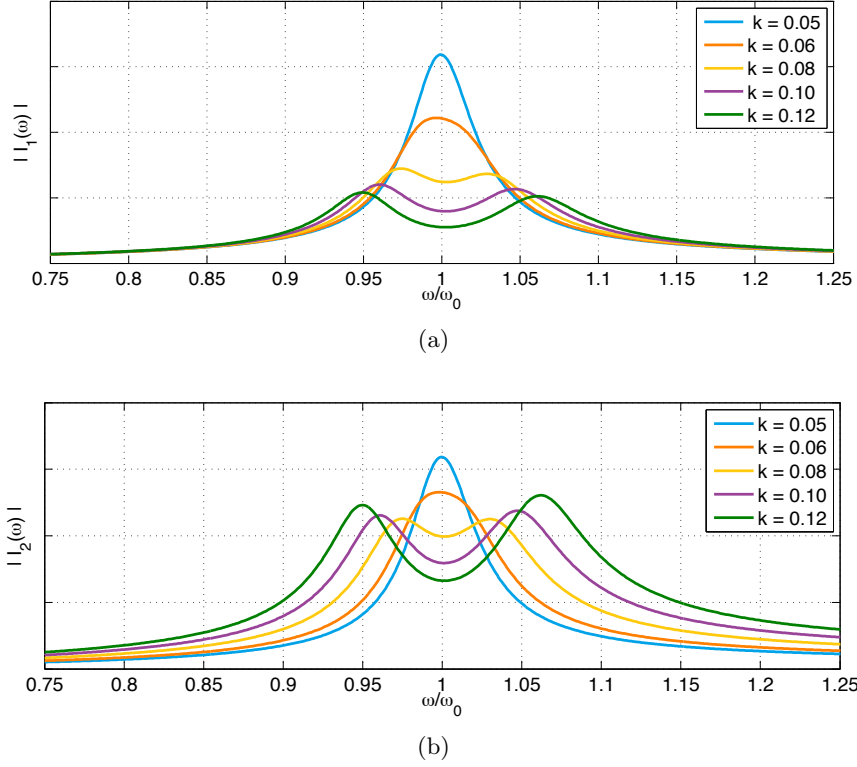
Figure 4.2: Effect of the variations of coupling on the transmitter (a) and receiver current (b) for a receiver quality factor $Q_2 = 10$.

can abruptly change. This phenomenon is here named *multiple-zero-crossing* and it appears under certain conditions of coupling and quality factor.

The analysis of this phenomenon starts from the definition of the reflected impedance by separating real and imaginary part:

$$\hat{Z}_{\mathrm{R}} = \frac{\omega^2 M^2}{j\omega L_2 + \dfrac{1}{j\omega C_2} + R_{\mathrm{L}}} = \begin{cases} Re\left(\hat{Z}_{\mathrm{R}}\right) = \dfrac{\omega^4 M^2 C_2^2 R_{\mathrm{L}}}{\left(\omega^2 L_2 C_2 - 1\right)^2 + \omega^2 R_{\mathrm{L}}^2 C_2^2} & (4.10) \\[4mm] Im(\hat{Z}_{\mathrm{R}}) = -\dfrac{\omega^3 M^2 C_2 \left(\omega^2 L_2 C_2 - 1\right)}{\left(\omega^2 L_2 C_2 - 1\right)^2 + \omega^2 R_{\mathrm{L}}^2 C_2^2} & (4.11) \end{cases}$$

Thanks to the previous relations it is easy to express the real and the imaginary part of the total impedance as

$$\hat{Z}_{\mathrm{T}} = \hat{Z}_1 + \hat{Z}_{\mathrm{R}} = \begin{cases} Re\left(\hat{Z}_{\mathrm{T}}\right) = Re\left(\hat{Z}_{\mathrm{R}}\right) & (4.12) \\[4mm] Im\left(\hat{Z}_{\mathrm{T}}\right) = j\left(\omega L_1 - \dfrac{1}{\omega C_1}\right) + Im\left(Z_{\mathrm{R}}\right) & (4.13) \end{cases}$$

It is possible to express $\hat{Z}_{\mathrm{T}}$ using the introduced main parameters by providing the

following substitutions:

$$L_1 C_1 = L_2 C_2 = \frac{1}{\omega_0^2} \tag{4.14}$$

$$M^2 C_1 C_2 = M^2 \frac{1}{\omega_0^4 L_1 L_2} = \frac{1}{\omega_0^4} k^2 \tag{4.15}$$

$$R_{\mathrm{L}}^2 C_2^2 = \frac{1}{\omega_0^2 Q_2^2} \tag{4.16}$$

finally obtaining

$$
\begin{cases}
Re\left(\hat{Z}_{\mathrm{T}}\right) = \dfrac{\dfrac{\omega^4}{\omega_0^3} k^2 L_1 \dfrac{1}{Q_2}}{\left(1 - \dfrac{\omega^2}{\omega_0^2}\right)^2 + \dfrac{\omega^2}{\omega_0^2}\dfrac{1}{Q_2^2}} & (4.17) \\[3em]
Im\left(\hat{Z}_{\mathrm{T}}\right) = \dfrac{\dfrac{\omega^4}{\omega_0^4}\left(1 - k^2\right) + \dfrac{\omega^2}{\omega_0^2}\left(\dfrac{1}{Q_2^2} - 2\right) + 1}{\omega C_1 \left(\dfrac{\omega^4}{\omega_0^4} - 2\dfrac{\omega^2}{\omega_0^2} + \dfrac{\omega^2}{\omega_0^2}\dfrac{1}{Q_2^2} + 1\right)} & (4.18)
\end{cases}
$$

Equation (4.17) shows that the real component of the total impedance is always positive for all values of ω, k and Q_2. Hence, the analysis can be focused on the imaginary part only. The denominator of (4.18) is independent of the coupling and its value is positive for every value of Q_2 and ω. This means that the search of the frequencies for which multiple-zero-crossing occurs is limited to the study of the numerator under the condition

$$\left(\frac{\omega}{\omega_0}\right)^4 \left(1 - k^2\right) + \left(\frac{\omega}{\omega_0}\right)^2 \left(\frac{1}{Q_2^2} - 2\right) + 1 = 0 \tag{4.19}$$

that is satisfied by

$$\boxed{\omega = \omega_0 \sqrt{\frac{\left(2Q_2^2 - 1\right) \pm \sqrt{1 + 4Q_2^2\left(Q_2^2 k^2 - 1\right)}}{2\left(1 - k^2\right)Q_2^2}}} \tag{4.20}$$

The existence of multiple points at which the phase of $\hat{Z}_{\mathrm{T}}$ becomes zero is dependent on the existence of real solutions of the equation (4.20). This happens only if the following conditions are verified:

$$
\begin{cases}
1 + 4Q_2^2\left(Q_2^2 k^2 - 1\right) > 0 & (4.21) \\[1em]
\left(2Q_2^2 - 1\right) \pm \sqrt{1 + 4Q_2^2\left(Q_2^2 k^2 - 1\right)} > 0 & (4.22)
\end{cases}
$$
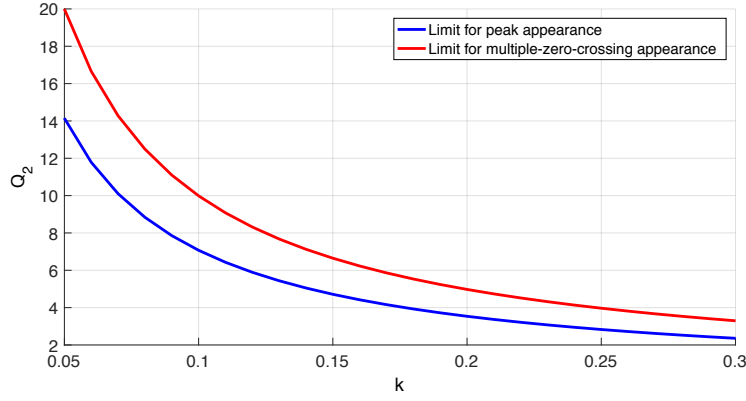
Figure 4.3: Limits curve for the existence of current peaks (4.8) and multiple-zero-crossings (4.25).

According to these relations, the intervals where the solutions exist are respectively

$$\begin{cases} Q_2 \leq \dfrac{\sqrt{1 - \sqrt{1 - k^2}}}{\sqrt{2}k} \ \wedge \ Q_2 \geq \dfrac{\sqrt{1 + \sqrt{1 - k^2}}}{\sqrt{2}k} & (4.23) \\[4ex] Q_2 \leq \sqrt{1 - \sqrt{1 - \dfrac{1}{2}\left(1 + k^2\right)}} \ \wedge \ Q_2 \geq \sqrt{1 - \sqrt{1 - \dfrac{1}{2}\left(1 + k^2\right)}} & (4.24) \end{cases}$$

However, it may be observed that the fulfilment of (4.23) also implies the fulfilment of (4.24). Moreover, the fulfilment of the left conditions implies values of Q_2 lower than unit that are not practically achieved. This means that the only useful relation is

$$Q_2 \geq \frac{\sqrt{1 + \sqrt{1 - k^2}}}{\sqrt{2}k} \tag{4.25}$$

Considering a value of $k \ll 1$, this approximation holds true:

$$Q_2 \geq \frac{1}{k} \tag{4.26}$$

The presence of the multiple-zero-crossing is dependent on the values of k and Q_2. It is worth remembering that the same result was obtained for the peaks appearance. Moreover, observing the condition (4.8) indicating the limit for the peaks appearance, and the relation (4.25), it is clear that the first phenomenon can exist in absence of the second one but not vice versa. Fig. 4.3 shows the limits represented by the two inequalities for a range of values of coupling and quality factor. The graph clearly shows that the limit represented by (4.8) is always under the red curve of (4.25). The two limits become coincident for very weak ($k \to 0$) or very high coupling ($k \to 1$). The behaviour of module and phase of the transmitter current for different values of coupling is depicted in Fig. 4.4a and Fig. 4.4b. The curves at $k = 0.08$ and $k = 0.1$ show that, although the current peaks are present, the phase crosses the zero degrees

(a)

(b)
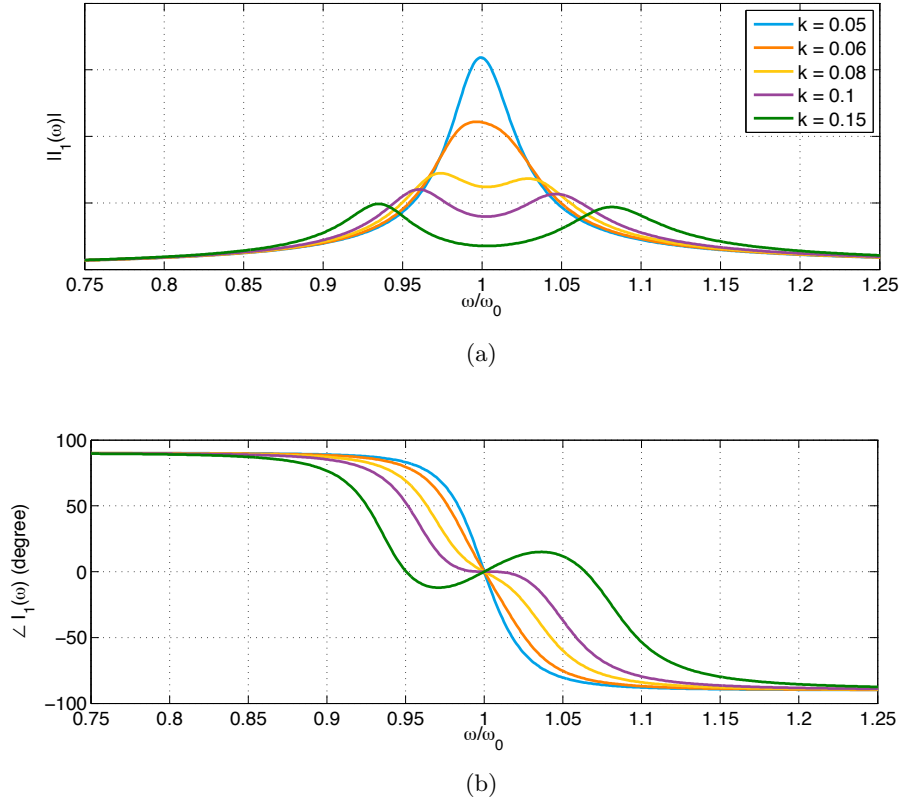
Figure 4.4: Effect of the variations of coupling on amplitude (a) and phase (b) of the transmitter current for a quality factor $Q_2 = 10$.

axis at a unique point. The appearance of the two additional angular frequencies ω_1 and ω_2 starts by deforming the phase and only at higher values of coupling the phase clearly crosses the zero degrees axis at three different points. In that case the behaviour of Z_T in the proximity of the resonance angular frequency ω_0 becomes very unstable and it can rapidly vary due to possible variations of the coupling. Fig. 4.5 shows that the behaviour in correspondence of the peaks is not purely resistive.

4.4   Unsymmetrical tuning

So far, the presented phenomena have been analysed under the condition of equal and perfect tuning of the resonance frequency on both transmitter and receiver side. This condition is not practically achievable in reality due to the tolerances in the components manufacturing. This means that the relation (4.14) is not usually valid and each side of the systems has a specific resonance angular frequency defined as:

$$
\begin{cases}
\omega_{0,1}^2 = \dfrac{1}{L_1 C_1} & (4.27) \\[2ex]
\omega_{0,2}^2 = \dfrac{1}{L_2 C_2} & (4.28)
\end{cases}
$$
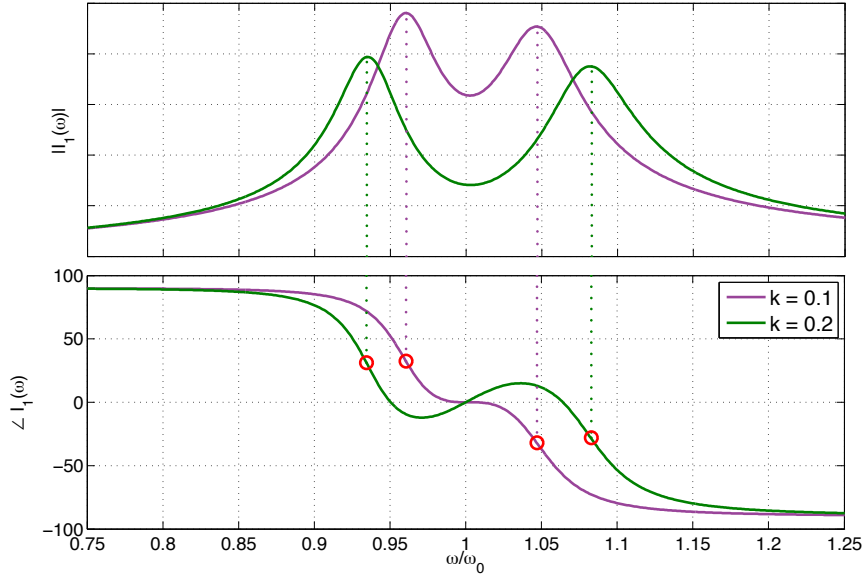
Figure 4.5: Details of the phase in correspondence of the two current peaks.

This asymmetry changes the behaviour of $\hat{Z}_T$ in amplitude and phase in a way dependent on the difference between $\omega_{0,1}$ and $\omega_{0,2}$ but also on the relative difference between these two angular frequencies and the ideal global resonance angular frequency ω_0. In the amplitude response the current curve becomes larger and the peaks amplitude changes dependently on the side where the detuning is predominant. In particular, as shown in Fig. 4.6a, if the capacitive component on the transmitter side increases (C_1 increases or C_2 decreases) the left peak lowers whereas the right one increases. The effect is exactly dual if the capacitive component is smaller than in the ideal case (C_1 decreases or C_2 increases) as shown in Fig. 4.6b. The figures indicate that the value of the current in correspondence of the original angular frequency ω_0 is almost the same. Conversely the phase is not still equal to zero. As shown in Fig. 4.7, the unequal tuning causes a translation of the phase modifying also the crossing condition of the zero degree axis. It is possible to reformulate (4.20) through the use of the two different resonant angular frequencies obtaining a new expression:

$$\omega = \omega_{02} \sqrt{\frac{(2Q_2^2 - 1) \pm \sqrt{1 + 4Q_2^2 \left(Q_2^2 k^2 \frac{\omega_{02}^2}{\omega_{01}^2} - 1\right)}}{2(1 - k^2)Q_2^2}} \qquad (4.29)$$

In that case the presence of the multiple-zero-crossing points is also dependent on the tuning asymmetry.
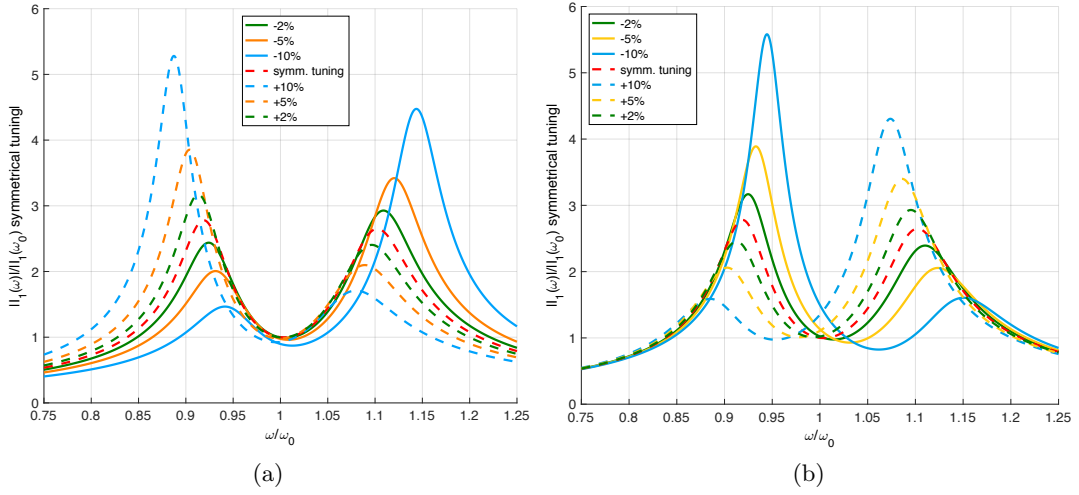
Figure 4.6: Effect of relative variations of the compensation capacitances on transmitter side (a) and receiver side (b) on the shape of the transmitter current.
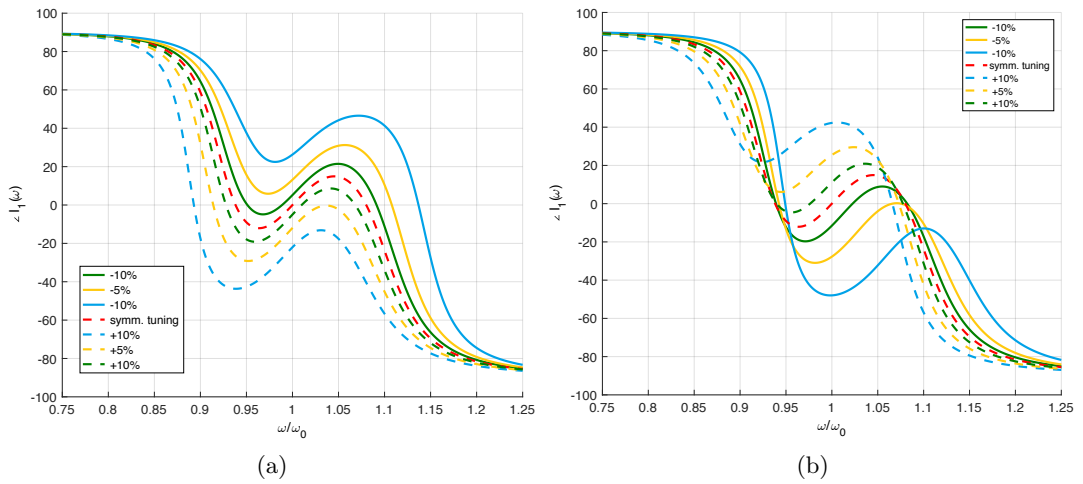
Figure 4.7: Effect of relative variations of the compensation capacitances on transmitter side (a) and receiver side (b) on the phase of the transmitter current.
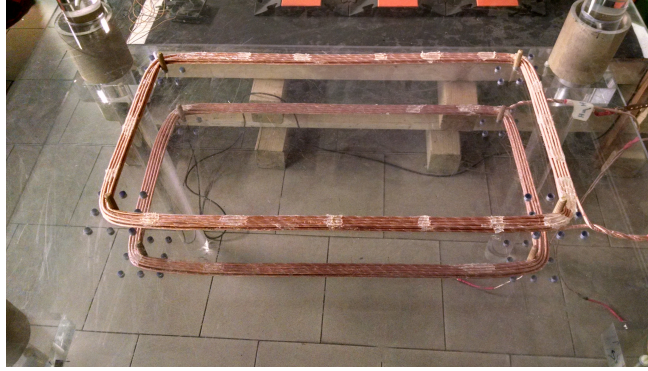
Figure 4.8: IPT prototype for the testing the frequency behaviour.
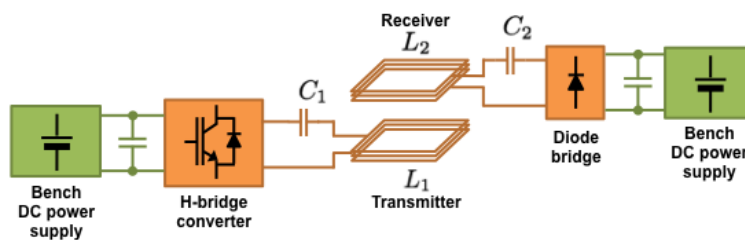
Figure 4.9: Setup for testing the frequency behaviour.

4.5   A practical demonstration

An experimental demonstration of the effects of the not symmetric tuning is provided through the simple prototype for IPT depicted in Fig. 4.8. The arranged test scheme is depicted in Fig. 4.9. The coils are supplied with an H-bridge having adjustable switching-frequency and both DC sides are connected to a DC voltage source at 27.9 V.
 The self-inductance of the coils is 90 μH $\pm 1\%$ and each coil is series compensated. The tests have been performed through the use of different ceramic capacitors in order to obtain a precise regulation of the value of compensation capacitance. The symmetrical tuning condition has been performed with a capacitance of 15 nF on each side in order to resonate at 137 kHz. In two subsequent tests the capacitance on the receiver side has been modified obtaining an increase of 10% and a reduction of 7% with respect to the symmetrical case. The resulting measurements are shown in Fig. 4.10. In this system the phenomenon of the multiple-zero-crossing is not present whereas it is clear the presence of the two peaks in the currents. These peaks move dependently on the sign of the mistuning and their value increase as a function of the mistuning level. The current values are almost constant around the original resonance frequency, conversely the phase of the transmitter current is not long zero.
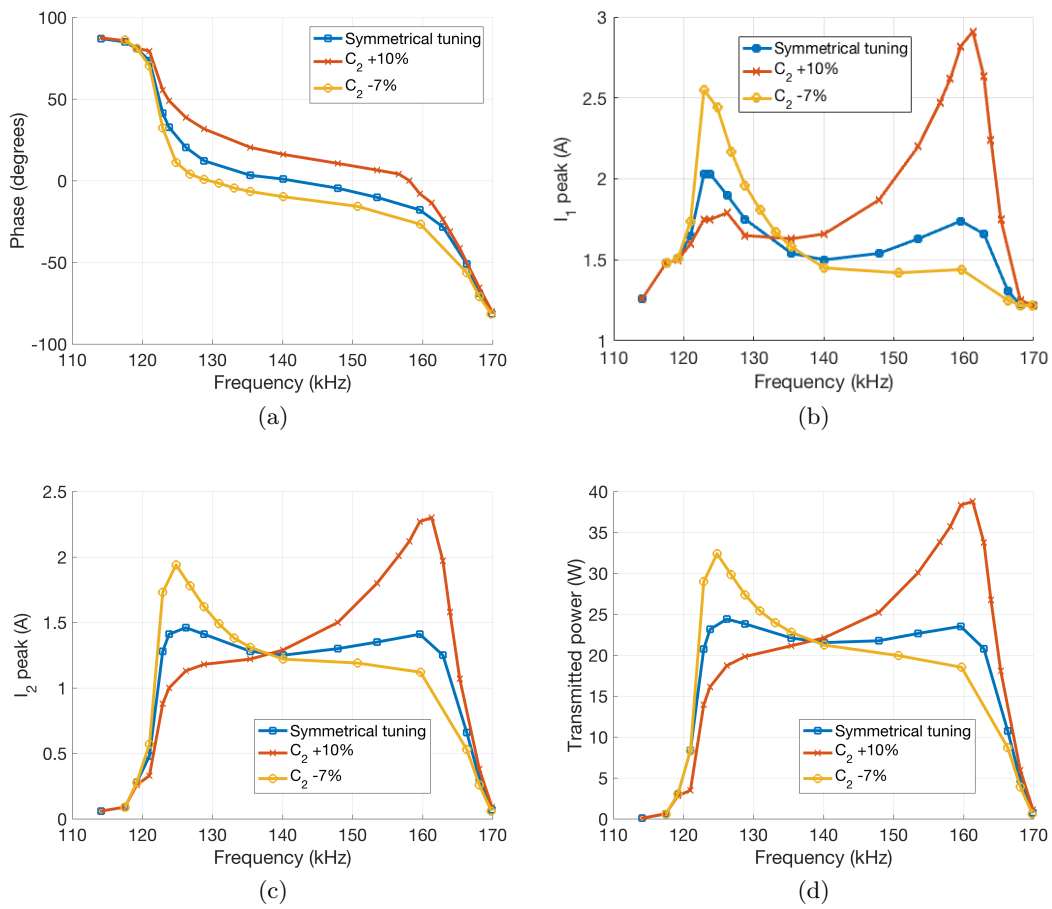
Figure 4.10: Behaviour of the system versus supply frequency for different conditions of tuning. Phase (a) and of peak (b) of the transmitter current, peak of receiver current (c) and transferred power (d).

4.6   Conclusions

This chapter illustrated and provided an analytical study of two important phenomena that characterise IPT systems: the current peaks and the multiple- zero-crossing. It is shown that these phenomena can be avoided, or at least minimised, in the design phase. Nevertheless, it is not possible to exclude their appearance in the dynamic applications due to the intrinsic variation of the coupling during the vehicle movement. Moreover, the unavoidable presence of uncertainties on the manufacturing of the reactive components adds another level of complication that cannot be precisely predicted. Hence, these phenomena have to be carefully considered during the design of the power electronics as well as in the control of the commutations. For the sake of simplicity, the principal implications are here summarised:

- The presence of multiple-zero-crossings introduces a sharp variation in the phase of $\hat{Z}_T$. This mirrors in the equivalent behaviour of the system with respect to the source in the proximity of the resonance frequency.

- The tolerances in the components can amplify this phenomenon increasing the values of the current peaks.

- A mistuning of the resonance frequency between transmitter and receiver can cause the increase of the current peaks and a translation in frequency of the point at zero phase (resistive behaviour).

For the power electronics this opens two possibilities:

- To work at variable frequency at the point with zero phase angle. This allows to be always in the conditions for the soft-switching but it needs a robust and fast regulation of the voltages in order to keep the currents at the rated values.

- To work at constant frequency and design the power electronics in order to be capable to manage both slightly inductive or capacitive commutations.

Chapter 5

Power electronics design

The next two chapters discuss the design process for the realisation of the prototype for dynamic IPT specifying the basic issues and constraints and illustrating the adopted choices and methodologies. The complexity of the system has demanded efforts in different fields of engineering starting from the project of the "electric device" itself arriving to its installation on vehicle board and the integration into the electrical network and the road infrastructure. In this chapter the processes that have led to the development of the power electronics are presented and discussed.

5.1 Adopted vehicle and power level of the application

The IPT system has been oriented to the installation on a full electric light commercial vehicle shown in Fig. 5.1. The vehicle has been provided by Centro Ricerche FIAT (CRF) as partner of the eCo-FEV and FABRIC projects. The main dimensions of the vehicle are reported in Table 5.1. The vehicle characteristics have been used to identify a proper power rating of the IPT system able to fulfil the power consumption within a reasonable speed. A parallel analysis has taken into account the possible employment of the system for an electric passenger car in order to investigate the possibility to generally extend the use of the developed architecture also for this category
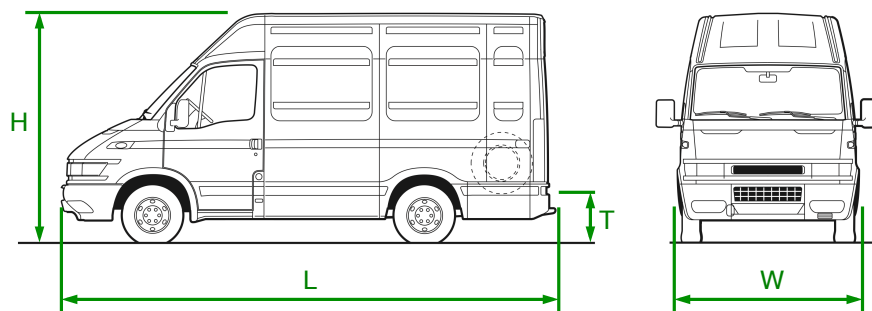
Figure 5.1: Adopted light commercial vehicle.

Table 5.1: Main dimensions of the reference light commercial vehicle for the development of the IPT system (ref. to Fig. 5.1).

Parameter	Description	Value
W	Maximum external width	2 m
L	Maximum external length	5.6 m
H	External height	2.7 m (min.) - 2.8 m (max.)
T	Height of loading area	735 mm (min.) - 775 mm (max.)

of vehicles.

The main quantities that contribute to the vehicle consumption are the *rolling resistance force* F_{roll} and the *aerodynamic force* F_{aer}. Naturally, if the vehicle is accelerating, an *inertial force* has to be taken into account as well as the *gravitational force* if the vehicle is moving on a certain slope.

Rolling resistance is defined as the energy consumed by a tyre per unit of covered distance [78, 79] and is expressed by means of the *rolling resistance coefficient* C_r. C_r is defined as the sum of two terms, one independent of the vehicle speed v and a second one that is function of the square of the speed and expressed by two coefficients indicated as f_0 and f_v respectively:

$$C_r = f_0 + f_v \cdot v^2 \tag{5.1}$$

These two parameters depend on materials and conditions of the tyres and on the characteristics of the ground. The global effect on the vehicle consumption depends on the normal components of the weight with respect to the soil. For a generic slope angle φ, the rolling resistance is defined as

$$F_{roll} = C_r \, m \, g \, cos(\varphi) \tag{5.2}$$

where m is the mass of the vehicle and g is the gravitational acceleration.

The aerodynamic force contribution is due to the movement of the vehicle through the air so it is dependent on the air density ρ and the aerodynamic characteristics of the vehicle. It can be expressed as

$$F_{aer} = \frac{1}{2}\rho A_f C_x v^2 \tag{5.3}$$

A_f is the *frontal area* that corresponds to the projection of the frontal vehicle profile onto a vertical plane [79]. C_x is the *drag coefficient* that correlates the frontal area and the resistance to the movement through the air. The lower the coefficient, the more aerodynamic the vehicle. F_{aer} is strongly dependent on the vehicle speed and it is the main parameter that influences the consumption.

The evaluation of the consumption has been done in a steady-state condition

Table 5.2: Aerodynamic parameters of adopted for the power consumption estimation.

Parameter	Value		Unit
	Commercial vehicle	Passenger car	
f_0	0.014	0.012	
f_v	$2.3 \cdot 10e^{-7} \cdot v^2$	$2.3 \cdot 10e^{-7} \cdot v^2$	$\left(\frac{m}{s}\right)^{-2}$
m	2500	1600	kg
C_x	0.6	0.32	
A_f	3.8	2.4	m^2
η_{pt}	0.8	0.8	

(constant speed) and in absence of slope ($\varphi = 0$). Hence, the contribution of the inertial and gravitational forces have been set equal to zero The sum of F_{roll} and F_{aer}, indicated as *motive force F_m*, is then expressed as

$$F_m = mgC_r + \frac{1}{2}\rho A_f C_x v^2 \tag{5.4}$$

The motive force times the vehicle speed gives the power at the vehicle wheels so, a parameter of efficiency η_{tr} is introduced to take into account the global efficiency of the power train (transmission, electric motor, power conversion). Finally the power consumption can be expressed as

$$P_{batt} = \frac{1}{\eta_{tr}}F_m v \tag{5.5}$$

that is the power demanded to the battery in function of the vehicle speed.

The values adopted for the analysis are reported in Table 5.2. They have been partially derived by measurements and partially acquired from literature [79–83]. The resulting power consumption behaviours are shown in Fig. 5.2. According to the results, a rated power of 20 kW has been chosen for the IPT system. This power level is sufficient to fulfil the power consumption of the adopted commercial vehicle up to about 70 km/h but, at the same time, it is the same power rating that could be adopted for a highway installation oriented to passenger cars.

According to the selected power rating, the vehicle has been equipped with a lithium-based battery having the main characteristics indicated in Table 5.3.

5.2 Compensation topology

The first choice at the base of the design has been the selection of the compensation topology. According to the analyses illustrated in Chapter 3, SS compensation has been considered the more suitable topology for the IPT application in dynamic. This topology has been preferred according to the following considerations:
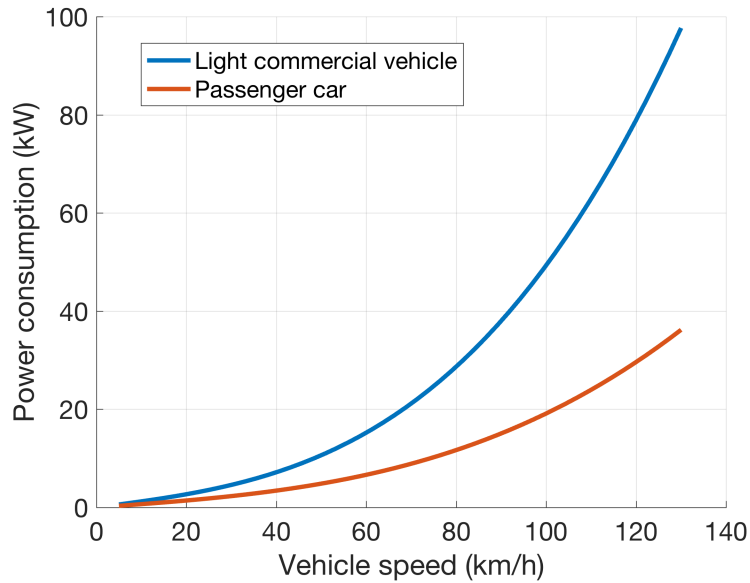
Figure 5.2: Power consumption of the adopted light commercial vehicle and a reference electric passenger car.

Table 5.3: Main electrical characteristics of the vehicle battery (at 25 °C).

Parameter	Value
Nominal capacity	75 Ah
Nominal voltage	370 V
Lower limit voltage	270 V
Upper limit voltage	420 V
Pulse current max	750 A

- Being the application oriented toward moving vehicles without autonomous guidance or mechanical system for the coil alignment, fluctuations of the coupling are unavoidably present. The SS compensation is the only one completely unaffected by the variation of the coupling with respect to the resonance condition.

- According to the selected power level of the applications, the series compensation allows to reduce the voltage supply at a manageable level. The system presented in [65] can provide again a good example. In the presented PP compensated system, a voltage of 1.6 kV is used to transfer about 2 kW. Without any change in the magnetic structure, that means no changes in the total impedance, the transfer of 20 kW needs for a voltage source of 5 kV. The use of a lower voltage allows the use of MOSFET or MOSFET-like components i.e. transistors of different technologies having similar characteristics in terms of operating voltage and current. This kind of component entails a better efficiency of the commutations and the possibility to operate at a higher frequency According to (3.16) and (3.51) the increase of the frequency is an effective way to transmit power

over large air-gaps (low mutual coupling) with a good efficiency.

- The system can be directly supplied with a voltage-source-converter (VSC) without the necessity of additional inductances for the compatibility of the commutations as happens for the hybrid compensations. This means no extra-costs, lower weight and complexity of the system.

Naturally the SS compensation presents some disadvantages that have to be taken into account during the design. The most important one is the unavoidably large voltage drop over the reactive components. This phenomenon is more relevant the weaker the coupling as the system tends to behave like a simple series resonant circuit [52, 74] (ref. Section 3.4). From a practical point of view, the voltage drop represents an important limitation for the compensation capacitors as the supported maximum voltage decreases at high frequencies in comparison to the rated DC value. An example is reported in Fig. 5.3 for a polypropylene film capacitor. In the design phase this aspect can be mitigated by reducing the self-inductance of the coils demanding a smaller impedance to the compensation capacitance then a lower voltage drop for an equal value of the current.

From the power electronics side, a weak coupling means also the necessity to adopt a fast and robust control that can react in case of sudden absence of load as the current in the transmitter becomes equal to a short circuit current.
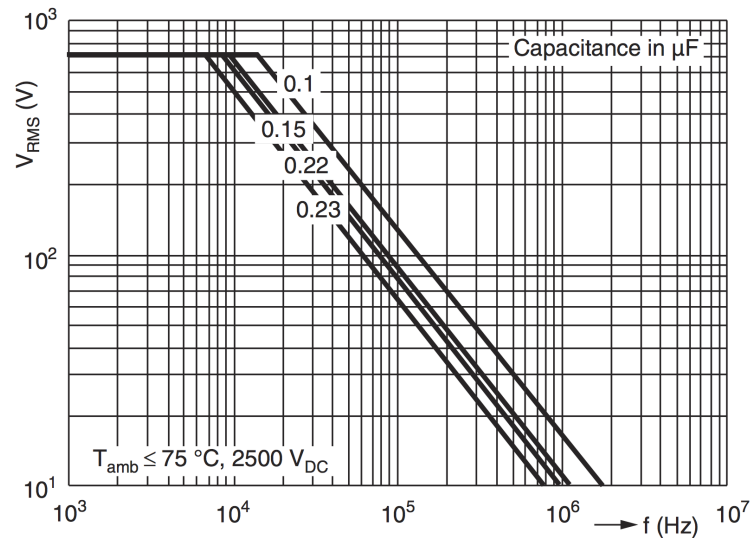
Figure 5.3: Maximum AC voltage in function of the frequency for a high voltage polypropylene film capacitor.

5.3 Power electronics overall architecture and control

The compensation topology influences the behaviour of the system from the points of view of source and load. The study of this behaviour is necessary to understand

in which way it is possible to manage the received power and by means of what kind of power electronics structure. Let's restart from the two fundamental quantities introduced in Chapter 3 that are the open-circuit voltage and the total impedance:

$$V_{oc} = \omega_0 M I_1 \tag{5.6}$$

$$Z_\mathrm{T} = \frac{V_1}{I_1} = \frac{\omega_0^2 M^2}{R_\mathrm{L}} \tag{5.7}$$

R_L has been generically defined as the ratio between the current I_2 that flows in the receiver and the first harmonic of the voltage V_2 over a generic load connected to the receiver:

$$R_\mathrm{L} = \frac{V_2}{I_2} \tag{5.8}$$

According to the selected topology, the reference basic circuit is the one depicted in Fig. 5.4. At the resonance, the impedances of inductors and capacitors reciprocally
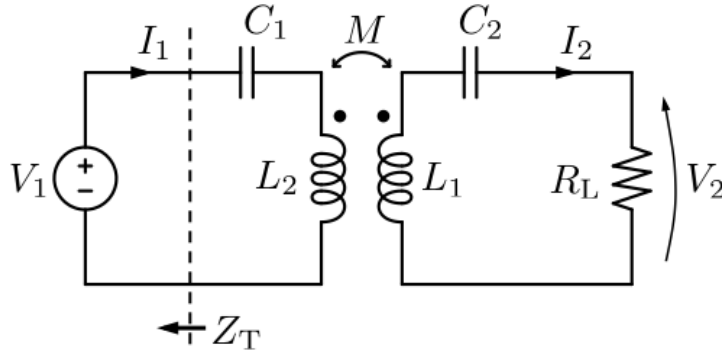
Figure 5.4: Basic circuit representation of the IPT system.

compensate, then the induced voltage V_{oc} and the voltage over the load are the same. Substituting (5.6) and (5.7) into (5.8), it is possible to find one of the fundamental relations of the power transfer:

$$I_2 = \frac{V_1}{\omega_0 M} \tag{5.9}$$

This relation indicates two intrinsic properties of the SS compensated IPT systems: the receiver current is independent of the load and it is possible to control this current acting on the voltage on the transmitter side. An exactly dual relationship can be found for the transmitter current rewriting (5.7) by using the definition of R_L provided in (5.8):

$$I_1 = \frac{V_2}{\omega_0 M} \tag{5.10}$$

Finally, (5.9) and (5.10) show that it is possible to control the currents on each side by regulating the voltage in the opposite side. This characteristics has been used in order to implement a control without communication loops between the two sides of

the system as the ones proposed in previous works on dynamic IPT [84–86]. This characteristic is strongly desirable for the dynamic applications for which the implementation of a communication between the road side and the vehicle can be difficult. This is all the more true the higher the speed of the vehicle.

Among the different possible solutions for the supply and control of the system, the one proposed in Fig. 5.5 has been chosen and implemented. An H-bridge has been chosen on the transmitter side whose DC bus is powered by an active synchronous AC/DC converter [87,88] that provides a stabilised voltage V_{DC} at 630 V. Differently
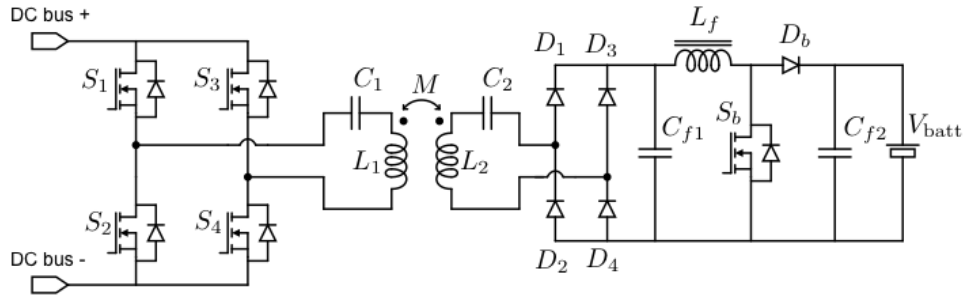
Figure 5.5: Block diagram of the overall architecture of the IPT system.

from previous works that adopted an intermediate DC/DC converter to control the transmitter current [24,54,89], the proposed converter works as a pure voltage source converter. With this structure the rms value of the voltage V_1 can be controlled through a phase shift technique at fixed frequency [61,90,91]. Each leg of the full-bridge is modulated with a complementary square wave as depicted in Fig. 5.6. The rms value of the output voltage is controlled by modulating the phase α between the complementary signal pairs according to the relation

$$V_1 = \frac{2\sqrt{2}}{\pi} V_{DC} \, sin\left(\frac{\alpha}{2}\right) \qquad (5.11)$$

The frequency of the voltage remains fixed at the resonance frequency of the system settled at 85 kHz. This value has been chosen to have a continuity with the static technology that is going to be commercially available. In fact this rated frequency is the one proposed by the standards SAE J2954 and ISO 19363 that are going to be the reference standards for the static IPT and the base for the future regulation on dynamic IPT.

The control of the receiver side is achieved by inserting a boost converter as interface between the diode bridge and the battery. The role of the boost is to control the voltage at the diode rectifier in order to regulate the voltage V_2. According to the battery parameters reported in Table 5.3, the boost has to operate between the upper and lower limit voltage of the battery. A rated value of 300 V has been chosen as rated voltage over the diode bridge in order to avoid operations in condition of deep
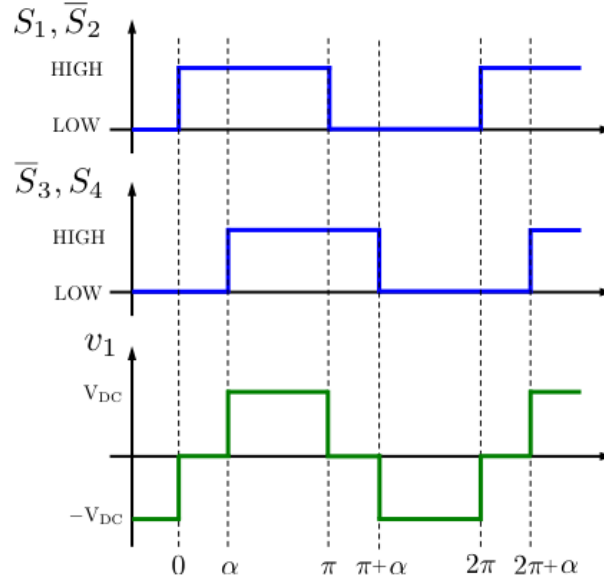
Figure 5.6: Example of waveforms of the phase-shift modulation. Command (gate) signals of the switches in blue. Output voltage of the DC/AC in green

discharge of the battery. The relationship between the voltage V_2 and the battery voltage depends on the duty cycle D of the switch S_b:

$$V_2 = \frac{2\sqrt{2}\,(1-D)}{\pi}V_{batt} \tag{5.12}$$

Finally, the fundamental relationships (5.9) and (5.10) can be rearranged according to the general system architecture as

$$I_2 = \frac{2\sqrt{2}}{\pi\omega_0 M}V_{DC}\,sin\left(\frac{\alpha}{2}\right) \tag{5.13}$$

$$I_1 = \frac{2\sqrt{2}\,(1-D)}{\pi\omega_0 M}V_{batt} \tag{5.14}$$

In the following, some aspects of the design and testing of the converters' structure is presented.

5.4 H-bridge design and testing

Several high power converters for IPT have been proposed in literature [54, 92, 93]. The general approach is to use several devices in parallel together with high current gate drives. In these applications, operation with *zero voltage switching* (ZVS) is required to keep the switching losses low if IGBT transistors are used. This applies also to MOSFET transistors because of the reverse recovery effects and high junction capacitance [94, 95]. This technique takes advantage of the characteristics of resonant

load of the IPT systems. In that case the transition of the switch in on or off state can be done when the voltage is practically zero. The technique can also be used to switch when the current, rather than the voltage, reaches zero. This technique is known as *zero current switching* (ZCS). Both ZVS and ZCS allow to reduce the switching losses practically to zero introducing also benefits in terms of reduction of electromagnetic interferences due to the hard-commutations [61, 62, 96, 97]. For these reasons these techniques are commonly called soft-switching techniques. Hard-switching operation is possible through the use of SiC MOSFETs, but with an increase in the cost of the components and the introduction of problems of possible thermal runaway at peak power [98].

The dedicated DC/AC converter developed in the present project presents several features that make it attractive for the dynamic IPT as high efficiency, low cost and small dimensions. In addition, the architecture of the converter has been thought to operate without ZVS in order to answer to the problem pointed out in Chapter 4 of the possible translation of the point at zero degrees phase in presence of tolerance errors in the components. The principle block diagram of the proposed structure is shown in Fig. 5.7.
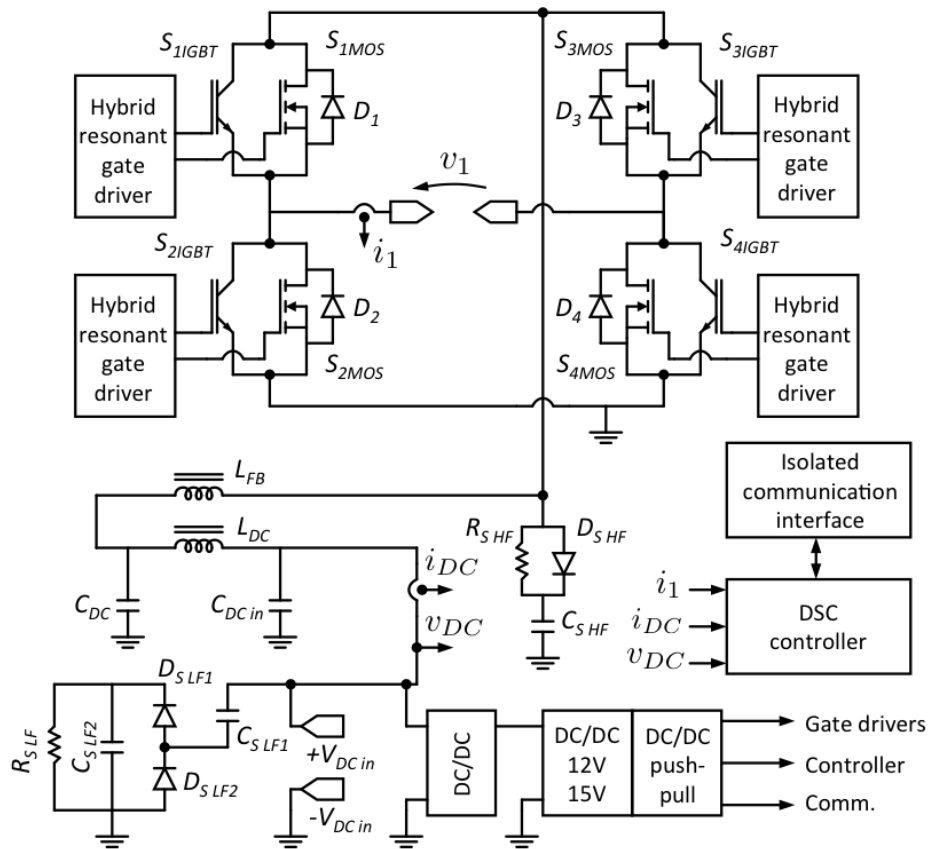
Figure 5.7: Block diagram of the supplying DC/AC H-bridge converter.

Each power switch is made with a low on-state voltage IGBT in parallel with a SiC MOSFET. This is a well known approach commonly indicated as hybrid switch [99, 100]. In rated conditions, the current is in phase with the transmitter input voltage so the peak of the current is carried by the IGBT and the turn-off is handled by the MOSFET. Because there is basically no reverse recovery, the turn-on can be done at high speed to minimise the losses while the additional capacitance of the IGBT helps to achieve partial ZVS at turn-off. The IGBT is switched on first with a high gate current to generate a fast transition. This reduces the power dissipation in the SiC MOSFET. The necessity to improve the efficiency also in hard-switching conditions derives also from the decision to control the system at fixed frequency. With a variable frequency control, the variation of the frequency can allow to follow the circuit resonance to more easily achieve soft-switching. As already discussed, the resonance frequency may drift from its nominal value in real conditions causing frequency stability problems or sharp increases of the currents. With the proposed fixed frequency control, the power transfer is more robust with respect to load and circuit parameters variations introducing also an important advantage in terms of EMC filters that have to be designed for a precise, known fundamental frequency [101].

According to the fast switching frequency of the circuit, the management of the circuit parasitics has been strongly considered [102]. Due to layout constraints, the main bus capacitor, C_{DC} is placed at a considerable distance from the transistors. In order to limit the over-voltage at the switching transients, additional ferrite beads, represented by the inductance L_{FB}, are placed together with an RCD snubber composed by $R_{S\,HF}$, $C_{S\,HF}$ and a SiC diode $D_{S\,HF}$. In this way some of the power loss is transferred from the transistors to the snubber resistor, increasing the power handling capability of the converter. As will be detailed in the next chapters, in the road prototype, the DC/AC converter is supplied by means of a DC distribution line. When the transfer to the vehicle begins, oscillations are generated between the self-inductance of the DC line and the input capacitance. To quickly damp and limit the amplitude of the oscillations, another RCD snubber is realised with $R_{S\,LF}$, $C_{S\,LF1}$, $C_{S\,LF2}$ and the diodes $D_{S\,LF1}$ and $D_{S\,LF2}$. An additional low pass filter with the components L_{DC} and $C_{DC\,in}$ is implemented to attenuate the high frequency ripple generated by the sinusoidal output current. The control of the converter is realised with an MC56F82746 digital signal controller (DSC). The board has been equipped with an isolated communications interface with CAN and RS485 to allow communications with other units in the vicinity. The gate drivers, control and communication circuits are supplied with a push-pull converter through isolation transformers with low capacitive coupling. The low voltage supply has been obtained from the main DC input by using two DC/DC converters. The adopted power switches have been the IGBT IRG7PH46U and the SiC MOSFET SCT2080KE. The realised prototype

is depicted in Fig. 5.8. The dimension of the board is 19×24 cm^2.
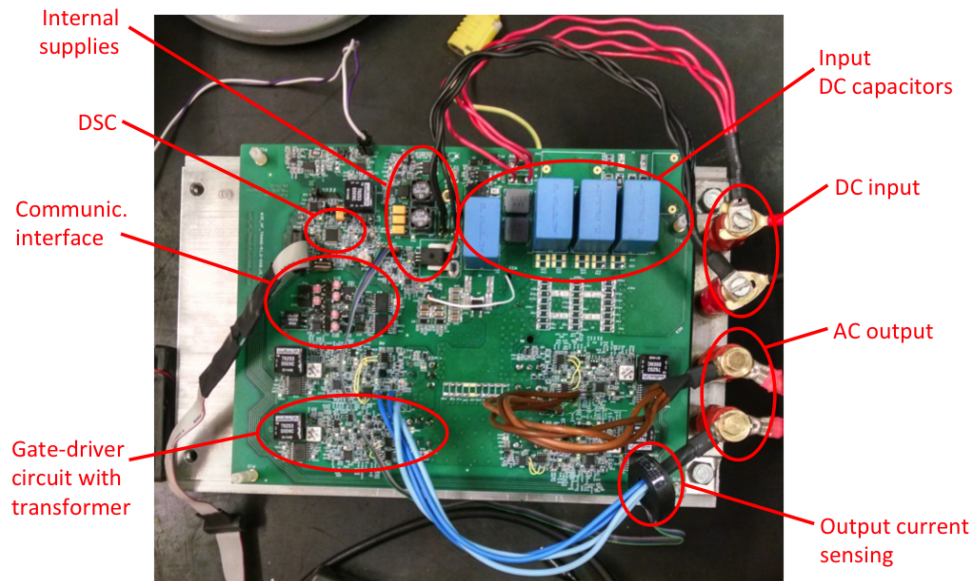
Figure 5.8: DC/AC converter prototype. The power switches are not visible as mounted on the bottom side.

The testing of the converter has been conducted by developing dedicated setups based on the *opposition method* [103–105]. It consists in the connection between two systems supplied by a common source the first one operating as generator and the second one as receptor. The aim is to circulate the full power through the two systems while the source has to supply only the losses of both systems. This technique presents several advantages. As the source has to provide only the losses, its power can be widely lower than the rated power of the system under test. The same concept mirrors on the load side where the introduction of a dissipative load can be avoided. Lastly, the losses and the efficiency can be directly evaluated with a good accuracy by measuring voltage and current at the DC source output.

The first test has been based on the configuration shown in Fig. 5.9 supplying the system at the nominal voltage. In relation to the described principle, one of the legs operates as a generator, the other as a receptor. A DC current has been imposed through an inductive load by manually setting the duty cycle and fixing the duty cycle of the generator leg to 50%. Therefore, the modulation of the generator leg is close to the modulation of the receptor leg. Nevertheless, a slight difference is required to compensate for the voltage drop across the inductor and the forward voltages of switches and diodes. Two conditions in which the IGBT or the MOSFET turns on first have been investigated. As this test has been used to evaluate the efficiency of the converter, the inductor L_1 was a simple air-core inductor that introduced negligible losses in the system. The measured efficiency in the two cases is shown in Fig. 5.11 for
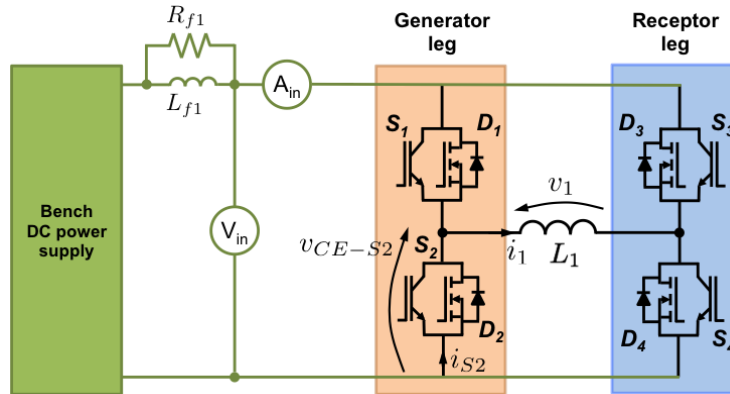
Figure 5.9: Test setup for the implementation of the opposition method for an IPT system.

different values of the current. It is worth noting that the system has been tested until a power level of about 6 kW according to the source limitations. Nevertheless, the test demonstrated that the converter is able to operate in hard-switching conditions with an efficiency higher than 98%. As visible through Fig. 5.10, this high efficiency makes easier to implement the cooling solution: the converter can be mounted over a very small heat sink preserving the necessity of reduced dimensions of the overall device.
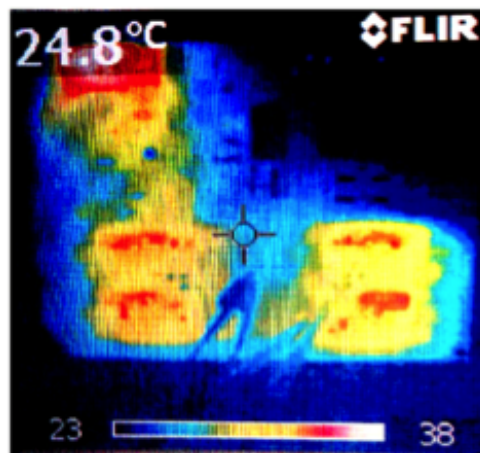
Figure 5.10: Thermal image of the converter during the test.

For the second test, the converter has been employed in a complete IPT system. The setup is depicted in Fig. 5.12. It consists of a closed loop where the DC output of the diode bridge that manages the power of the receiver is connected to the same DC bus of the DC/AC converter under test. In this way, if the bus voltage is the nominal one, the system can be tested at nominal power while the DC supply has to compensate only for the system losses. In general, the application of this method needs for a strong inductive filtering in the interconnection of the two DC stages in order to minimise the interferences of the two equivalent voltage source, but, in this case,
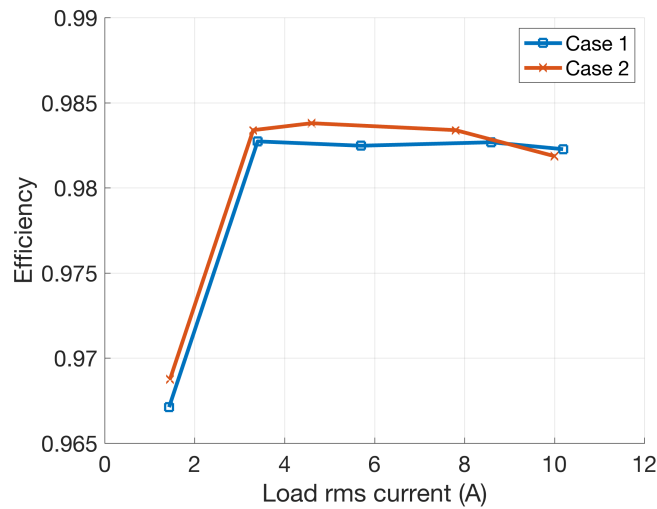
Figure 5.11: Measured efficiency with the opposition method. Case 1: IGBT turns-on first. Case 2: SiC MOSFET turn-on first.
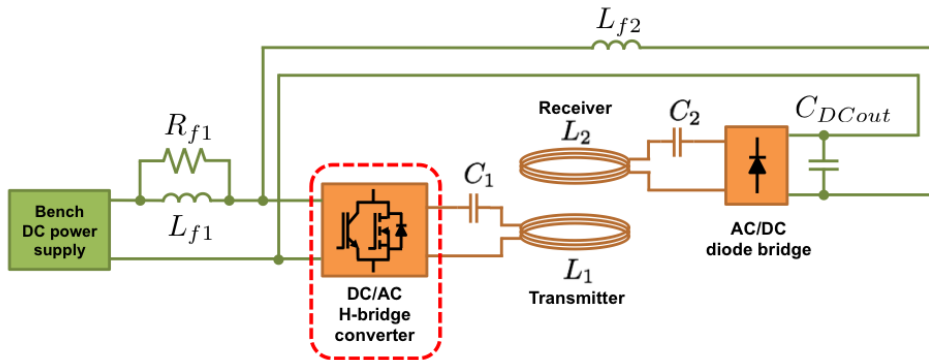
Figure 5.12: Test setup for the implementation of the opposition method for an IPT system. The converter under test is surrounded by the red dashed line.

just a small inductor L_{f2} is sufficient thanks to the current source behaviour of the receiver. The inductor L_{f1} and the resistor R_{f1} work as filter for the compatibility of the connection with the DC bench supply. The waveforms for ZVS and hard-switching are shown in Fig. 5.13 while the parameters of the main converter and the test benches components are presented in Table 5.4. The different working conditions have been obtained by slightly modifying the switching frequency of the converter. This test demonstrated the capability of the realised converter to handle both soft and hard switchings verifying the absence of the problem of the *conductivity modulation lag* that can be present for IGBT working at high frequencies of the tested application [106–108].

Table 5.4: Main parameters of the converter and components of the test bench.

Parameter	Reference	Value/Model
IGBT	S_{xIGBT}	IRG7PH46U
SiC MOSFET	S_{xMOS}	SCT2080KE
DC link filter capacitor	C_{DC}	15 μF
DC input filter capacitor	$C_{DC\,in}$	5 μF
Input filter inductor	L_{DC}	900 nF
Ferrite bead inductors	L_{FB}	FBMJ4516HS720NT
Snubber resistor AC side	$R_{S\,HF}$	100 Ω
Snubber capacitor AC side	$C_{S\,HF}$	30 nF
Snubber diode AC side	$D_{S\,HF}$	C4D02120E
Transmitter inductance	L_1	240 μH
Transmitter series capacitor	C_1	15 nF
Receiver inductance	L_2	120 μH
Receiver series capacitor	C_2	30 nF
Interconnection inductor	L_{f2}	1 mH
Diode bridge output capacitor	C_{DC2}	15 μF

5.5 Hardware protection of the receiver

(5.9) and (5.13) have shown that the receiver can be assimilated to a current source. This implies that all the components on the receiver side are intrinsically protected against the short-circuit. On the contrary the open-circuit represents a dangerous condition especially for the capacitor C_{f1} at the diode bridge output. In case of load disconnection, the current flowing in the receiver should continue to charge this component causing a rapid increase of its voltage until the dielectric breakdown. In the same time, the absence of load means the absence of the effects of coupling on the transmitter that becomes a short-circuit.

A protection system has been developed to react against the accidental disconnection of the load. It has been inserted between the diode bridge and the boost converter close to the components that have to be protected. The scheme of the solution is shown in Fig. 5.14. It is based on the use of three Zener diodes D_{z1}, D_{z2} and D_{z3} and the thyristor T. The Zener diodes have been chosen in order to obtain an overall breakdown voltage of 450 V, that is a safe level also for the battery. If the voltage across the capacitor exceeds the total breakdown threshold, the Zener diodes start to conduct a certain current that flows also in the thyristor gate inducing the transition in the conduction state. The thyristor short-circuits the receiver forcing the discharge of the capacitor lowering the voltage. Additional components are introduced to guarantee the correct functioning of the system in safe conditions. The resistors R_z and R_g limit the current flowing in the Zener diodes and in the thyristor gate respectively while the inductor L_t limits the variation of the current in the thyristor to a tolerable level. The diode D_g is used to avoid possible inversions of
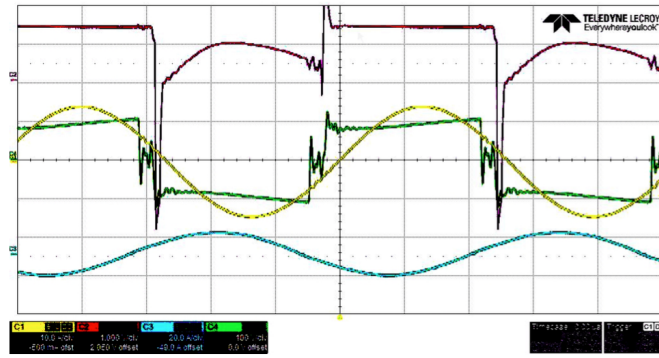
(a)
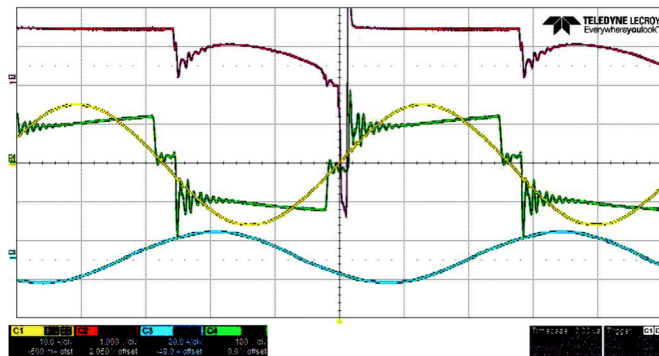
(b)

Figure 5.13: Waveforms of the DC/AC converter in the IPT system. Commutation for inductive load (ZVS) (a) and capacitive commutation (b). DC/AC output voltage v_1 in green 100 V/div, output current i_1 in yellow 10 A/div, receiver current i_2 in cyan 20 A/div, collector-emitter voltage v_{ce} measured at the S_2 switches terminals in purple (1 V/div).

the gate current caused by the oscillations established by the capacitor that resonates with its parasitic self-inductance after the step variation of the voltage. The chosen components have been three Zener diodes 1N5333B with a breakdown voltage of 50 and 200 V whose current has been limited to 4 A through the resistor $R_z = 100 \ \Omega$. The model of thyristors is an MCO150-12io1 that can conduct a steady-state current of 150 A with a maximum forward surge current of 2 kA. This high value is necessary to tolerate the peak of current injected by the capacitor in the first instants of the thyristor activation. The short circuit drastically forces the voltage over C_{f1} to pass from 450 to 0 V in about 5 μs so the capacitor reacts with a current pulse. The variation of the current in the thyristor is limited to its critical rate of rise of 500 A/μs thanks to the inductor L_t having value equal to 2.5 μH.

The system has been tested by means of a DC bench supply as source instead of the diode bridge and in absence of the filter capacitor. Fig. 5.15 shows as, when the voltage of the supply reaches the overall breakdown threshold of the Zener diodes, the protection systems acts as desired short-circuiting the supply. The short-circuit causes the intervention of the over current protection of the supply whose turn off is followed
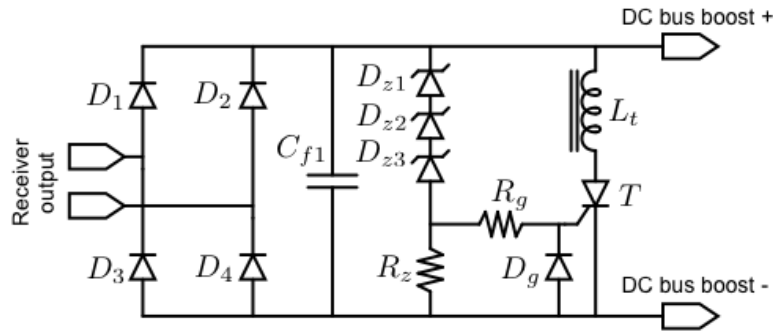
Figure 5.14: Scheme of the protection system in case of load disconnection.

by oscillations due to the discharge of the internal reactive elements of filtering. The
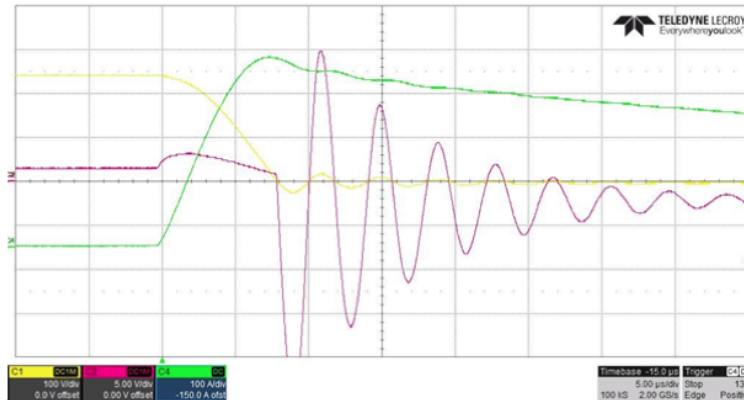
Figure 5.15: Waveforms of the testing of the receiver protection system with two zener diodes (breakdown threshold of 250 V). DC bench supply voltage in yellow (100 V/div), current in the thyristor branch in green (100 A/div), voltage over the diode D_g in purple (5 V/div). Time axis 5 μs/div.

mechanical realisation of AC/DC converter with the filter capacitors and the tested protection system is shown in Fig. 5.16.

5.6   Conlusions

In this chapter the methodology and the design choices followed during the development of the power electronics of the system have been presented. The developed system is supplied at a fixed frequency of 85 kHz with a series-series compensation. A compact, low cost and high efficiency DC/AC converter with soft or hard switching capabilities has been realised and tested. The preliminary experimental results indicated an efficiency of 98% at about 6 kW. The method for the testing has represented an important outcome as it provided a generally applicable solution that allows to operate with a high flexibility and in safer condition eliminating the necessity of a source able to manage the full power of the system.
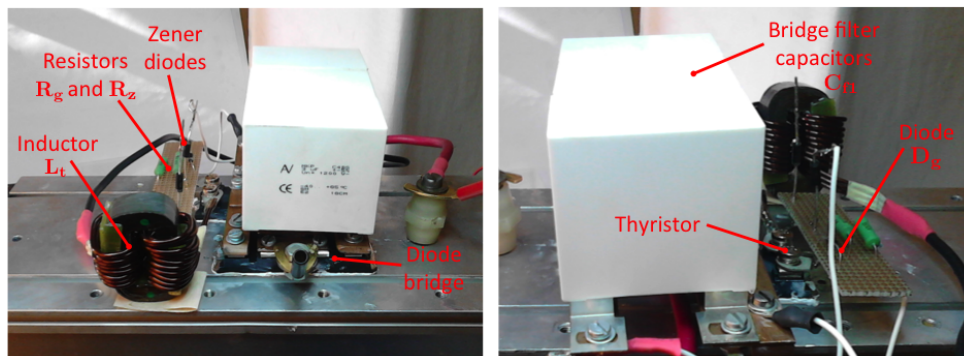
Figure 5.16: Mechanical realisation of the AC/DC converter with filter capacitors and protection system.

Chapter 6

Magnetic structure design and electromagnetic modelling

Continuing the description of the design process, in this chapter the development of the magnetic structure of the IPT system is presented. It concerns the development of the system of transmitter coils that have to be placed under the ground and the structure of the receiver that has to be mounted under the vehicle floor.

6.1 Receiver placing

The selected vehicle typology provides the constraints on the dimension of the structure that has to house the receiver coil. In fact the designed system has been thought for the installation on an existing vehicle without requiring modifications on the original framework. The two available positions for the mounting are located as illustrated in Fig. 6.1 and the related volumes have dimensions equal to 150 cm × 50 cm × 50 cm. A ground clearance of 18 cm with respect to the receiver is considered sufficient to
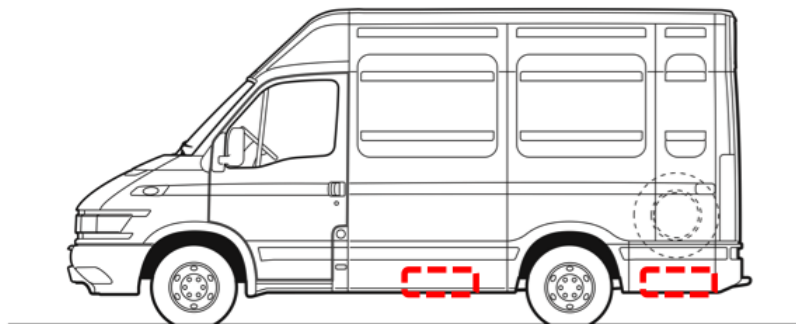
Figure 6.1: Allowed positions for the receiver structure mounting without modification of the vehicle framework.

guarantee absence of damages during the motion according to the indications provided in the ISO/DPAS 19363 standard [33].

6.2   Transmitters characteristics

As introduced in Chapter 1, the shapes of the transmitters presented in literature are fundamentally of two typologies: the long track coil and the small coil of the same dimension of the receiver. The principal advantage of the long track coil consists in a continuous power transfer as the vehicle moves along the track. The track can be energised when the vehicle is over the coil using a single source converter. Moreover, if the dimension of the coil is sufficiently long, the detection of the vehicle does not need to be extremely precise and very fast [109]. However, as the dimension of the transmitter is much longer than the receiver, the long section of not coupled coil causes the presence of a strong stray field. The stray field can represent a problem in terms of electromagnetic compatibility with the on-board electronic devices but also an important problem in terms of exposure to the people in the vicinity of the vehicle [110]. Structures with small transmitters reduce these problems but do not allow a continuos power transfer and require a very fast and precise vehicle detection system [111].

In the present work, a compromise solution has been implemented. It consists in the adoption of long transmitters whose dimensions allow that each coil, when energised, is completely covered by the shape of the vehicle also in conditions of misalignment. This concept is illustrated in relation to the adopted vehicle in Fig. 6.2, but it can be applied also to common passenger cars whose typical dimensions are 4.4 m in length and 1.8 m in width[1] [112]. According to the developed power electronics, this solution allows to transfer the power to one vehicle at a time in a more continuous way than a series of small transmitters but, at the same time, it allows an easier containment of the stray field with respect to a solution with the coils longer than the vehicle. The adopted internal dimensions are 1.5 m in length and 0.5 m in width.
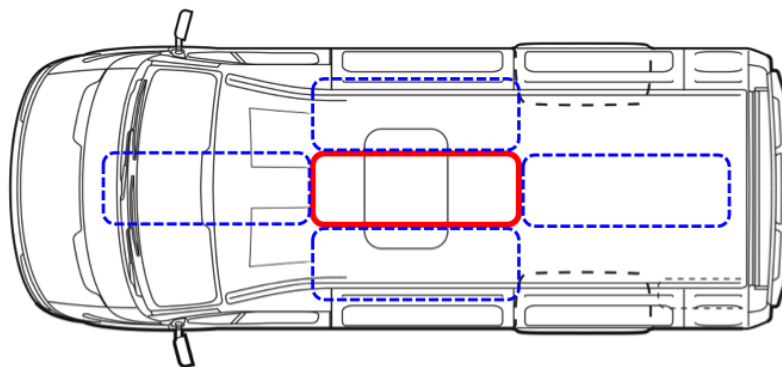
Figure 6.2: Comparison of the transmitter and vehicle dimension. Dashed lines represents different possible positions of the coil corresponding to a misplacement of 100% with respect to the centred case in red. Only one vehicle can be physically present over the active coil.

---

[1]Values extracted as average among 30 compact cars and 30 family cars from the reference web database.

For the final realisation, it has been decided to place the transmitters on a layer at 5 cm below the pavement surface. This choice has led to a nominal distance between transmitter and receiver of 25 cm.

6.3   Preliminary data for design and optimisation

Having fixed the geometrical constraints, the fundamental information for the design of the magnetic structure results from the nominal characteristics of the power electronics on both sides. The system has been designed in such a way as to transfer the nominal power $P_{nom} = 20$ kW (nominal voltage and current on both side) in condition of nominal mutual inductance M with a supply frequency equal to the global resonance frequency of the system ($\omega = \omega_0$). The mutual inductance M has been selected as main design parameter as it links the two sides of the IPT system and influences the power transfer. The preliminary design does not consider the losses as typically done in the first design phase of classical electrical machines.

6.3.1   Nominal mutual inductance

To obtain the desired value of M, the values of total impedance and equivalent load are evaluated in relation to the respective nominal parameters of the power electronics. In nominal conditions, the output voltage of the transmitter is a square wave of duty cycle 50% ($\alpha = 0$ in (5.11)) and amplitude equal to the nominal voltage of the DC bus $V_{DC} = 630$ V. The rms value I_1 of the output current is approximately equal to 36 A. These values provide a total impedance

$$Z_{\mathrm{T}} = \frac{V_1}{I_1} = \frac{\frac{4}{\pi\sqrt{2}}V_{DC}}{I_1} \approx 15.8 \ \Omega \tag{6.1}$$

The evaluation of R_{L} needs for some additional steps in order to reflect the ratio of voltage and current from the DC to the AC side. The different components of the receiver and the voltages and currents of interest are reported in Fig. 6.3 and Fig. 6.4 respectively. The voltage v_2 at the diode bridge input is a square wave whose amplitude is equal to V_{2DC} (has similarly happens on the transmitter side at nominal conditions). The amplitude of V_{2DC} is regulated by the boost converter that decouples the system from the battery voltage V_{batt}. Then, the relation between the peak of the first harmonic of v_2 and the rectified output is:

$$\hat{v}_{2,1h} = \frac{4}{\pi}V_{2DC} \tag{6.2}$$

The sinusoidal current i_2 induced in the receiver is rectified obtaining the current i_{2b}. The rectified current I_{2DC} is the average value of i_{2b} assuming an ideal behaviour of

the capacitor C_{f2} that filters the harmonic content of the current [61]. This description can be translated in the following relations:

$$i_{2b} = |i_2| \tag{6.3}$$

$$I_{2DC} = \bar{i}_{2b} = \frac{2}{\pi}\hat{i}_2 \tag{6.4}$$

At the nominal condition, the boost regulates a nominal voltage $V_{2DC} = 300$ V that means a current I_{2DC} of about 67 A. The value of the equivalent load can be then calculated as:

$$R_{\mathrm{L}} = \frac{\hat{v}_{2,1h}}{\hat{i}_2} = \frac{8}{\pi^2}\frac{V_{2DC}}{I_{DC}} = 3.65 \ \Omega \tag{6.5}$$

At this point it is possible to reuse the expression of the total impedance (5.7) to find
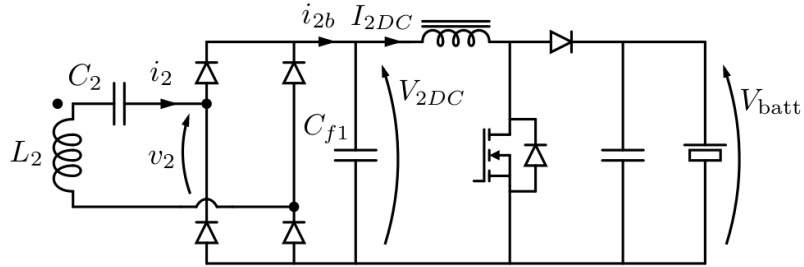
Figure 6.3: Scheme of the receiver power electronics stages with the reference voltages and currents.
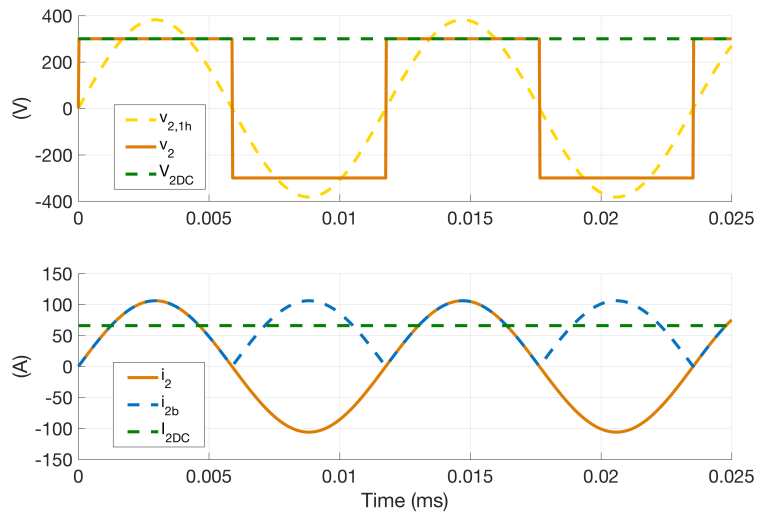
Figure 6.4: Waveforms of voltage and current of the series compensated receiver in presence of rectifier and ideal capacitive filter.

the desired value of nominal mutual inductance:

$$M_{nom} = \frac{\sqrt{Z_T R_L}}{\omega_0} \approx 14.2 \ \mu H \qquad (6.6)$$

6.3.2 Cross section and material of the conductors

The values of the currents on the transmitter and receiver provide the starting information for the selection of the characteristics of the coil wires. The cross section of the conductors depends on the selection of a current density in relation to the cooling system. In the present case the cooling is simply obtained by natural air convection on both sides so a value of current density of 4 A/mm^2 is considered an acceptable reference. This value can be slightly exceeded on the receiver side according to the vehicle movement that works as air-cooler if the heat is effectively extracted from the coil. On the other side, lower value can be adopted for the transmitter as it is located under the ground in a condition that does not allow a good thermal exchange.

The wire cross section influences also the coil resistances and the self-inductance. As indicated in the two works dedicated to the calculation of self and mutual inductances of wires and coils [113] and [114], the value of self-inductance is inversely proportional to the cross section of the wire. The minimisation of the values of self-inductance is an important parameter on which to act in order to minimise the voltage drop across the reactive elements. Nevertheless, the selection of the section has to face with related aspects of cost, technical realisation and management of the connections and space availability. According to these considerations a wire cross-section of 16 mm^2 has been selected for the coils on both sides. This cross-section leads to a value of current density of about 2.3 A/mm^2 on the transmitter and 4.7 A/mm^2 on the receiver.

For the realisation of the coils, a particular kind of wire called *litz wire* has been adopted. The litz wire is particularly suited for the high-frequency applications where the presence of skin and proximity effects cause a relevant increase of the AC resistance. As illustrated in Fig. 6.5, the litz wire consists of many enamelled thin copper strands twisted together often involving several levels (groups of twisted wires are twisted together, etc.) [115, 116]. It strongly reduces the skin effect and decreases the AC resistance by replacing the mono-wire by numerous smaller single wires resulting in the same cross section. The winding pattern equalises the proportion of the overall length over which each strand is at the outside of the conductor. The diameter of the single strand is chosen to be smaller than the skin depth δ at the working frequency:

$$\delta = \sqrt{\frac{2}{\sigma \omega_0 \mu}} \approx 0.25 \ mm \qquad (6.7)$$

where σ is the copper conductivity equal to about 50 MS/m and μ is the magnetic
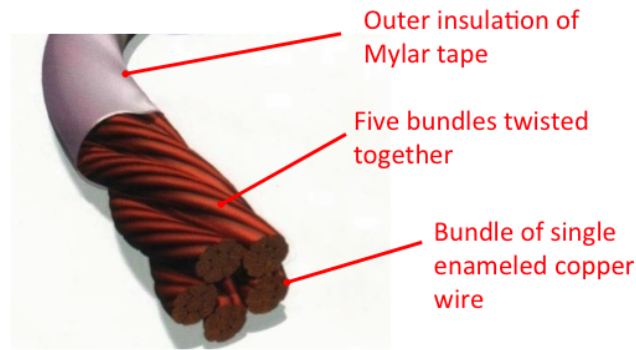
Figure 6.5: Illustration of the litz wire construction.

Table 6.1: Parameters of selected litz wire

Parameter	Value
Net wire section	16 mm^2
Single strand diameter	0.1 mm
Total number of strands	2050
Number of groups	5
Gross wire section	23.8 mm^2

permeability that, for the copper, is equal to the one of vacuum $\mu_0 = 4\pi 10^{-7}$ H/m. Finally, the parameters of the selected wire are reported in Table 6.1. Each single strand is insulated through a solderable enamel in polyurethane having a temperature class of 180 °C. The external insulation is constituted by two layers of Mylar tape, a polyethylene film with a dielectric strength of 193 kV/mm, for a total thickness of 24 μm.

Other classical conductor solutions for the reduction of the skin effect are the conductive hollow pipes with a wall thickness approximately equal to the skin-depth [117, 118] or copper straps [119]. With respect to these possibilities, the litz wire offers a higher flexibility that translates in a faster realisation at lower cost and a natural higher resistance to compression that are particularly desirable properties for the integration under the road pavement.

6.3.3 Preliminary shape of magnetic structure

Although the fixed inner dimensions of the transmitter, the wire section and the geometrical constraints on vehicle board, the value of M_{nom} can be obtained in many different ways acting on the dimension of the receiver coil and on the number of turns on both sides.

A preliminary sizing of the coil has been done by using two air-coupled rectangular coils as the ones depicted in Fig. 6.6, numerically evaluating the mutual inductance. Each coil has been treated as a polygon whose sides are subdivided into smaller seg-

Table 6.2: Coil parameters for the preliminary sizing

Parameter	Value
Transmitter width	0.5 m
Transmitter length	1.5 m
Transmitter number of turns (N_1)	9
Receiver width	0.55 m
Receiver length	0.4 m
Receiver number of turns (N_2)	9

ments. Each segment forming the transmitter has been considered as a conductor carrying a current I_0 in order to compute its effect in terms of magnetic flux density over the surface of the receiver coil applying the Biot-Savart law for thin wires [120]. The surface of the receiver has been split into triangles then he value of M has been obtained by integrating the normal components of the magnetic flux density B_n though the 16 points rule Gauss quadrature [121, 122]:

$$M = N_1 N_2 \frac{\int_\Omega \vec{B} \cdot \mathrm{d}\vec{S}}{I_0} \tag{6.8}$$

The extracted preliminary dimensions are reported in Table 6.2 and the obtained value of M is 14.6 μH.
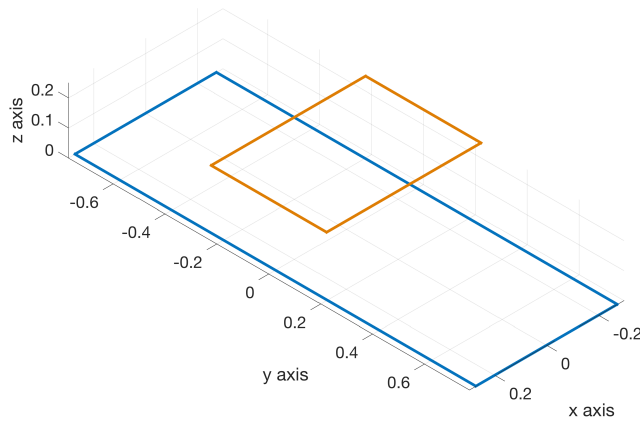
Figure 6.6: Air-coupled rectangular coils for the preliminary sizing. Transmitter in blue and receiver in orange.

Nevertheless, the use of simple coils is not suited for the EV applications as they give rise to a not well penned field that illuminates the vehicle floor and the areas in the vicinity with related problems in terms of induced losses, EMC and exposure to people that may be in the proximity of the vehicle. Moreover, the mutual coupling becomes dependent on the complex geometry of the vehicle that, acting as a conductive shield, can deform the magnetic field distribution. For all these reasons, a combination of ferromagnetic and conductive materials has been added in order to confine the

magnetic flux in a better defined region and lowering the leakage flux independently of the geometry of the underside of the vehicle. The desired ideal shape of the flux lines is sketched in Fig. 6.7. They perfectly link the coils remaining in a well defined path on the underside of the vehicle as happens in the coils of a transformer with an E-shape core. This is naturally impossible in presence of the large air-gap of the IPT for EVs.
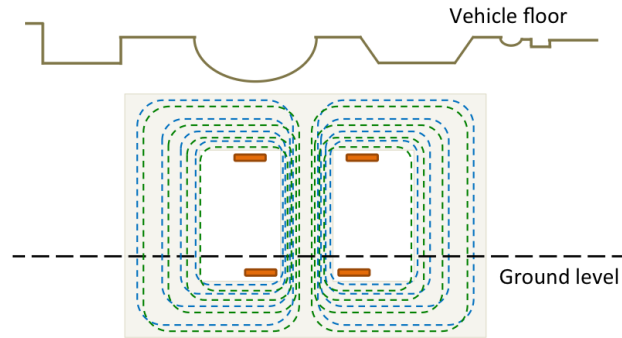
Figure 6.7: Ideal shape of the flux lines.

The basic idea of the creation of the auxiliary structure for the receiver consists in trying to obtain this ideal shape using ferromagnetic materials to create a preferential low-reluctance path for the flux lines and inserting conductive sheets to mold the magnetic field distribution tending to the ideal shape. A qualitative representation of the desired effects is given in Fig. 6.8 where the red lines represent the conductive elements while the blue ones represent the boundaries of the ferromagnetic elements. The arrows indicate the desired effect of deformation over the flux lines. The insertion of ferromagnetic elements is necessary to compensate for the coupling decrease due to the shielding effect of the conductive elements but also to reduce the induced losses by lowering the perpendicular component of the flux that invests the conductive surfaces.

The obtained preliminary geometry of the system is depicted in Fig. 6.9. The different conductive sheets are connected together in order to create a unique shielding structure that can simplify the mechanical realisation and the mounting. Moreover, it has been decided to create a contact between the ferromagnetic material and the shield in order to make the most from this last component using it also as a heat sink. Two possible materials have been considered for the shield construction: 1100 aluminium alloy and 304 stainless steel. The principal characteristics of interest are reported in Table 6.3 [123]. The 1100 aluminium is a wrought alloy in the commercially pure alloys family. It contains a minimum of 99% of aluminium and it is the mechanically strongest alloy of the same series. The second one is the most common stainless steel also know as 18/8 steel. Both materials offer a good resistance to corrosion and a good workability. With respect to aluminium, steel offers a better mechanical workability as it can be easily bended and welded but, on the other side, aluminium is three
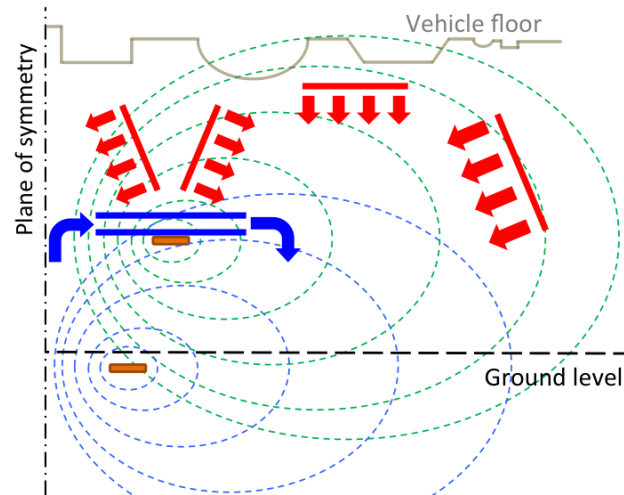
Figure 6.8: Desired effect on the shape of transmitter and receiver flux lines by means of the insertion of ferromagnetic (blue) and conductive materials (red). Only one side is represented as symmetric with respect to the other one.
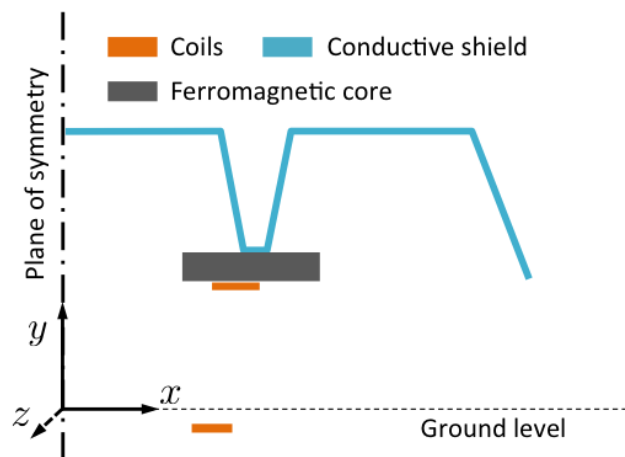
Figure 6.9: Scheme of the preliminary geometry of the magnetic structure

times lighter and offers electrical and thermal resistance of one order of magnitude lower. Finally, for the prototype realisation, aluminium has been considered the most suitable material as it can guarantee a lighter solution with a lower value of induced losses thanks to its high conductivity.

3F3 ferrite has been chosen for the ferromagnetic elements. Although ferrites have a good magnetic permeability, they are basically non-conductive so they are particularly appropriate to work at high frequencies. In particular, 3F3 ferrite offers a stable value of permeability $\mu_r = 2000$ at the working frequency of the application and very low specific power losses. The main parameters are summarised in Table 6.4. The most critical cons of ferrite is its fragility. This characteristic has to be taken into account during the design providing for adequate housing and damping against vibrations.

Table 6.3: Properties of 1100 aluminium and 304 stainless steel.

Parameter	Value	
	1100 aluminium	**304 steel**
Electrical conductivity	33.45 MS/m	1.38 MS/m
Magnetic relative permeability	1	1.02
Thermal conductivity	222 W/(mK)	16.2 W/(mK)
Specific Heat Capacity	904 J/(kgK)	500 J/(kgK)
Specific weight	2710 kg/m^3	8000 kg/m^3

Table 6.4: Properties of 3F3 ferrite

Parameter	Value
Relative permeability @85 kHz and 0.25 mT	$2000 \pm 20\%$
Saturation flux density 80°C	≈ 300 mT
Specific losses @100 kHz, 100 mT and 80°C	< 80 kW/m^3
Electrical conductivity @25°C	0.5 S/m
Thermal conductivity $3.5 - 5$ W/(mK)	
Specific weight	4750 kg/m^3
Curie temperature	≥ 200°C

Differently from the majority of proposed solutions for dynamic IPT, the insertion of auxiliary materials is only limited to the receiver side. This choice has been made in order to obtain a strong reduction of the cost per meter of the system. The elimination of ferrite increases the ease in the road pavement maintenance and the robustness of the solution against vibration. As secondary relevant effect, the absence of ferrite helps to maintain a low value of self-inductance in relation to the significant length of the coil.

6.4   Optimisation process

The qualitative shape of the magnetic structure depicted in Fig. 6.9 has been improved through an optimisation process. According to the complexity of the geometry and the considerable number of variables, the optimisation has been carried out using a 2D simulation based on the finite element method (FEM). The goals of the optimisation have been the minimisation of the losses per unit of length on the shield, namely P_{loss}, and the maximisation of the coupling k. Starting with fixed dimensions of the transmitter, the maximisation of k means the maximisation of the ratio M/L_2. This choice aims then at increasing the system efficiency (ref. Section 3.6) minimising the voltage stress over the reactive elements on the receiver side. According to the material properties, the losses in the ferrite cores are neglected and the material considered as linear. This condition has been verified a posteriori after the optimisation process. A weight $P_{\text{max}} = 1$ kW/m has been introduced to combine the two goals in a single

objective function defined as:

$$f(k, P_{\text{loss}}) = \min\left[(1 - k) + \frac{P_{\text{loss}}}{P_{\text{max}}}\right] \tag{6.9}$$

The adopted variables for the optimisation are depicted in Fig. 6.10. Their description and the ranges of possible variation are indicated in Table 6.5. Proper constraints have been inserted in order to guarantee the mechanical feasibility of the solution according to the available spaces indicated in Section 6.1 and the safety of operations during the movement. As shown in Fig. 6.10, the presence of the vehicle floor has been taken into account by simply modelling this part with a steel sheet of 1 mm having magnetic permeability and conductivity $\mu_r = 200$ and $\sigma = 10$ MS/m. This element is functional to preliminarily consider the exposure constraints already in the design phase evaluating the magnetic flux density B over a plane coincident to the lateral side of the vehicle chassis. The adopted reference for the exposure compliance have
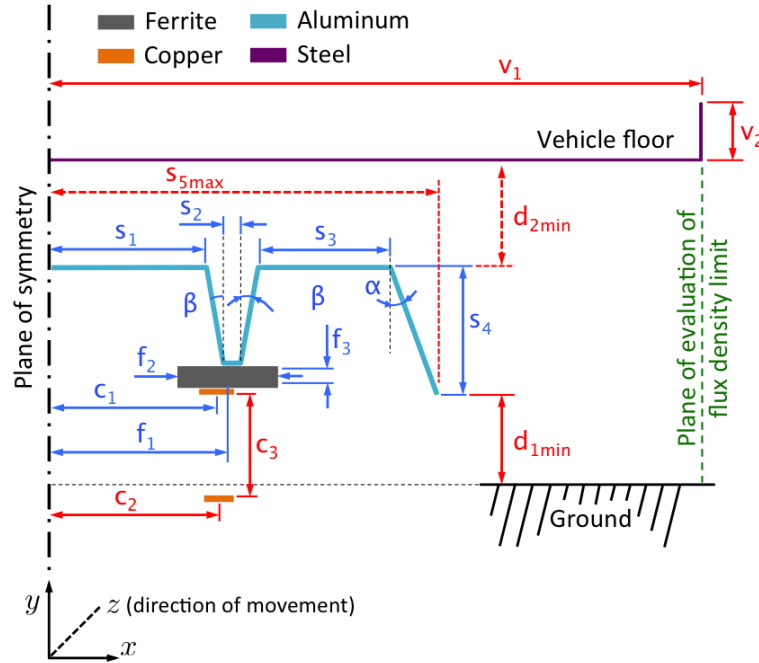
Figure 6.10: Scheme of the geometry to be optimised. Optimisation variables in blue. Fixed parameters in red. Optimisation constraints in dashed red.

been the ICNIRP guidelines of 2010 [124]. As will be better detailed in Chapter 8, these guidelines indicate a reference limit of 27 μT for the magnetic flux density at the frequency of 85 kHz. During the optimisation, the value of B is calculated along the green plane of Fig. 6.10. If at least one value exceeds the limit, a penalty factor assigned to the objective function causes the rejection of the current configuration.

The optimisation is carried out using a differential evolutionary strategy algorithm [125, 126] with the parameter set up indicated in Table 6.6. This optimisation

Table 6.5: Parameters of the optimised geometry and range of variation. Constraints in bold.

Parameter	Description	Values and ranges
c_1	Receiver coil semi-width	$0.1 - 0.4$ m
c_2	Transmitter coil semi-width	0.5 m
c_3	Coil distance	0.25 m
f_1	Ferrite core position with respect to the receiver coil center	± 0.05 m
f_2	Ferrite core width	$0.05 - 0.2$ m
f_3	Ferrite core thickness	$0.075 - 0.1$ m
s_1	Left shield section	$0.02 - 0.5$ m
s_2	Center shield section	$0.02 - 0.5$ m
s_3	Right shield section	$0.02 - 0.5$ m
s_4	Overal shield height	$0.1 - 0.3$ m
β	Internal bending angle	$0 - 80°$
α	Lateral bending angle	$0 - 80°$
$\mathbf{s_{5max}}$	Maximum total shield semi-width	0.7 m
$\mathbf{d_{1min}}$	Minimum allowed distance of the shield from the ground	0.19 m
$\mathbf{d_{2min}}$	Minimum allowed distance of the shield from vehicle floor	0.35 m
v_1	Vehicle floor semi-width	1 m
v_2	Vehicle floor lateral height	0.1 m

algorithm is particularly suited for constrained optimisation among several degrees of freedom allowing the use of techniques of parallel computing [126, 127]. Thanks to the symmetry of the solution with respect to the y-z plane (Fig. 6.10) it is possible to simulate only a half of the structure speeding up the computation. The process has been based on MATLAB and the freeware FEMM software [128]. The overall

Table 6.6: Parameters for the DE strategy optimisation

Parameter	Value
DoFs	10
Population size	50
Mutation ratio	0.8
Crossover ratio	0.5
Max. number of iteration	150

optimisation process is illustrated through the flow chart of Fig. 6.11. It starts with the random creation of the population i.e. fifty candidate solutions (i.e. fifty vectors that contain the ten variables for the optimisation). Each element of the population is tested in order to verify the compliance with the geometrical constraints. In case of not compliant geometry, a value of 10 is automatically assigned to the respective objective function. The assignment of this penalty naturally leads to the rejection of
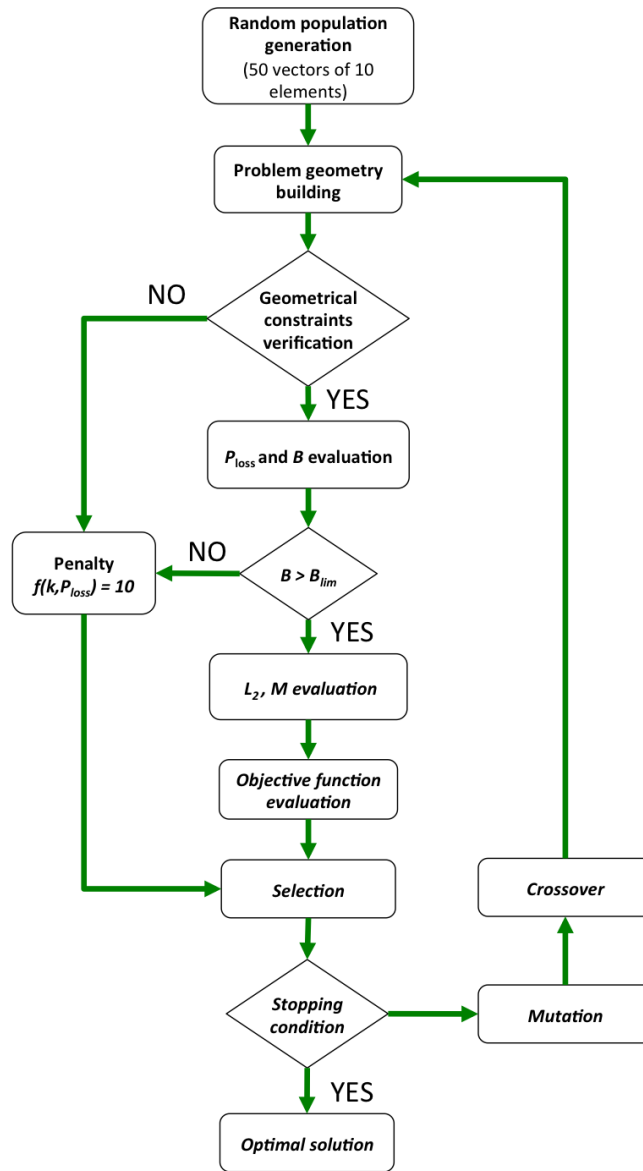
Figure 6.11: Optimisation process flowchart.

the candidate solution during the selection phase without demanding the immediate regeneration of the single vector. In case of compliance, the FEM simulation is carried out. The simulation runs a first time with the currents I_1 and I_2 fixed at the nominal values in order to evaluate the magnetic flux density along 300 points of the inspection lines and the losses per unit of length by integrating the induced current density in the chassis J_{ch} over its section S_{ch}:

$$P_{\text{loss}} = \rho \int_{S_{ch}} J_{ch}^2 \mathrm{d}S \tag{6.10}$$

After this first run, the respect of the limit $B < 27$ μT is checked. If the check is negative, the same previous penalty is assigned to the objective function otherwise the second simulation starts. This simulation is used to evaluate the self-inductance of the receiver and the mutual inductance so, in this case, the current I_2 is set to the nominal value while I_1 is fixed at zero. The self-inductance is evaluated integrating the scalar product of magnetic vector potential $\vec{A_2}$ and current density $\vec{J_2}$ over the cross section S_2 of the receiver and dividing for the square of the current imposed in the respective coil:

$$L_2 = \frac{\int_{S_2} \vec{A_2} \cdot \vec{J_2} \mathrm{d}S}{I_2^2} \tag{6.11}$$

The mutual inductance is evaluated over the transmitter coil as

$$M = \frac{N_1}{I_2 S_1} \left(\oint_{S_{1+}} \vec{A_1} \cdot \mathrm{d}\vec{S} - \int_{S_{1-}} \vec{A_1} \cdot \mathrm{d}\vec{S} \right) \tag{6.12}$$

In this case, the magnetic vector potential over the transmitter $\vec{A_1}$ is due to the current flowing in the receiver. The first term in brackets is the contribution from the induced current flowing in the transmitter that points out of the plane of simulation (in the cross section indicated as S_{1+}) and the second term is the contribution of the current that points into the plane (in the cross section indicated as S_{1-}). At the end of the two runs a new generation of candidate solutions is created by combining existing candidates (crossover) or modifying elements of the population (mutation) but keeping the candidate solution that has the best fitness (selection). The process is stopped after 150 iterations. Fig. 6.12 shows the convergence of the algorithm. The value of the objective function stabilises after the eightieth iteration also if a small improvement arrives on the last iterations. Its final value has been equal to 0.657 with a coupling $k = 0.344$ and a value of losses $P_{\mathrm{loss}} = 0.463$ W/m.
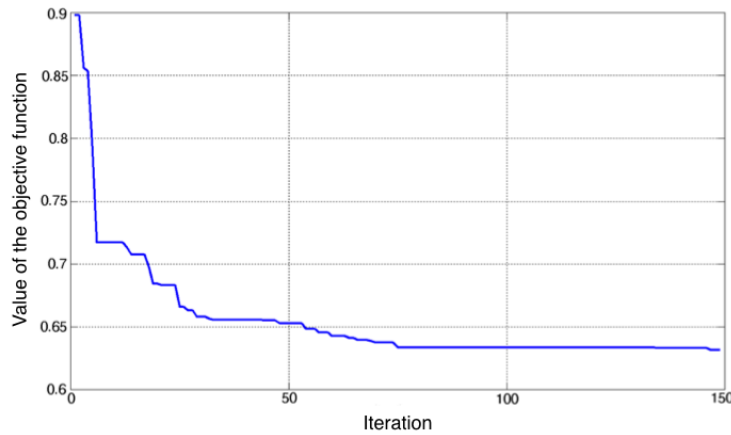
Figure 6.12: Convergence of the optimisation algorithm.

Table 6.7: Resulting parameters of the optimised geometry.

Parameter	Value	Parameter	Value
c_2	0.525 m	α	2°
s_1	0.23 m	β	4°
s_2	0.025 m	f_1	0.01 m
s_3	0.44 m	f_2	0.2 m
s_4	0.15 m	f_3	0.025 m
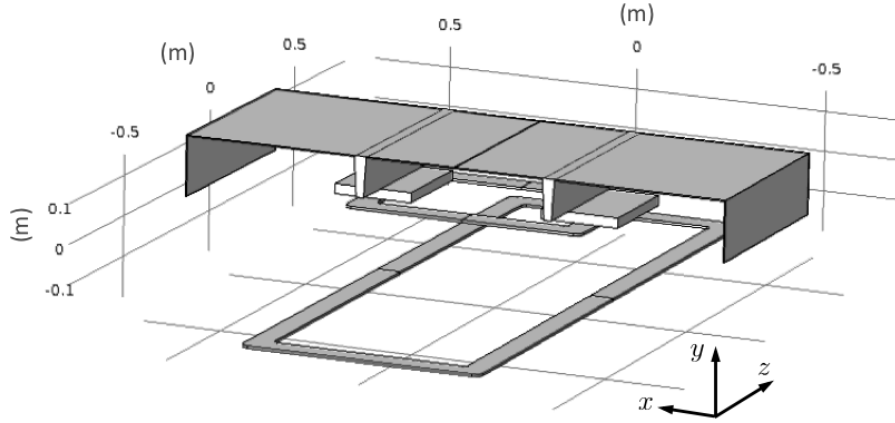
Figure 6.13: 3D model for the structure refinements.

6.5   Post-optimisation refinements

The optimisation process left the dimension in the direction of movement (z axis) as degree of freedom that has been used to obtain the desired value of mutual inductance together with the refinements of the number of turns. This final step has been conducted through a 3D model treated again using the finite element method. In this case the simulation has been conducted using the commercial software COMSOL [129]. The developed model is depicted in Fig. 6.13. With respect to the results of the optimisation, the angle α has been fixed at zero for the sake of the mechanical realisation of the structure considering that this operation does not entail a substantial modification of the result. The coils are treated as ideal massive coils [130] having height equal to the gross diameter d_{wire} and width equal to $N \times d_{wire}$ where N is the number of turns. The mutual inductance is calculated through the integral (6.13) over the volume of the receiver Ω_2:

$$M = \int_{\Omega_2} \frac{\vec{A}_2 \cdot \vec{J}_2}{I_1 I_2} \, \mathrm{d}\Omega \tag{6.13}$$

Table 6.8: Final parameters of the optimised geometry after refinements.

Parameter	Value
Transmitter length	1.5 m
Transmitter width	0.5 m
Transmitter num. of turns N_1	10
Receiver length	0.3 m
Receiver width	0.525 m
Receiver num. of turns N_2	10
Transmitter self-inductance L_1	279.5 μH
Receiver self-inductance L_2	120.8 μH
Mutual inductance M	14.3 μH

The self-inductance of each coil has been evaluated through a similar integral over its own volume setting the current to zero in the coil not interested by the calculation:

$$L_1 = \int_{\Omega_1} \frac{\vec{A}_1 \cdot \vec{J}_1}{I_1^2} \, \mathrm{d}\Omega \quad \text{for } I_2 = 0 \tag{6.14}$$

$$L_2 = \int_{\Omega_2} \frac{\vec{A}_2 \cdot \vec{J}_2}{I_2^2} \, \mathrm{d}\Omega \quad \text{for } I_1 = 0 \tag{6.15}$$

The aluminium shield is modelled applying the *surface impedance boundary conditions* (SIBC) [131, 132]. According to the high conductivity of the material and the high frequency of the application, the penetration of the electromagnetic field is limited to a very thin layer inside the shield of about the same thickness of the skin dept defined in (6.7) whose value is about 0.3 mm. The SIBC are particularly indicated in this case as they approximate the penetration of the magnetic field in the inner part of the material avoiding to include its domain in the model reducing the calculation efforts. The SIBC assume that the induced currents flow entirely on the surface of the material. The effects of the finite value of conductivity and permeability of the material are taken into account by means of an surface impedance that puts in relation the electric and magnetic fields on the surface of the object. The chassis is not considered in this analysis as it has not influence on the values of self and mutual inductance according to the presence of the receiver structure and the distance from both coils [57, 133]. After few trials, the final length of the receiver has been fixed at 0.3 m and the number of turns increased by one on each side. The final parameters of the magnetic structure resulted from the simulation are reported in Table 6.8. The same model has been used to provide a verification of the absence of saturation on the ferrite cores. As shown in Fig. 6.14 the maximum value of magnetic flux density inside the ferrite is about 100 mT, a value three times lower than the saturation level. This confirms the correctness of the hypothesis of linear behaviour of the ferrite done for the optimisation.
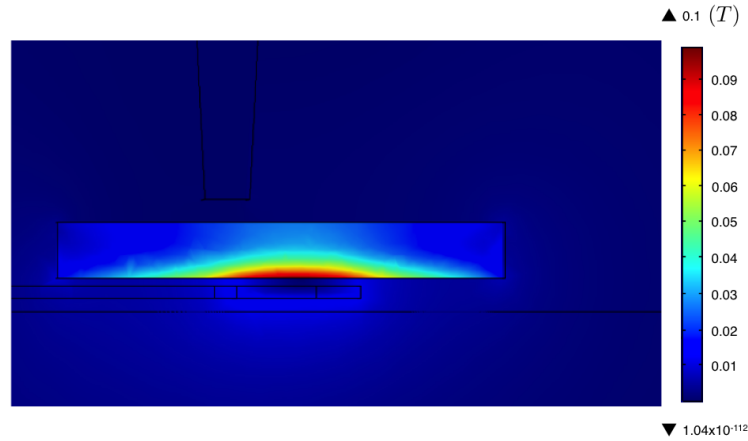
Figure 6.14: Colormap of the magnetic field density in the plane x-y with zoom over the section of the ferrite core.

6.6 Mechanical realisation

6.6.1 Receiver

The receiver structure has been reproduced by using a mechanical 3D CAD thanks to which all the auxiliary components for the realisation and the mounting under the adopted vehicle have been designed. The basic components are illustrated in Fig. 6.15. The aluminium of the main structure of the shield has been wrought through hot bending. The two internal parts have been realised as two aluminium trapezoidal beams in order to use them as main load-bearing elements for the entire structure. The receiver coil is placed over a U-shaped plate of Lexan that encloses and protects the entire active part. Lexan is a particularly tough transparent polycarbonate that can undergo large plastic deformations without cracking or breaking. The same material has been used to create a support working as a template to keep the coil and the ferrite in the right positions (Fig. 6.16a). Both Lexan elements have been thermoformed and worked through cold milling. The ferrite cores have been realised using twenty commercially available I-shaped bars, as the one shown in Fig. 6.16b, on each side. The bars are pressed together using a silicon glue. The same glue has been used to fix the internal Lexan plate to the external support. The structure is held together through eight main steel bolts on the frontal sides that fix the Lexan to the beams and other smaller bolts screwed on the lateral sides. A Sil-Pad has been placed between the coil and the ferrite bars and between these last and the beam. Sil-Pads are thermally conductive insulators based on silicon rubber so they can guarantee the insulation between the different elements creating a good path for the heat flow from the coil and the ferrite toward the aluminium structure. In order to strengthen the structure and guarantee a sturdy fastening to the vehicle framework, two C-shaped aluminium elements have been fixed to the shield and blocked on the underside of the external Lexan plate through two screwed aluminium bars (Fig. 6.17a). The
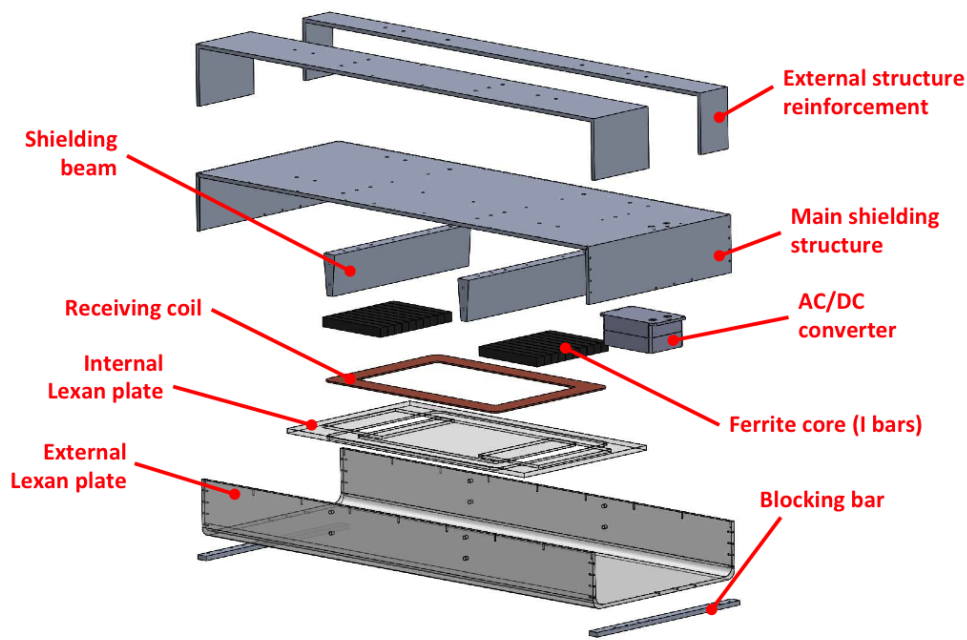
Figure 6.15: CAD model of the main components of the receiver structure.

mounting under the vehicle is provided by means of eight cylindrical stainless steel anti-vibration dampers, commonly called silent blocks, shown in Fig. 6.17b. These components protect the structure and the inner components from the vibrations during the movement of the vehicle. The compensation capacitors are inserted inside the structure together with the AC/DC stage. In this way the receiver can be connected directly to the DC/DC converter at a manageable voltage level. The AC/DC converter has been screwed to a heat sink welded to the aluminium shield and placed in a plastic case at the top of the structure where the presence of magnetic stray field is negligible according to the result of the simulations. The structure of the converter and its heat sink are visible in Fig. 6.18. The resulting assembled structure is visible in Fig. 6.19. It has been mounted under the vehicle in order to test the correct mechanical assembly that as been successfully achieved as visible in Fig. 6.20. In Table 6.9 are reported the weights of the developed components together with the total weight of the structure.

6.6.2   Transmitter

The mechanical realisation of the transmitter has been oriented to the creation of a light structure able to be carried and placed without risks of damage or deformation. For these reasons the coil has been formed over a base of fiberglass having a thickness of 5 mm and fixed through a series of bandages with a special tissue tape typically used for the construction of high frequency transformers. Additional fixings have been created by using classical plastic bands. The obtained structure, shown in Fig. 6.21,

<div align="center">(a)   (b)</div>
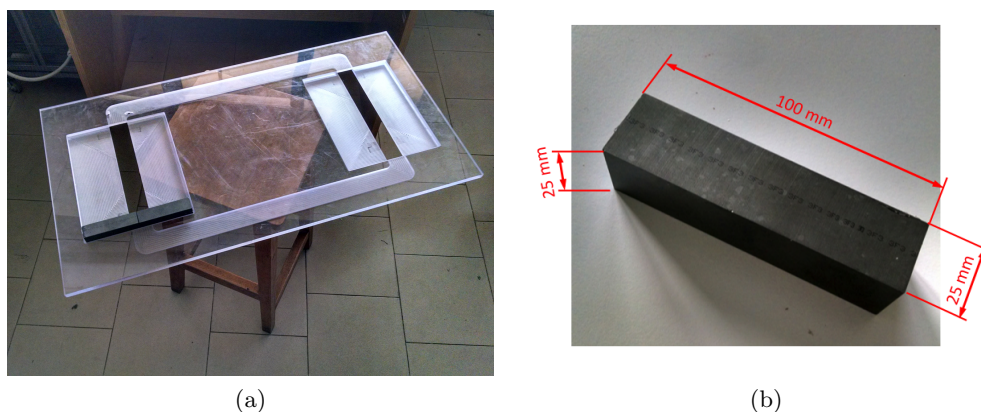
Figure 6.16: Lexan plate for the coil forming and the ferrite positioning (a) and bar of 3F3 ferrite adopted for the realisation of the ferrite cores (b). Two ferrite bars are visible in the dedicated housing into the plate.

Table 6.9: Weight of the receiver structure components.

Element	Quantity	Weight
Aluminium shield	×1	5.0 kg
C-shaped reinforcement (big)	×1	9.3 kg
C-shaped reinforcement (small)	×1	4.6 kg
Aluminium beam	×2	8.7 kg
Blocking bar	×2	1.0 kg
Receiver coil	×1	3.9 kg
Ferrite bar	×40	13.4 kg
Lexan plate	×1	3.2 kg
U-shaped Lexan plate	×1	10.9 kg
AC/DC + case + compensation cap.	×1	2.1 kg
AC/DC heat sink	×1	0.3 kg
Silent block	×8	1.6 kg
Total weight		64.0 kg

is robust and light and then particularly suited to be integrated on the road pavement as better described in the dedicated Chapter 7.

6.7 Measurements

The final magnetic structure has been tested by measuring the values of self and mutual inductance by using an HIOKI 3532-50 LCR HiTESTER LCR meter at the frequency of 85 kHz. This instrument measures the amplitude and the phase of the object under test applying an AC voltage. With these information it is possible to estimate the values of self-inductance and resistance of the coils. The first measurement has been made on the receiver coil terminals mounted in the magnetic structure and disconnected from the other electrical components. A self-inductance of 119.8 μH and
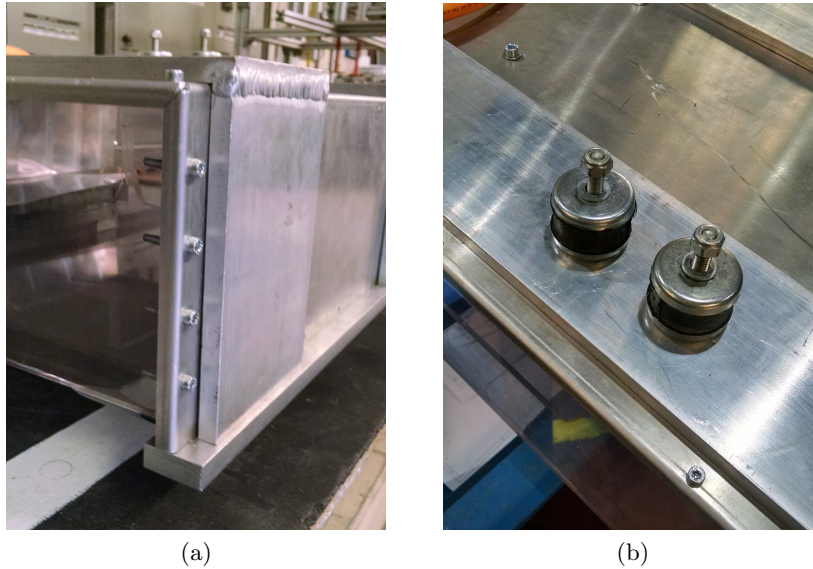
Figure 6.17: Details of the C-shape reinforcement structure with lateral screwing and blocking bar underside (a). Silent blocks dumpers (b).
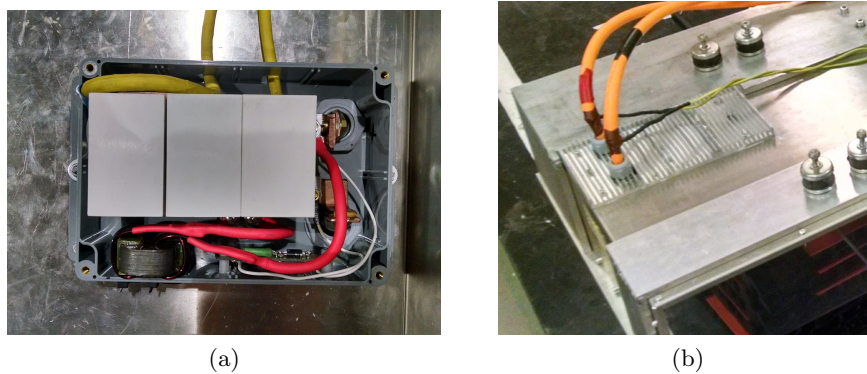
Figure 6.18: Final structure of the AC/DC converter with filters and protection circuit placed into the receiver structure (a). Detail of the AC/DC heat sink welded to the shield structure (b).

a resistance of 128 mΩ have been measured.

The measurements on the transmitter have been provided over 46 different transmitters realised for the construction of the on-road system. These measurements have been used also to verify the variability of the adopted manufacturing process. As visible in Fig. 6.22 and Fig. 6.23 the measurements provide an average value of 281.4 μH with a standard deviation of 0.97 μH which indicates a really good precision and repeatability of the manufacturing process. The same measurements have provided an average value of the resistance equal to 359.3 mΩ with a standard deviation of 20.2 mΩ. The value of the mutual inductance has been extracted through the evaluation of the total impedance, as ratio between transmitter voltage and current, by using the indications provided by an 8 bit Lecroy WaveSurfer 3000 digital oscilloscope and supplying the system with the developed power electronics. A simple resistive
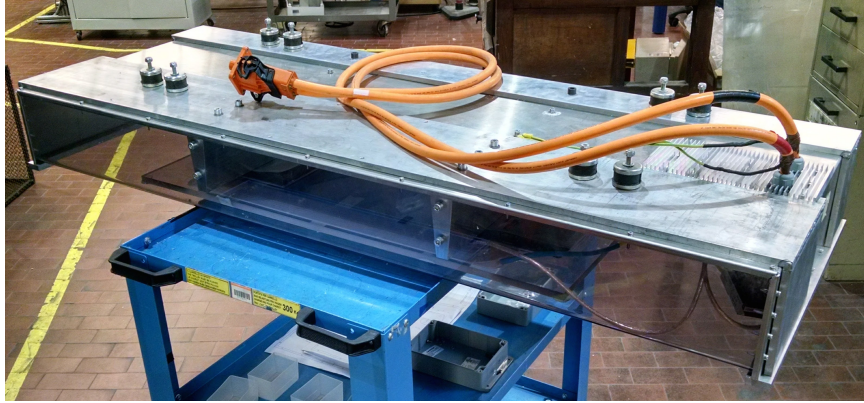
Figure 6.19: Complete receiver structure ready to be mounted under the vehicle.

Figure 6.20: Receiver structure mounted under the vehicle.
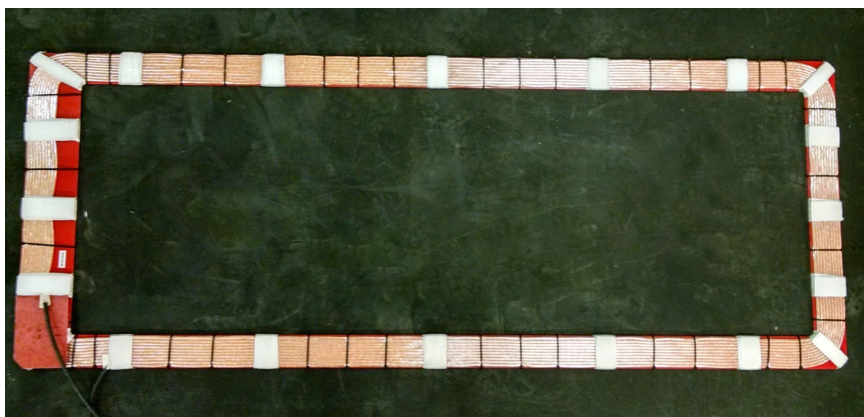
Figure 6.21: Transmitter coil fixed over the fiberglass base with the white tissue tape and the black plastic bands.

load of 4.5 Ω has been connected at the diode bridge output. A value of M equal to
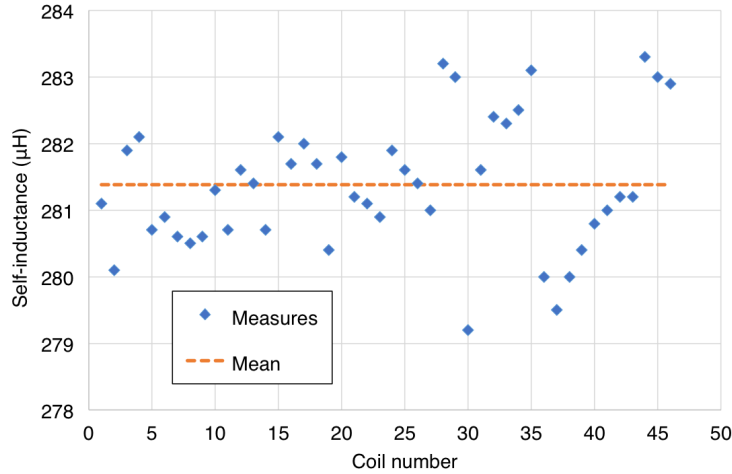
Figure 6.22: Measurements of self-inductance over 46 transmitters. Single measurements in light blue and average in orange.

14.9 μH has been estimated using the complete expression of the total impedance:

$$Z_{\mathrm{T}} = \frac{\hat{V}_1}{\hat{I}_1} = R_1 + j\left(\omega L_1 - \frac{1}{\omega C_1}\right) + \frac{\omega^2 M^2}{\left(R_2 + R_{\mathrm{L}} + j\left(\omega L_2 - \frac{1}{\omega C_2}\right)\right)} \qquad (6.16)$$

where R_1 is the sum of the resistances of coil and capacitors on the transmitter side (0.92 Ω) while R_2 represents the sum of the contribution of coil and capacitor resistance plus the resistances of the two diodes of the bridge in conduction at each semi-period (0.53 Ω).

The derived values from the tests are collected in Table 6.10 together with the relative errors with respect to the values derived from the simulations. The results show that the developed models result in a really precise estimation of the final values of the magnetic structure. It is worth noting that the higher relative error in the estimation of the mutual inductance has to be related also to the test conditions. In fact, as visible also in Fig. 6.24, the real shape of the voltage is not perfectly square introducing errors in the estimation of the amplitude of the first harmonic. Another source of error derives from estimation of the phase relation between the voltage V_1 and the current I_1 by means of the oscilloscope according to the typical problems of synchronisations of the channels at which the probes are connected.

Table 6.10: Values of self and mutual inductances from measurements and simulation.

Parameter	Value		Relative error
	Measured	Simulated	
Transmitter self-inductance (average)	281.4 μH	279.5 μH	0.67%
Receiver self-inductance	119.8 μH	120.8 μH	0.83%
Mutual inductance	14.9 μH	14.3 μH	4.3%
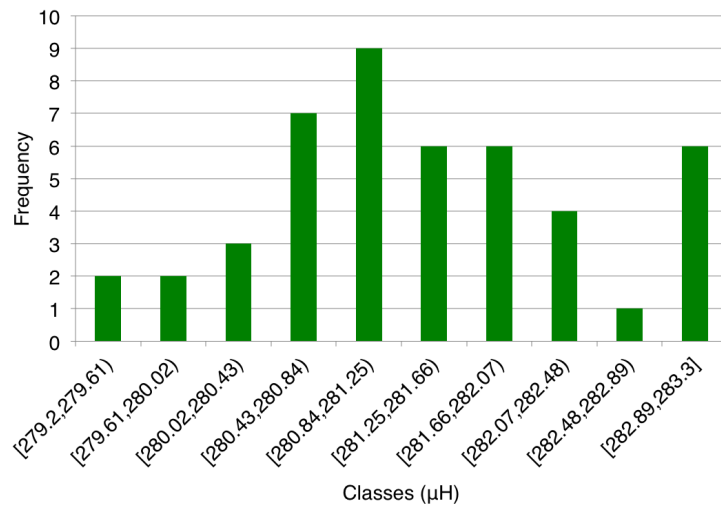
Figure 6.23: Frequency distribution of the measurements of the self-inductance of 46 transmitters.
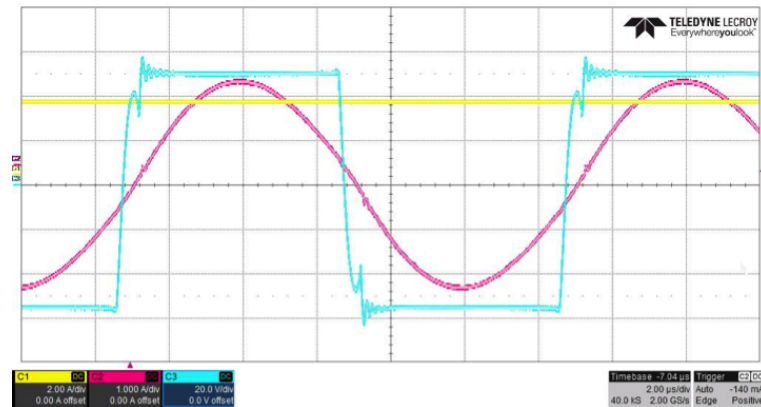
Figure 6.24: Wave form in case of supplying voltage (light blue) with duty cycle 50%. Transmitter current in purple and rectified current of the load resistor in yellow. The not perfect square shape of the voltage is visible.

6.8 Conclusions

The last two chapters presented the complete development of the two main components of the IPT system: the power electronics and the magnetic structure. Starting from qualitative observations based on the know-how of the designers and the study of the characteristics and constraints of the applications together at the future environment of application the design has been conducted introducing novelties on both fields. The AC/DC converter presents good characteristics in terms of switching capabilities in not perfectly resonant conditions preserving an efficiency higher than 98%. Its dimensions and costs make it perfectly suited for the proposed on-road installation described in the next chapter. A procedure for the design has been developed and applied to the creation of the dedicated magnetic structure. The design has used techniques of

optimisation, the development of precise electromagnetic models and the application of useful formulations of the magnetic problem. In addition, novel laboratory setups have been developed for the testing of the solutions without demanding the availability of a source at the nominal power with a real improvement in the testing time and in safety of the operations. The developed techniques and methodologies can be generically applied to the development of future solutions dedicated to the IPT.

Chapter 7

On road installation

The integration of the developed system in the road infrastructure represents a relevant outcome in the perspective of a future diffusion of the IPT technology. The investigations concerning this aspect has demanded relevant efforts and the synergy between different competences. The activities have been carried out in a dedicated test site with the final goal of the creation of a dedicated charging lane. The realisation of the test site has demanded the creation of a dedicated electric infrastructure for the supply of the IPT system and the powering of the auxiliary devices. These activities have been conducted within the two european projects eCo-FEV and FABRIC that involved also several aspects related to the creation of an electric mobility platform for the integration of electric vehicles into a cooperative infrastructure systems. In this chapter the two main aspects of the electric infrastructure and the methods for the integration in the road infrastructure are presented.

7.1 Test site and electrical infrastructure

The test site has been developed in Val di Susa at the foot of the Alps close to the city of Turin, thanks to the cooperation with Tecnositaf, owner of the site and partner of both projects eCo-FEV and FABRIC. The main concept of the implemented system is depicted in Fig. 7.1. It consists of a series of 50 transmitters placed with an interspace of 50 cm. Each coil is supplied by a dedicated DC/AC converter. This solution allows a more flexible management of the recharge and a stronger fault tolerance. The series of DC/AC converters is supplied through a DC distribution line that constitutes the DC bus of the overall system. The entire system is powered though an active AC/DC three-phase converter that provides a stabilised voltage at 630 V. The nominal power of the AC/DC converter, equal to 50 kW, allows to test the condition of two vehicles moving over the charging lane and absorbing the rated power of 20 kW at the same time. The system is directly connected to the LV distribution network through an ungrounded insulation transformer that electrically separates the utility three-phase
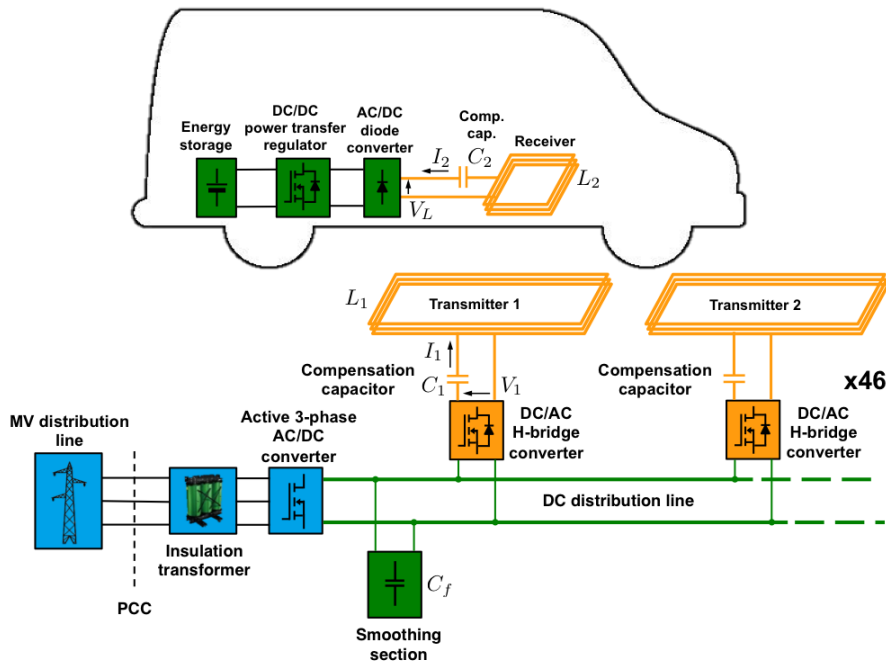
Figure 7.1: Scheme of the general architecture of the IPT system developed for the on road prototype.

distribution grid from the IPT system, allowing a dedicated IT system [134]. This solution guarantees the continuity of the power supply also after a first ground-fault without compromising the safety of the operators. The IT grounding system was chosen since the protection against indirect contact in TN systems[1] is challenged by the presence of active converters. In the case of ground-faults, in fact, converters positively reduce the fault current to nearly their nominal current, to protect their circuitry. This limitation of the current would prevent over-current protective devices from promptly tripping, exposing persons to the risk of electric shock.

The passage of the vehicle from one transmitter to the next one can generate an abrupt variation of the absorbed power, causing stress at the point of common coupling (PCC) with the utility network. This stress may cause degradation of the power quality due to possible voltage fluctuations related also to the injection of high order current harmonics. To mitigate this problem, the introduction of a capacitive smoothing made of super capacitors is proposed. The aim of the capacitors bank is to maintain a constant current at the output of the AC/DC converter thereby reducing the harmonic content at the PCC. The value of the capacitance has been fixed at 2.6 F according to the analysis presented in [135].

The AC/DC converter and the transformer have been placed in a dedicated building that has been named *power room*. As visible in Fig. 7.2, the DC distribution line

---

[1]Systems in which the neutral point of the power supply system is grounded, and enclosures of equipment are connected by a protective conductor to the main grounding bus of the installation, which is connected to the grounded point of the power supply.

comes out from the power room following a path at 50 cm under the ground together with an auxiliary AC distribution at the standard level of 230 V 50 Hz. This auxiliary distribution line reaches a shelter were the devices for the monitoring of the charging lane are placed.

The most important component placed in the shelter is a Single Board Reconfigurable I/O (sbRIO-9606 by National Instruments). The sbRIO manages the finite state machine that governs the different steps of the recharge interacting with the other components installed in the test site that form the IT infrastructure. This kind of reconfigurable devices were successfully adopted in several engineering applications [136–138]. In this case, it has been selected according to its high computing power provided by a 400 MHz industrial processor and a Xilinx Spartan-6 LX45 FPGA and the presence of several interfaces as DIO channels, CAN interface, serial RS232 interface, USB ports and a built-in Ethernet port. A complete description of the state machine and the other components of the IT infrastructure has been provided in the co-authored work [40].

The DC/AC converters are installed in dedicated manholes on the side of the road.
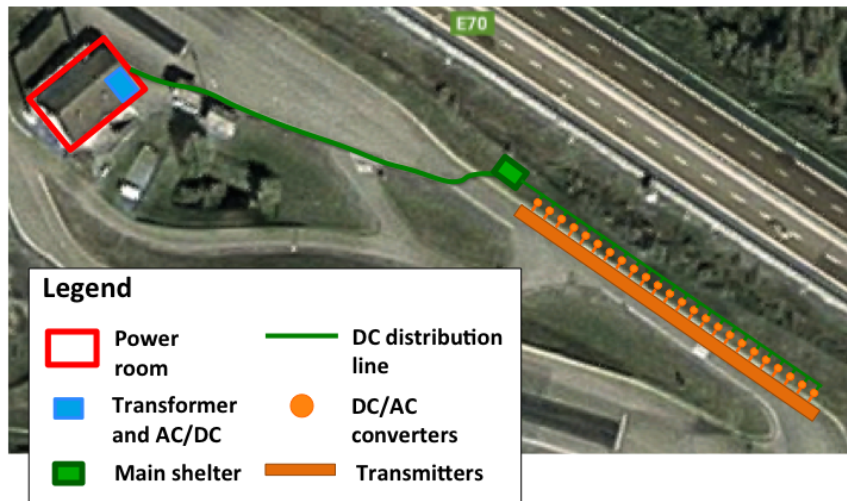
Figure 7.2: Map of the developed test site for the testing of the dynamic IPT infrastructure.

7.2 Coil embedding

The selection of a proper procedure for embedding the coils in the road pavement has faced significant technical issues. Unexpected phenomena have appeared during the first practical trial of embedding. Their comprehension and the identification of a feasible solution has demanded several weeks of work.

The first trial of embedding has been done directly on the test site with a transmitter having inner dimensions 1.25 m × 0.5 m made of 9 turns of litz wire with a diameter

of 4 mm. Its values of resistance and self-inductance (in the following simply indicated as R and L) have been preliminarily measured at the frequency of 85 kHz with an HIOKI 3532-50 LCR HiTESTER. The obtained values have been $R = 303$ mΩ and $L = 211.8$ μH. The coil has been embedded in a basement of not reinforced concrete (i.e. concrete without any reinforcing bars) following the procedure shown in Fig. 7.3. The coil has been covered with a layer of 2 cm of concrete and another layer of 3 cm of cold asphalt.

A new set of measurements has been carried out after the complete drying of concrete and asphalt. The measurements have been conducted powering the LCR meter by means of an insulation transformer in order to minimise the capacitive coupling between the instrument and the ground. The measurement has been automatised through a serial interface with a PC that has registered the acquired data. The instrument operates supplying the object under test with a sinusoidal voltage and calculating the amplitude and the phase of the impedance of the object by measuring the injected current. The instrument has been firstly calibrated on the whole frequency span through the open and short circuiting of the instrument terminals. The measurements have been carried out in the frequency range from 5 to 150 kHz. The resulting behaviour of the coil impedance is shown in Fig. 7.4. Contrary to what was expected, the behaviour of the impedance of the embedded transmitter was far from an inductive behaviour. As shown in Fig. 7.4a and Fig. 7.4b, the amplitude of the impedance is not linear with the frequency and the phase starts to be much lower than 90° above 60 kHz. The interpretation of the measurements with a series R-L model has provided a value of resistance and self-inductance equal to 14.7 Ω and 293 μH respectively. This discrepancy has been ascribed to the presence of capacitive coupling between the coil and the ground. The presence of this capacitive component can explain also the deviation from a linear behaviour of the impedance.

Starting from this hypothesis, a second check has been performed in order to assure the correctness of the results provided by the LCR meter. This second test has been carried out supplying the system through a power source and measuring the quantities of interest with a Teledyne LeCroy Wavesurfer 3024 digital oscilloscope. The test setup is shown in Fig. 7.5. It is composed by a 60 W linear power amplifier able to supply up to 2 A rms at 30 V rms. The input signal of the amplifier is provided by a signal generator. An 8.25 Ω low-inductance power resistor has been placed in series to the amplifier output in order to limit the output current. The role of the resistor is to protect the amplifier against a sharp increase of the current in case of presence of phenomena of series resonance in the load (the transimitter under test).

A sinusoidal voltage with a peak of about 18 V and a frequency of 88 kHz has been applied to the coil. The related waveforms are shown in Fig. 7.6. A phase difference $\phi = 83.9°$ between current and voltage has been measured and the ratio between the peaks of the two waveforms revealed an impedance amplitude Z_{RL} of about 180 Ω.

(a) (b)

(c)

(d) (e)
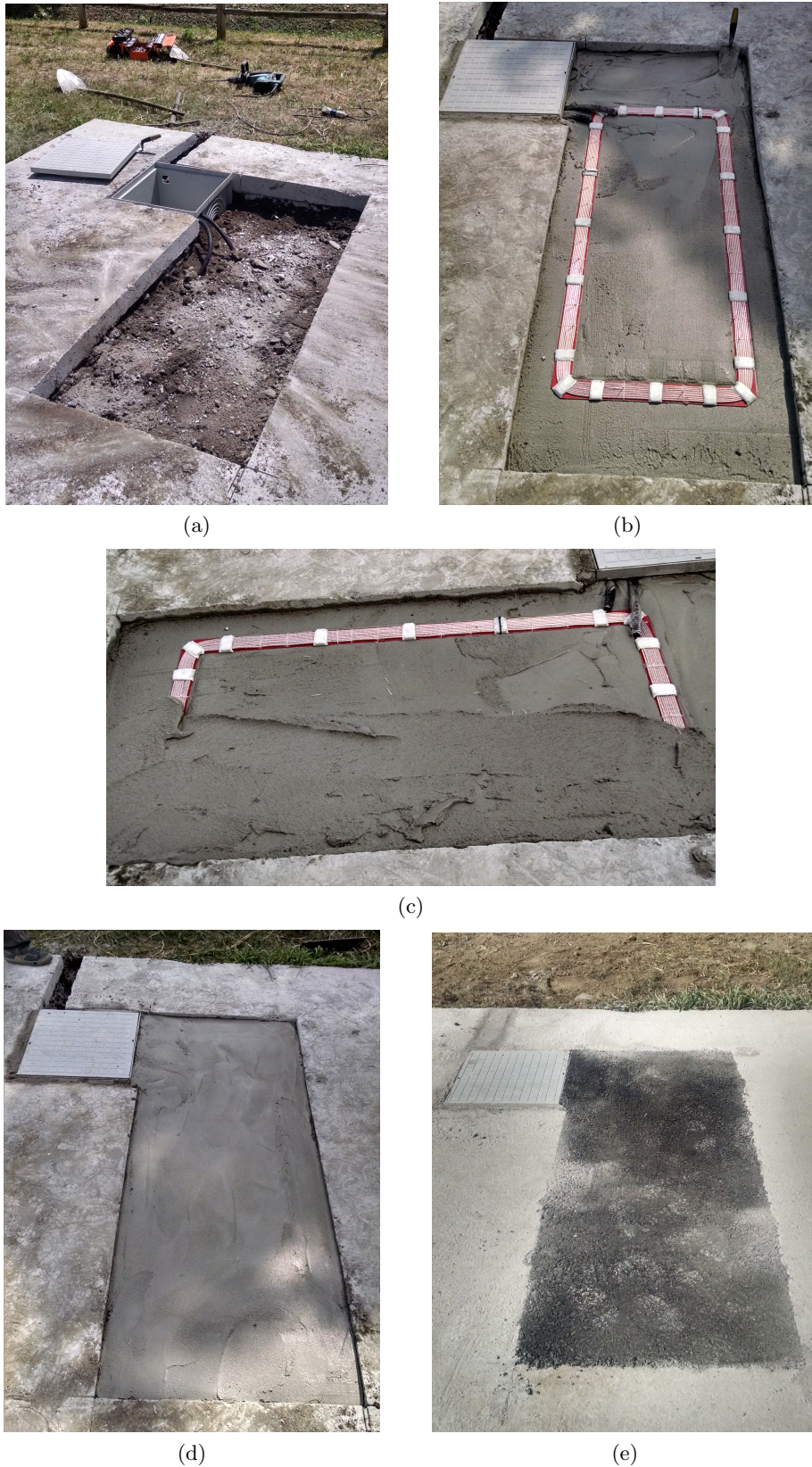
Figure 7.3: First try of embedding procedure. Realisation of the hole for the coil placement (a). Creation of a first layer of concrete for the placement (b). Coil placed on the semi-wet concrete layer (c). Coil embedding with a layer of 2 cm of concrete (d). Completed embedding under concrete (e). Final layer of cold asphalt (f).
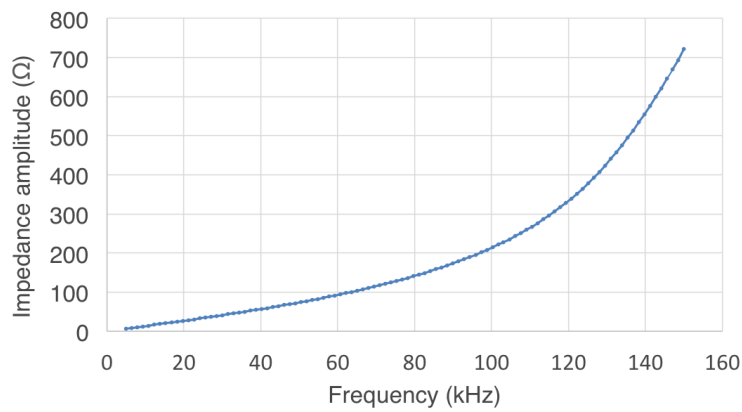
(a)
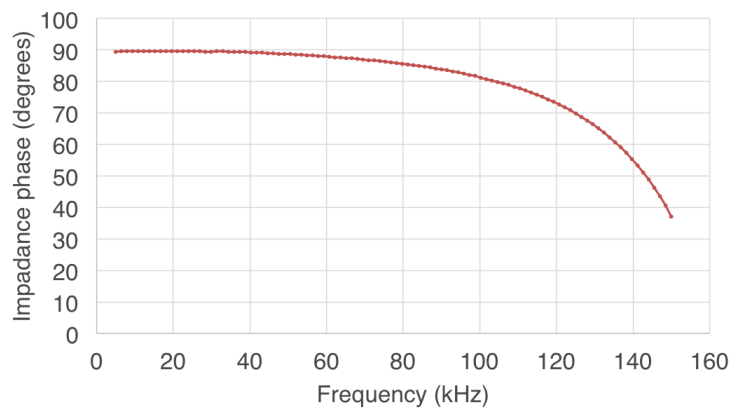
(b)

Figure 7.4: Amplitude (a) and phase (b) of the coil impedance in the frequency range $5-150$ kHz.
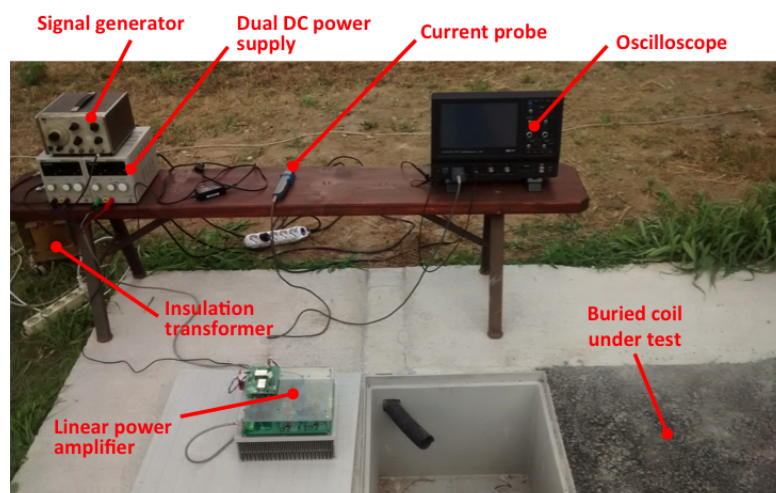
Figure 7.5: Test setup with power linear amplifier.
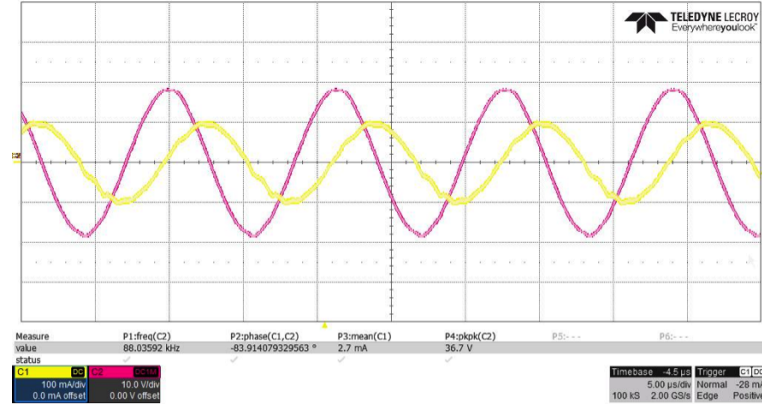
Figure 7.6: Waveforms of the voltage (magenta) 10 V/div and current (yellow) 100 mA/div at the output of the linear power amplifier. Time axis 5 μs/div.

(a)

(b)
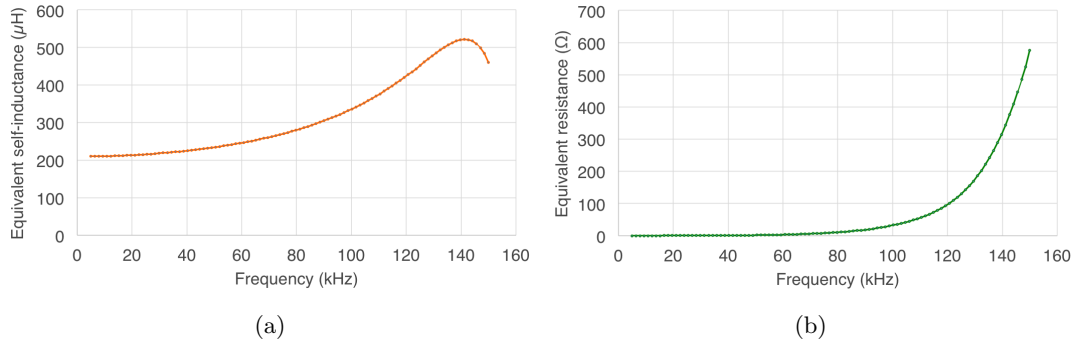
Figure 7.7: Values of self-inductance (a) and series resistance (b) calculated by the LCR meter.

The match of these results with the R-L series model through the equation set (7.1), has provided an estimation of $R = 19.1 \ \Omega$ and $L = 323.7 \ \mu$H.

$$\begin{cases} Z_{RL} = \sqrt{R^2 + (\omega L)^2} \\[2mm] \tan\phi = \dfrac{\omega L}{R} \end{cases} \tag{7.1}$$

The value of the additional resistance has been subtracted to the value of R obtaining a value of 10.85 Ω. These results are consistent with the measurements done with the LCR meter that indicate a value of $R = 17.2 \ \Omega$ and $L = 301 \ \mu$H as shown in Fig. 7.7.

This test confirmed the reliability of the measurements carried out by means of the LCR meter clearly indicating that the embedding process introduced additional phenomena that modified the behaviour of the coil moving it away from the inductive behaviour.
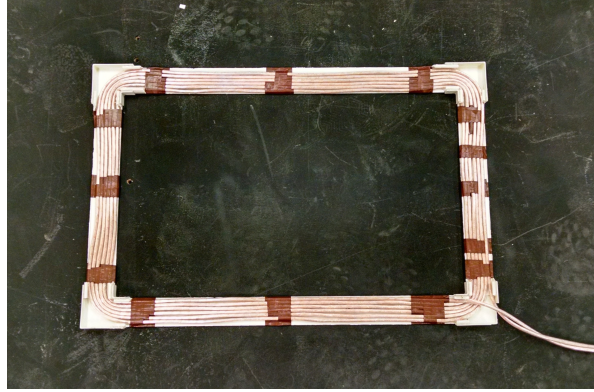
Figure 7.8: Coil for the laboratory tests.

7.2.1   Tests on laboratory

A series of laboratory experiments have been conducted in order to better understand the physical mechanisms that caused the underligned phenomena and put them in correlation with the embedding process. Two coils of reduced dimensions 30 cm × 40 cm, as the one depicted in Fig. 7.8, have been assembled using 6 turns of litz wire with a diameter of 4 mm. Both coils have been placed into a plastic wire way that helped to form and to maintain them in the right position. The two identical coils have been named A and B. Two wooden containers $1 \times 1.2 \times 0.15$ m^3, as the one shown in Fig. 7.9, have been built for the tests. The impedances of both coils have been preliminarily measured placing them in the container. The container has been sustained by a wooden base with a height of 40 cm. This arrangement has assured a sufficient distance from possible metallic objects. The results indicate a linear behaviour of the impedance (inductive behaviour) until 1 MHz. At this impedance corresponded a value of self-inductance equal to 45 μH.

After these preliminary measurements, the coil A has been placed over a layer of 5 cm of semi-wet concrete and covered with another layer of the same thickness as illustrated in Fig. 7.10. New measurements have been conducted after 48 hours with the concrete completely dry. A more extended frequency range has been chosen according to the small dimensions of the coil and the small value of self-inductance. This last assumption can be explained assuming that, in first approximation, the electric coupling with the concrete (capacitance of the coil with respect to the concrete) is in some way proportional to the surface of the coil. The smaller the exposed surface the smaller the capacitance. Smaller values of inductance and capacitance mean a shift toward higher frequencies of eventual phenomena of resonance. The results shown in Fig. 7.11 have clearly confirmed the hypothesis of the capacitive coupling with the ground. In fact, the behaviour shown in Fig. 7.11 is equivalent to a parallel RLC circuit. The amplitude reaches its maximum at about 1 MHz and in correspondence of this frequency the phase becomes zero. The results clearly indicate an increase in
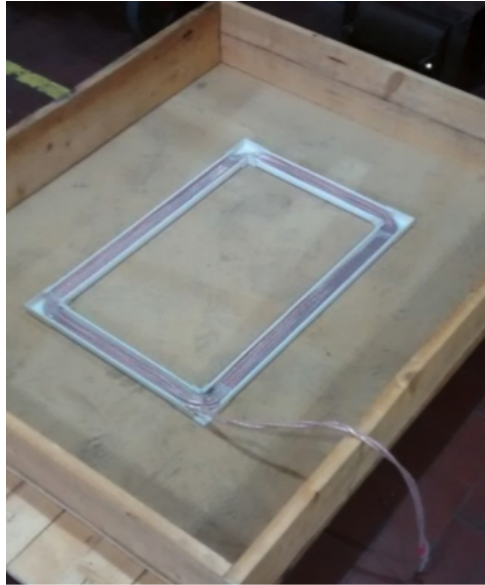
Figure 7.9: Wooden container for the housing of the coil and the testing of the embedding conditions.
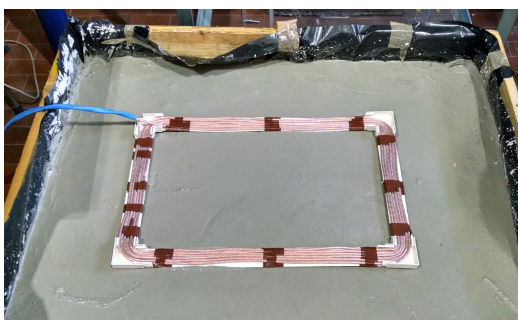
(a)   (b)

Figure 7.10: First test using coil A placed over a layer of concrete (a) and completely covered by a second layer (b).
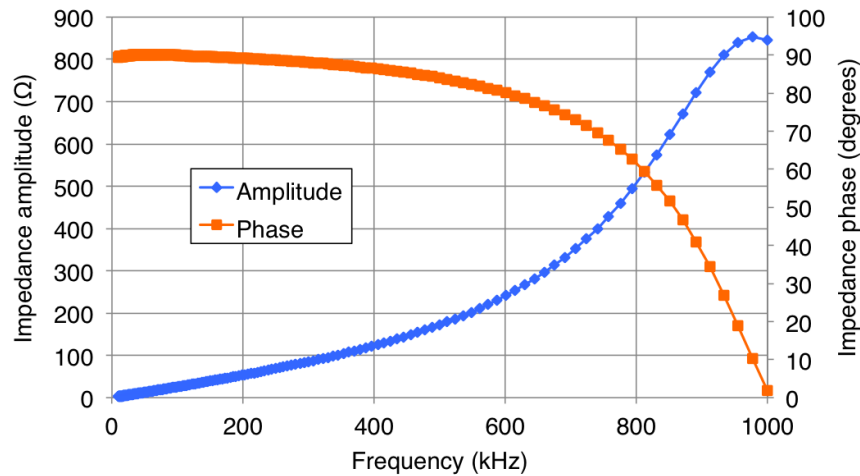
Figure 7.11: Amplitude and phase of the impedance of coil A buried into concrete.

Figure 7.12: Last layer of cold asphalt for the tests on coil A.

the impedance and a strong modification of the phase as pointed out in the first test of embedding. A layer of 3 cm of cold asphalt has been superposed to the concrete in order to reproduce the embedding process used for the first try (Fig. 7.12). The measurements have been repeated. The results shown in Fig. 7.13 indicate that the cold asphalt does not affect the behaviour of the coil.

According to what emerged from the tests on coil A, coil B has been used to investigate a possible solution. The main idea behind the proposed solution has considered the capacitance between the coil and the ground as inversely proportional to their distance similarly to a planar capacitor. Hence, a non conductive material acting as dielectric has been placed between the coil and the surrounding material. The increase of the distance aimed at the reduction of the capacitance toward the ground moving the phenomena of resonance at higher frequencies far from the working frequency.

The idea has been implemented by filling the plastic wire way with a bituminous coating obtaining a layer of about 5 mm all around the coil. The resulting object is shown in Fig. 7.14. The same embedding steps with the two layers of concrete (5 cm under and 5 cm above the coil) and the layer of cold asphalt (3 cm) have been
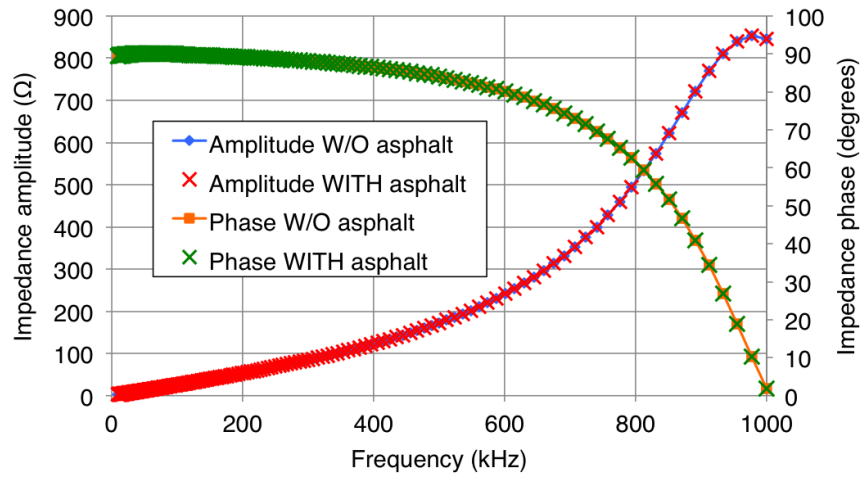
Figure 7.13: Comparison of amplitude and phase measurements of the impedance of coil A buried into concrete and coil A buried into concrete with the addiction of a layer of cold asphalt.

Figure 7.14: Coil B with the plastic wire way filled with bituminous coating.
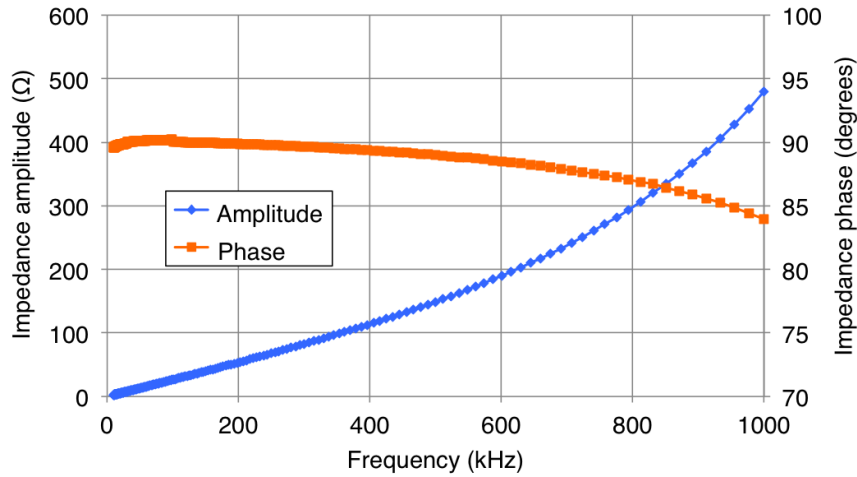
Figure 7.15: Impedance measurements on coil B embedded with the bitumen preliminary layer.

Table 7.1: Parameters of the coils for the embedding tests on the test site.

Coil name	Inner dimensions	Num. of turns	Wire diameter
L_1	0.5×1.5 m	9	4 mm
L_2	0.5×1.5 m	9	4 mm
L_3	0.5×1.5 m	10	5.5 mm
L_4	0.5×1.5 m	9	4 mm
L_5	0.5×1.5 m	10	5.5 mm
L_6	0.5×1.5 m	9	4 mm

applied to the coil B. Finally, the impedance measurement has been repeated. The results shown in Fig. 7.15 indicate the success of the adopted process. As expected, the non linear behaviour of the impedance becomes evident only above 300 kHz. At the frequency of 1 MHz the phase is equal to about 85° instead of the 0° presented in absence of the layer of bitumen (Fig. 7.11).

On the base of this result a new series of tests have been conducted on the test site investigating different materials and embedding processes.

7.2.2   Tests on the real environment

Six different coils labeled as L_1, ..., L_6 have been built to be tested directly in the test site. Each coil has been buried following a different procedure or using different materials. The wire diameter, the number of turns and the dimensions slightly differs from the final design of Section 6 as the coils have been built using the available materials. The characteristics of each coil are reported in Table 7.1.

The second goal of the tests has been the individuation of a fast and cheap way to integrate the transmitters into the road pavement on the base of the knowledge of the POLITO group and Tecnositaf as expert in the field of road infrastructures. Each
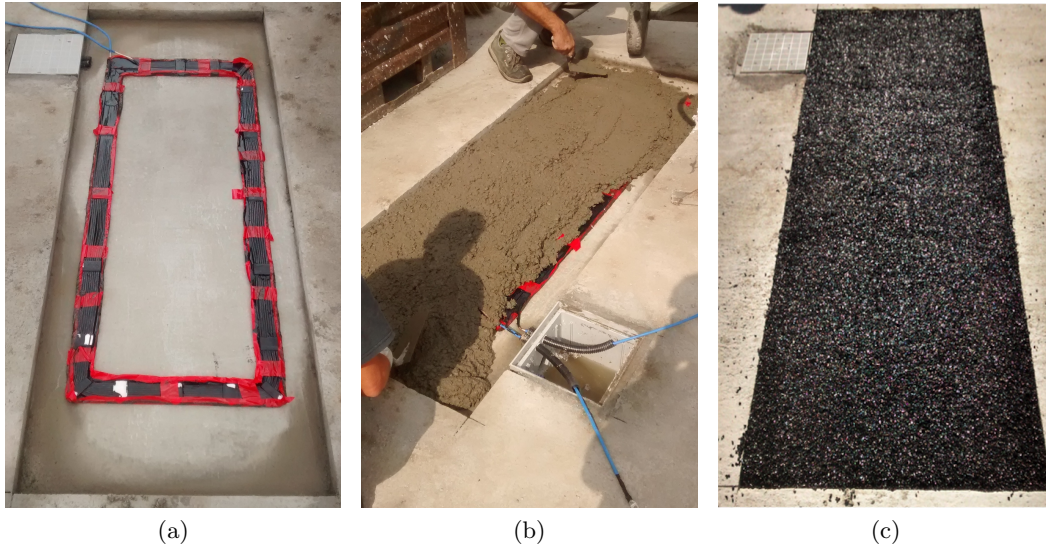
Figure 7.16: Embedding procedure on coil L_1. Placement of the coil with dry layer of bituminous coating (a). Cover with the layer of concrete (b). Final layer of cold asphalt (c).

test is described in the following.

Coil L_1

Coil L_1 has been used to test the same bituminous coating used for the laboratory test on coil B. It has been placed in a dedicated concrete housing and covered with a layer of 2 cm of concrete and another layer of 3 cm of cold asphalt. The process is illustrated in Fig. 7.16. At each step the impedance of the coil has been measured and the results are shown in Fig. 7.17.

Fig. 7.17a confirms that the bituminous coating does not influence the behaviour of the coil that remains perfectly inductive. Some modification occurs after the burying under the concrete layer (Fig. 7.17b) but the impedance remains perfectly inductive at the frequency of interest of 85 kHz. The strict similarity between Fig. 7.17b and Fig. 7.19c confirms that the cold asphalt does not create any kind of problem.

This first process has been considered suitable for the coil embedding. Moreover the bituminous coating is a low cost readily available material. Nevertheless, the use of concrete for the creation of the housing was strongly time consuming and expensive in terms of cost of material and cost of human work.

It is worth nothing that, for certain values of frequency, the values of the phase appear slightly higher than 90°. This is an intrinsic error due to delays in the acquisition chain of the instrument [139].

Coil L_2

Coil L_2 has been embedded with the same method of coil L_1 but substituting the bituminous coating with an epoxy resin typically adopted for the realisation of high

Figure 7.17: Impedance measurements on the coil L_1 during the different phases of the embedding process. Preliminary measurements after the application of the bituminous coating (a). After the laying of the concrete layer (b). Final measurement with the cover of cold asphalt (c).

frequency transformers and inductors. The resin needs several hours to become completely dry resulting in a rigid and compact object as visible in Fig. 7.18. The measurements referred to each step are shown in Fig. 7.19. Also this second process has resulted feasible together with the proposed dielectric material. The only relevant cons of this process is represented by the higher cost of the resin that is a high-tech material dedicated to a specific manufacturing process.

Coil L_3

A different embedding method avoiding the creation of a concrete housing has been used for the other coils. Coils L_3 and L_4 have been placed in a template hole directly cut on the road pavement (standard asphalt). For L_3, an elastomeric liquid bitumen, cheaper than the bituminous coating, has been used as dielectric. The coil has been placed directly into the hole that has been filled with the liquid elastomeric bitumen. The main steps of the embedding process are illustrated in Fig. 7.20. The embedding process has not been completed with the last covering layer as the liquid elastomeric bitumen turned out not to be suited for the application. As pointed out in Fig. 7.21, the coil has presented a clear phenomenon of resonance around 85 kHz meaning that the adopted material did not provide the expected effect. Hence, the liquid elastomeric bitumen has been excluded among the usable materials for the coil embedding.

Figure 7.18: Coil L_2 inserted in the epoxy resin block placed on the concrete housing.

(a)

(b)

(c)

Figure 7.19: Impedance measurements on the coil L_2 during the different phases of the embedding process. Preliminary measurements after the application of the epoxy resin (a). After the laying of the concrete layer (b). Final measurement with the cover of cold asphalt (c).

(a)
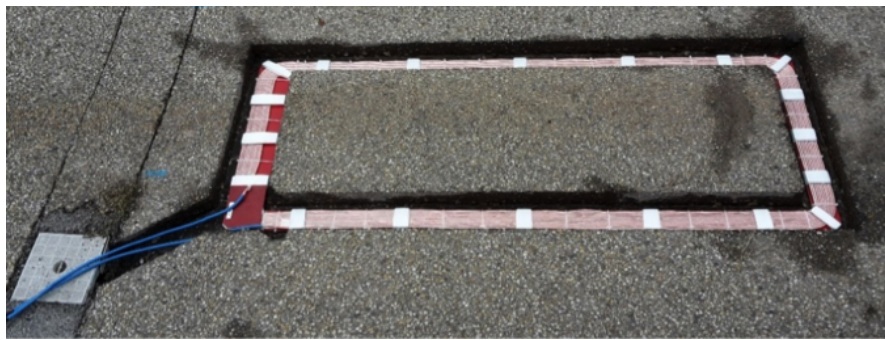
(b)

(c)

(d)

Figure 7.20: Embedding process of coil L_3. Template hole cut in the asphalt (a). Coil placed in the hole (b). Partial filling with liquid elastomeric bitumen (c) with a detail on the hole depth in the upper part. Coil completely covered by the liquid elastomeric bitumen (d).
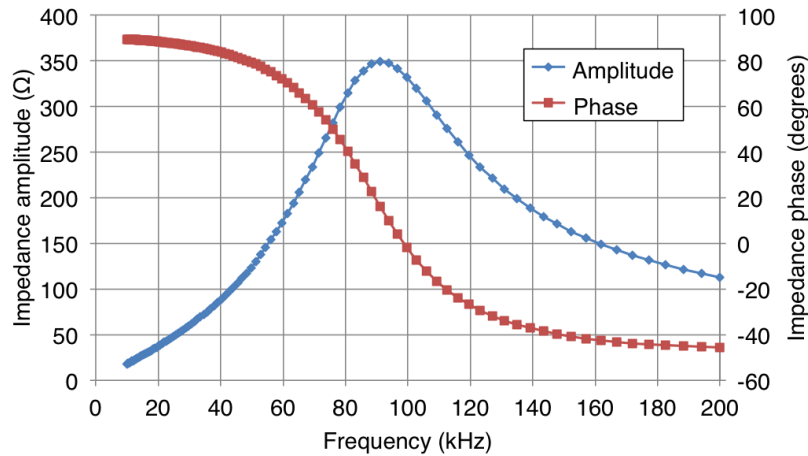
Figure 7.21: Measurements of the impedance of coil L_3.
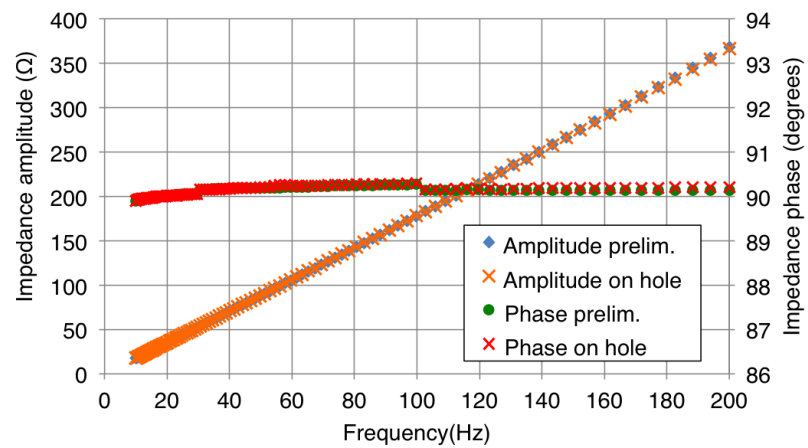
Figure 7.22: Comparison of the measurements on the impedance of coil L_4 for a preliminary case with the coil far from any external object and the same coil placed in the template hole.

Coil L_4

The first measurements on coil L_4 has been conducted by simply placing the coil in another template hole (as for L_3 in Fig. 7.20b). This test has been done in order to exclude the road asphalt as possible cause of the undesired effects pointed out on coil L_3. The comparison with the preliminary measurement in laboratory is shown in Fig. 7.22. The difference with respect to the preliminary measurements is completely negligible. This result confirmed the possibility to create the housing directly in the road asphalt. This method has been preferred because it was faster and cheaper than the previous one based on the concrete housing.

The coil L_4 has been then used to test, as dielectric, the bituminous emulsion MAPEI Plastimul. This material has been tested according to the absence of solvents in its composition. In fact, the presence of solvents has been considered one of the possible causes of the negative behaviour of the liquid elastomeric bitumen: the solvents evaporate during the drying process leaving porosities that can lower the dielectric
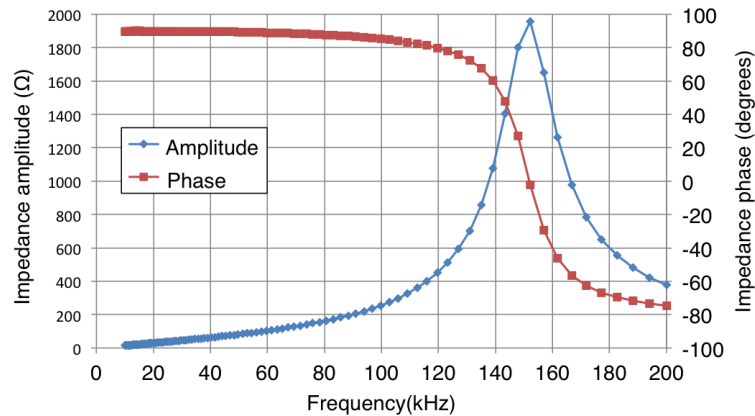
Figure 7.23: Measurements of impedance and phase of coil L_4 covered with a layer of Plastimul.
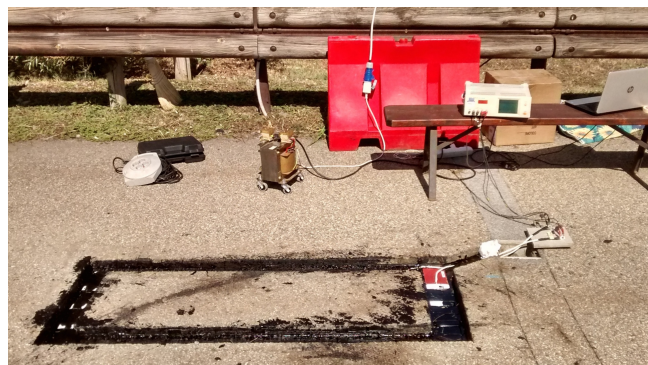
Figure 7.24: Test setup with coil L_5 placed in the hole and covered with liquid bituminous coating.

properties of the material.

This hypothesis has not been verified by the test. Fig. 7.23 shows the appearance of a resonance around 150 kHz that causes anyway a unacceptable modification of the behaviour of the coil.

Coil L_5

The test on the coil L_5 has been done by filling the hole with the same bituminous coating used for coil L_1 (Fig. 7.24). A cold asphalt has been used for the last layer of 3 cm. The results of the measurements are shown in Fig. 7.25 for each phase of the embedding process. At the end of the process, the amplitude presents a linear trend until 150 kHz. After this frequency the behaviour starts to slightly deviate from the linearity. The phase remains stable around 90° until 100 kHz. Above this frequency it start to decrease. The comparison with the preliminary laboratory measurements at the frequency of 85 kHz indicated an increase of the self-inductance of about the 2.7% and a negligible variation of the phase (measured phase = 89.96°). The adopted process is then considered feasible.
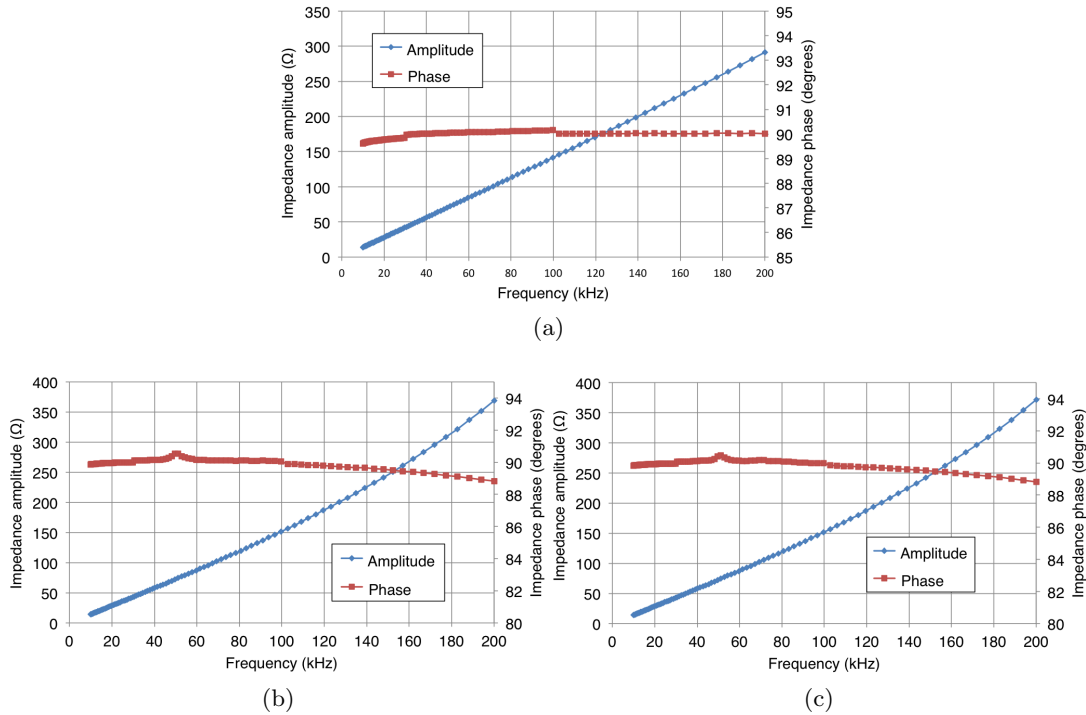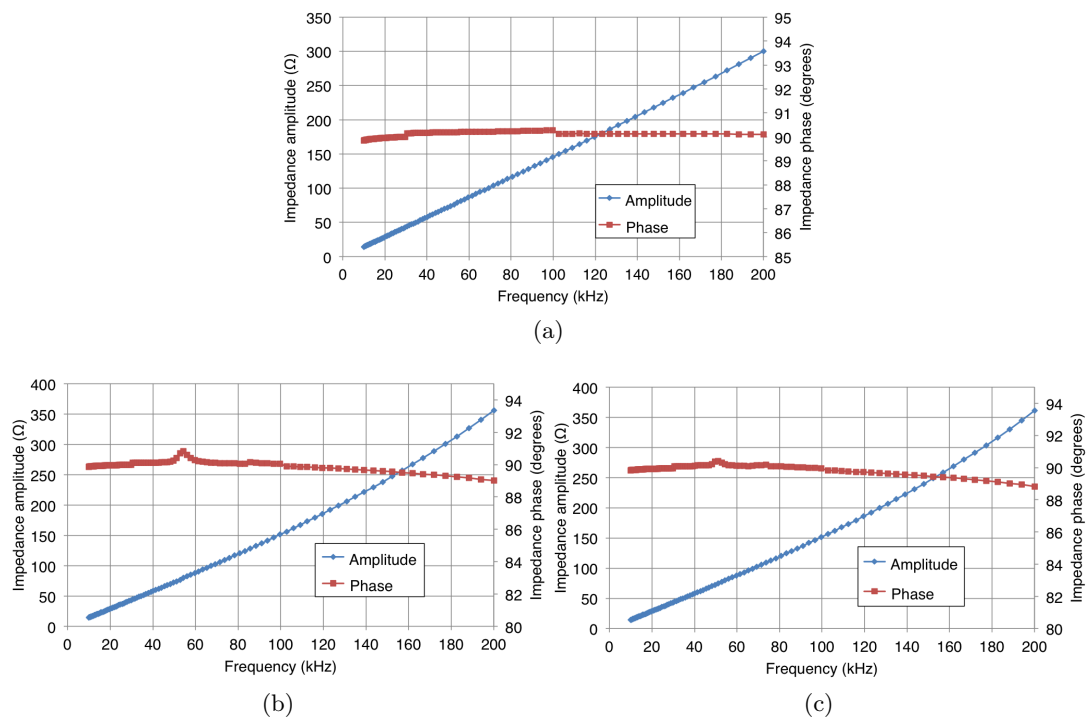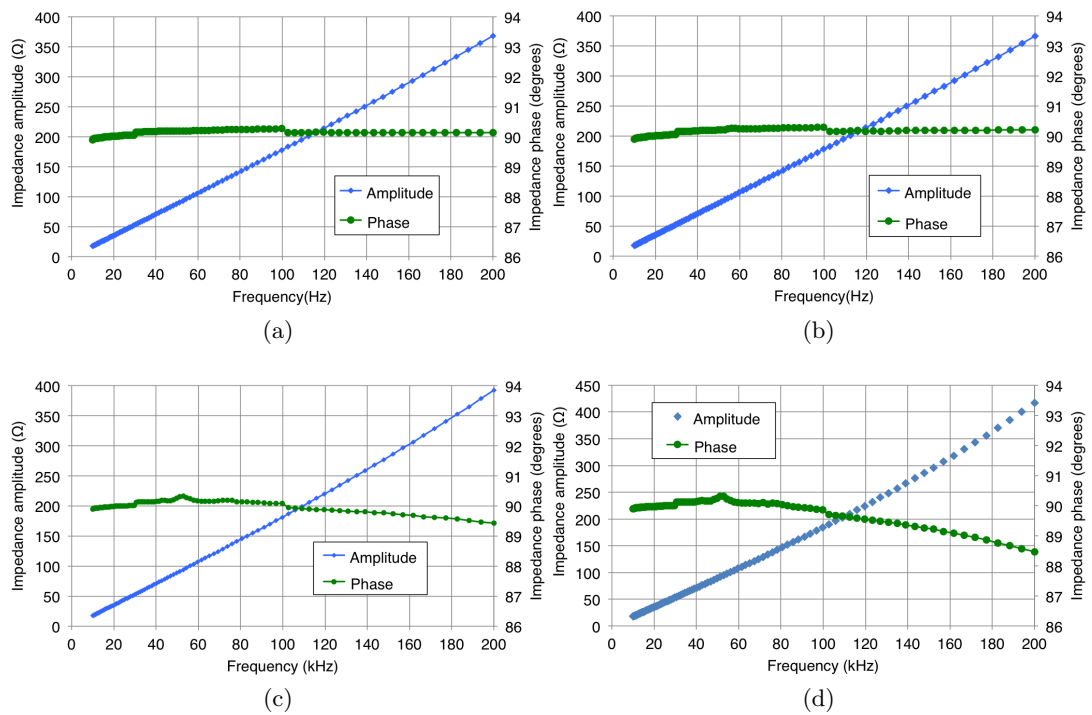
Figure 7.25: Impedance measurements on the coil L_5 during the different phases of the embedding process. Preliminary measurements in laboratory (a). After the laying in the asphalt hole (b). With the first layer of bituminous coating (c). Final measurement with the cover of cold asphalt (d).
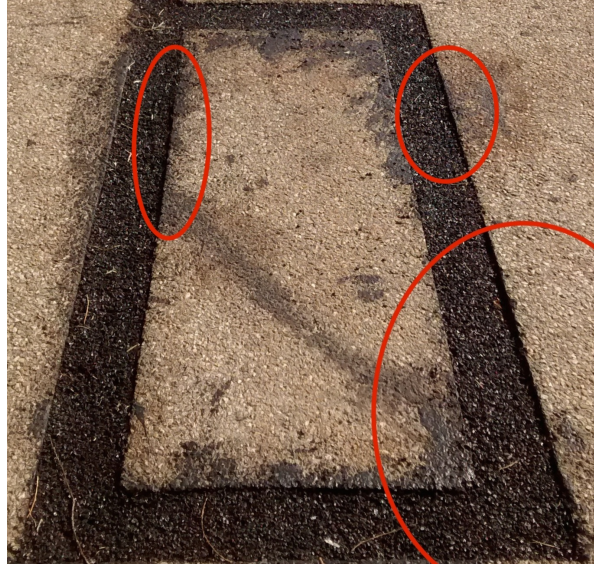
Figure 7.26: Deteriorated areas (red circles) on coil L_5.

(a)   (b)

Figure 7.27: Appearance of the hole filled with cold asphalt (a) and MAPEI Mapegrount (b).

Coil L_6

Despite the cold asphalt appeared to be well suited the necessities of the application, it presented problems in terms of mechanical resistance. The coils have been stressed by the passage of different light vehicles during one week of tests. After this week, the layers of cold asphalt has started to degrade as visible in Fig. 7.26. This inconvenience forced the investigation of an additional material for the creation of the pavement layer.

The MAPEI Mapegrount SV T has been considered among the possible materials for the ground pavement permitted by the standard regulations [36]. This material is a pre-blended mortar based mix with a consistence more compact than the cold asphalt as visible in Fig. 7.27. Even though this material presented better characteristics in terms of simplicity of laying, fast drying, grip and mechanical robustness, the measurements have pointed out an unacceptable effect on the coil impedance. The results are depicted in Fig. 7.28 and refer to a condition with the coil L_6 covered by a first layer of bituminous coating and a cover layer of MAPEI Mapegrount.
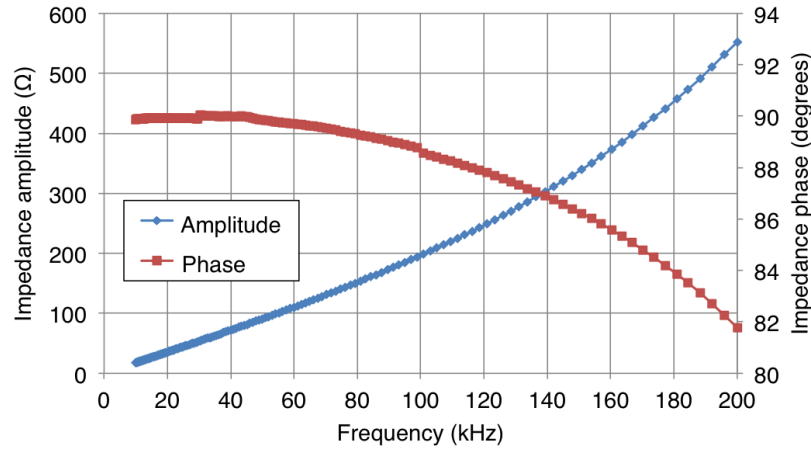
Figure 7.28: Measurements of impedance and phase of coil L_6 covered with bituminous coating and last layer of Mapegrount.

Table 7.2: Tested materials, use and suitability on the base of the test results (✓ suitable, × not suitable).

Material	Use	Test result
Concrete	Intermediate layer	✓
Cold asphalt	Pavement	✓
Bituminous coating	Separation coil-ground	✓
Epoxy resin	Separation coil-ground	✓
Elastomeric bitumen	Separation coil-ground	×
MAPEI Mapegrount	Pavement	×
MAPEI Plastimul	Separation coil-ground	×

7.3   Final charging lane integration

Table 7.2 summarises the results of the tests with respect to the analysed materials and methods of embedding. According to these results, a first section of 20 m of the charging lane has been created adopting the technique tested on the coil L_4 but using the concrete for the cover layer. Concrete has been the only material fitting the main requirements of low impact on the coil behaviour (in presence of adequate dielectric layer), simplicity of laying and mechanical robustness. It is worth mentioning that the characteristics of the concrete in terms of grip are not advisable for any kind of road pavement. In this first version the concrete has been treated in order to increase its roughness improving its characteristics in terms of grip guaranteeing safe conditions for the drivers during the tests. The final developed process for the integration of the transmitter on the road pavement is illustrated through Fig. 7.29. It starts by cutting the hole borders in the asphalt by means of an angle grinder and then digging the inner asphalt using a pneumatic drill. The bottom part of the hole is flatten with a hand press then the transmitter is placed at a depth of 5 cm under the pavement level. The hole is filled with bituminous coating until the transmitter is completely

<div align="center">(a)</div>

<div align="center">(b)</div>

<div align="center">(c)</div>

<div align="center">(d)</div>
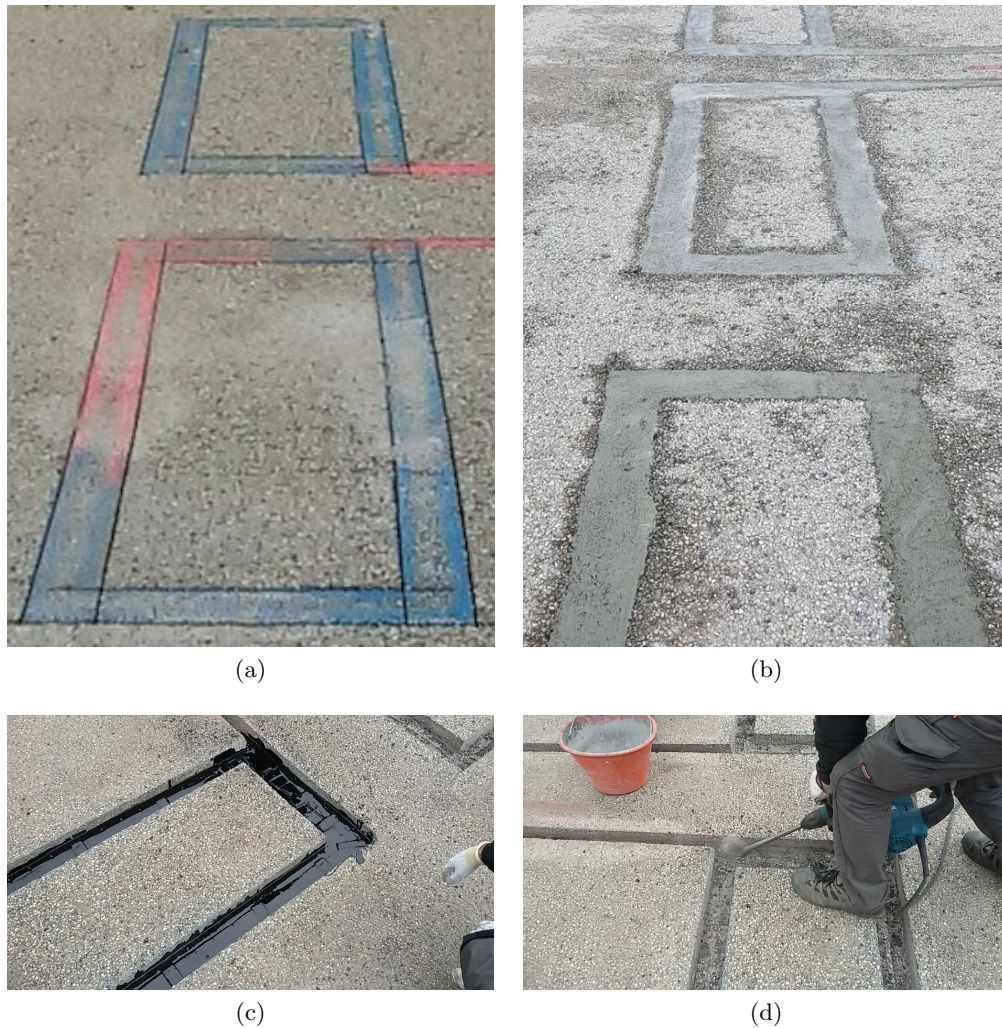
Figure 7.29: Description of the embedding process. Cut of the template hole borders (a). Digging of the hole in the road asphalt (d). Filling of the separation material between coil and ground (c). Last layer of concrete (b).

covered. When the bitumen is completely dry, a layer of about 3 cm of concrete is used to cover the hole reaching the pavement level.

The distance between the transmitters has been chosen by means of the models developed in Chapter 6. When a transmitter is active and supplied with the nominal current, the distance of 50 cm guarantees a coupling with the not active transmitters in the proximity that gives place to an open-circuit voltage lower than 30 V. This voltage does not create problems to the DC/AC converter and it is perfectly manageable during the start-up phase.

The connection between the transmitter, the DC/AC converter and the DC distribution is done as sketched in Fig. 7.30. The terminals of the coil reach a manhole placed at 2.2 m far from the transmitter. The two terminals are twisted together in order to limit the additional self-inductance introduced by the long connection. Each manhole receives the terminals of two consecutive transmitters then it houses
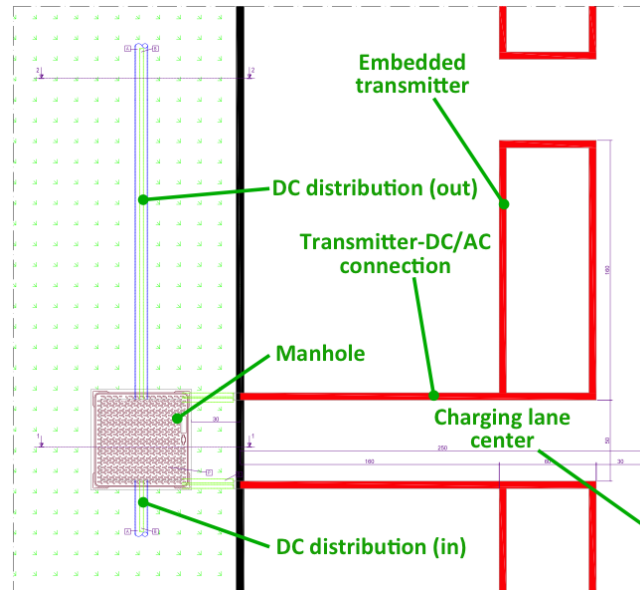
(a)

(b)

Figure 7.30: Plan of the placement of coils, manhole and connection with the DC distribution line (a) and realisation (b).

two DC/AC converter mounted on two sides of the same heat sink (Fig. 7.31). The manhole is also the point of connection between the DC distribution line and the converters through a parallel connection (in-out scheme [140]). The final appearance of the charging lane is shown in Fig. 7.32. The ensamble of two consecutive transmitters and the related components constitute the basic charging unit of the IPT system. According to the representation of Fig. 7.33, the charging unit is used as reference for the estimation of the costs of implementation of the charging lane that are summarised in Table 7.3. The results indicate a cost of about 558 €/m.

7.4 Conclusions

The present chapter has presented the different activities aimed at the creation of a dedicated infrastructure for the installation of the designed IPT system. The embedding of the transmitters in the road pavement has resulted the most critical and
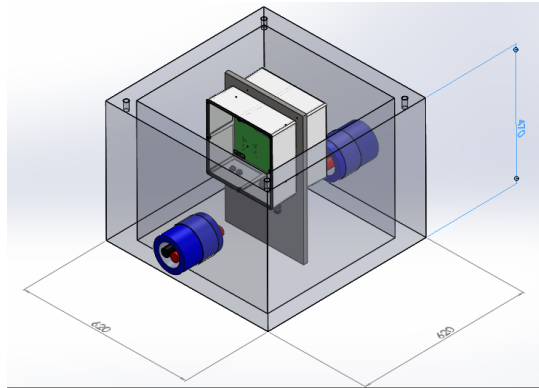
Figure 7.31: 3D model of the heat sink in the manhole with the mounting of the two DC/AC converters. In blue the connectors for the connection to the DC distribution and the transmitter.
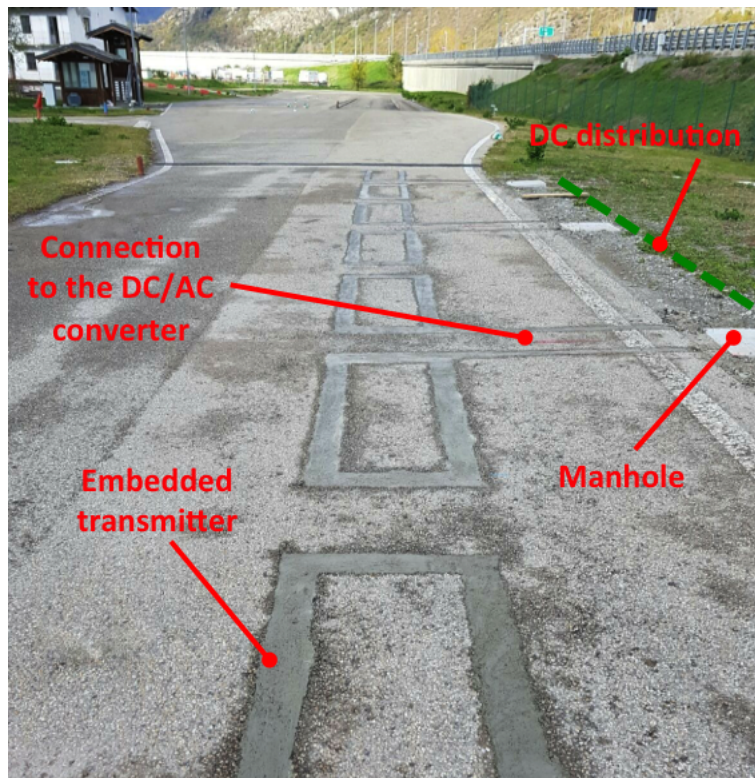
Figure 7.32: Final aspect of the charging lane installed in the road infrastructure.
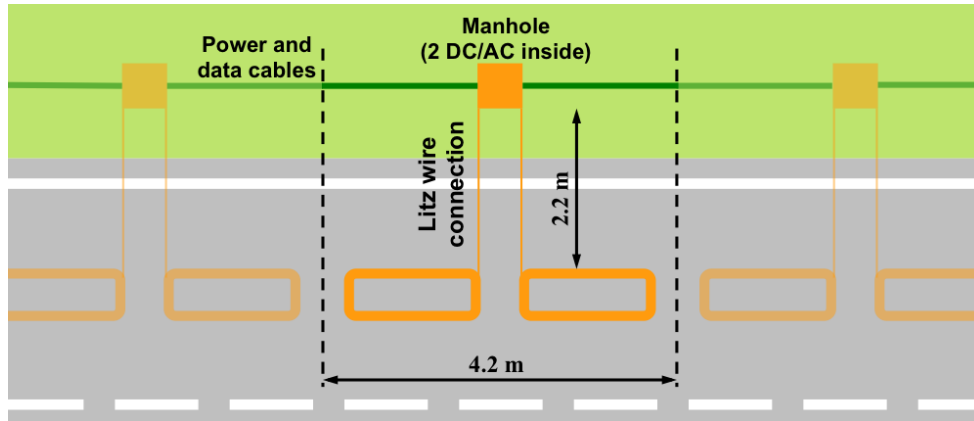
Figure 7.33: Scheme of a charging unit considered for the estimation of the cost per meter.

Table 7.3: Charging unit components and costs

Description	Quantity	Cost
DC cables	4.2 m	15.00 €
Data and auxiliary supply cables and pipes	4.2 m	8.00 €
Manhole	1	20.00 €
Power and data connectors	1	40.00 €
Transmitter and comp. capacitors	2	500.00 €
DC/AC converter	2	600.00 €
Materials for transmitter embedding	Lump sum	300.00 €
Manpower for DC line and manholes placing and manholes placing	Lump sum	320.00 €
Manpower for transmitters embedding	Lump sum	540.00 €
Total cost		**2343.00 €**

challenging issue. The carried out tests have demonstrated that the capacitive coupling of the coils with the ground can represent a bottleneck for the future integration of the IPT systems. This problem becomes strongly relevant for frequencies higher that 15-20 kHz. The interposition of a dielectric material between the coil and the ground has seemed an effective solution to mitigate the effect of the capacitive coupling on the equivalent behaviour of the coil. Nevertheless, the mechanisms that renders certain materials not suited is not clear and only some first rough hypothesis has been proposed in this work. The identification of suitable materials for the road pavements will surely represent a necessary step concerning the future integration in the road infrastructure.

Chapter 8

Human exposure assessment

The last chapter of the present thesis is dedicated to the relevant problem of the safety in relation to the protection of people from the electromagnetic fields involved in the IPT application. In the opinion of the author, this is a mandatory ethical duty that cannot be omitted in each process of development of a new technology. Moreover, the possibility to assure the compliance with existent standards related to the safety is an essential component for the social acceptance and the diffusion of a new commercial product.

The activities conducted in this field have resulted in the development of a methodology for the assessment of the IPT systems applicable to the dynamic case but also to vehicle parked (static IPT) or temporary stopped above the transmitter i.e. a particular condition of the dynamic IPT called stationary IPT). In the dynamic case, the different transmitters have to be sequentially energised for few milliseconds in correspondence to the passage of the vehicle giving rise to pulsed magnetic fields. Considering the system presented in this work, a vehicle speed of 40 km/h means a permanence over a transmitter (then the energisation of the transmitter) for an interval of about 135 ms.

The presented methodology has been directly applied on the developed IPT system.

8.1   Methodology for the exposure assessment

8.1.1   Pulsed magnetic field

The proposed methodology has been developed adopting the 2010 ICNIRP guidelines as reference for the assessment. These guidelines provides a definition of two different limits for the assessment. This standard distinguishes the *reference values*, i.e. values that can be directly measured like the magnetic flux density, and the *basic restrictions* that are based directly on established health effects and biological considerations. This means that the assessment is based on a two-step approach. Firstly, the compliance

has to be verified considering the magnetic flux density by means of measurements or calculations. The exposure is compliant if the magnetic flux density does not exceed the reference levels. If the reference levels are exceeded, a dosimetric analysis has to be carried out to compute the dosimetric quantities. The exposure is compliant if these induced quantities are below the basic restrictions. The dosimetric quantity in the low frequency range is the induced electric field.

The ICNIRP guidelines provides different methods to analyse pulsed magnetic fields. The one formally adopted in the last guidelines is the *weighted peak method* (WPM). The WPM was developed by Prof. Jokela in [141] and the ICNIRP introduced it in the statement of 2003 [142] and formally adopted it in the latest guidelines related to low frequency fields [124]. The WPM is summarised by the following expression:

$$|W_j A_j \cos\left(2\pi f_j t + \theta_j + \varphi_j\right)| < 1 \tag{8.1}$$

where A_j and θ_j are the amplitude and the phase of the jth spectral line of the field under analysis. W_j and φ_j are the amplitude and the phase of the weight function at the same frequency. The amplitude of the weight function at a given frequency is defined as the inverse of the peak limit at that frequency. The weight function for the magnetic flux density is shown in Fig. 8.1. The assessment of the magnetic flux
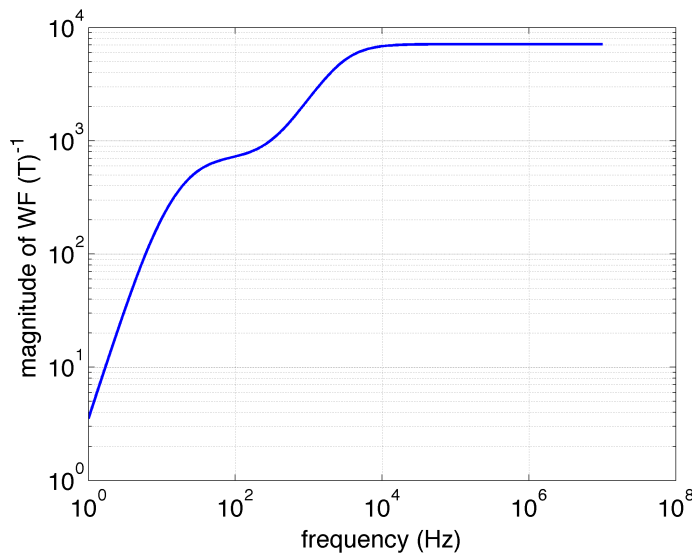
Figure 8.1: Magnitude of the WF used to weight the magnetic flux density.

density by means of the WPM is, in general, like to filter in time domain the field waveform by a suitable high pass filter [142]. However, for a waveform whose spectrum is limited above 10 kHz the WPM corresponds to the application of a scale factor. In fact, the weight is constant above 10 kHz as shown in Fig. 8.1. For this reason, the sinusoidal burst related to the activation of the transmitter can be considered as a continuous sinusoidal waveform. This is shown by comparing the assessment of two
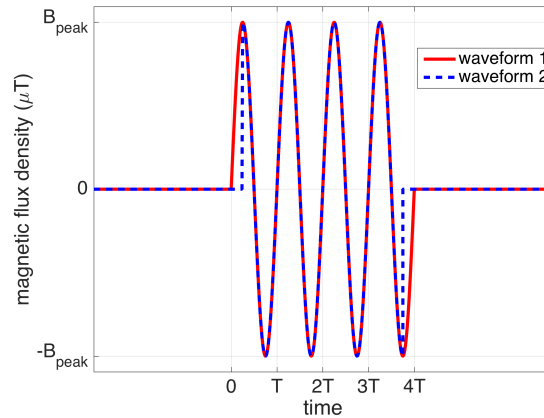
Figure 8.2: Complete (waveform 1) and incomplete (waveform 2) sinusoidal bursts.

sinusoidal burst at different frequencies, 50 Hz and 85 kHz. For each frequency two limit conditions are considered:

1. finite number of cycles

2. incomplete cycle at the beginning and at the end in order to simulate a sharp variation of the field.

Fig. 8.2 shows the two cases for the general waveform at frequency $f = 1/T$. The peak of the waveform is always chosen as the ICNIRP limit at the frequency f.

Fig. 8.3a and Fig. 8.3b represent the left hand side of (8.1) for the waveforms at 50 Hz and 85 kHz, respectively. The sharp variation of the field plays a key role because it corresponds to a high frequency spectral line with respect to the fundamental frequency of the field. For the 50 Hz sinusoidal burst it corresponds also to the maximum exposure because the high pass filter emphasises them as shown in Fig. 8.3a. Conversely, the exposure to a 85 kHz sinusoidal burst is not affected by sharp variations because the WPM becomes a simple scaling factor as explained earlier and as shown in Fig. 8.3b. Therefore, the sinusoidal burst of the present application is equivalent to a continuous sinusoidal waveforms at the same frequency. The same conclusion can be drawn for more smoothed start up transients (as the real transients are) for which the components related to the frequencies lower than the fundamental one are perfectly negligible. These considerations clearly indicate as the compliance of IPT applications can be analysed in the same way under steady state conditions in both cases of stopped or moving vehicle. Consequently, the exposure will be assessed by means of a time-harmonic formulation and the weighted peak method is equivalent to the computation of an exposure index defined as the ratio of the maximum value of the E field and the related exposure limit value. This exposure index corresponds to the maximum value of the right hand side of (8.1).
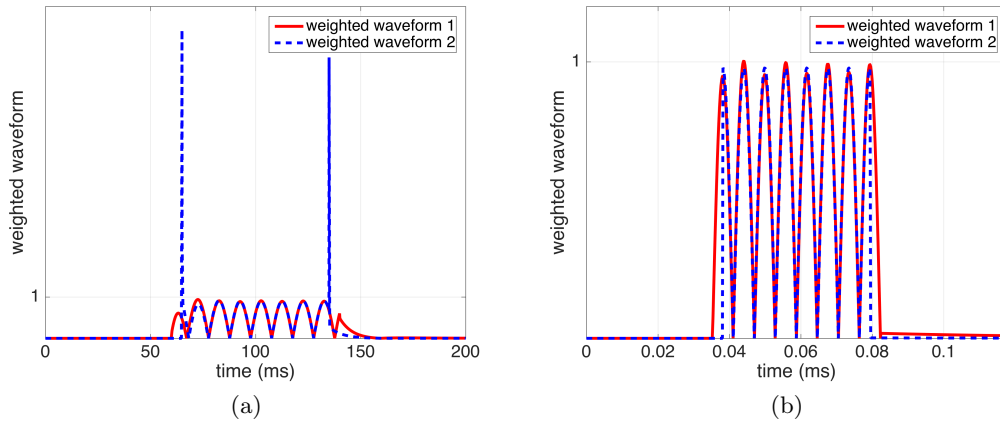
Figure 8.3: Weighted waveforms of the complete and incomplete sinusoidal bursts at 50 Hz (a) and 85 kHz (b). The incomplete burst at 50 Hz is characterised by two peaks in correspondence with the sharp variations. The second waveform at 85 kHz is not characterised by any peaks.

8.1.2   Identification of the worst case scenario

The exposure assessment of the system must take into account the possible misalignment between transmitter and receiver. This analysis becomes more relevant in the stationary case where the vehicle can stop over the transmitter with a high misalignment and people can approach the vehicle remaining in its proximity.

The control of the systems tries to maintain both currents constant at the rated values $I_1 = 36$ A and $I_2 = 67$ A on each side by controlling the rms value of the output voltage of the DC/AC converter and the voltage over the diode bridge by controlling the boost converter (see Chapter 5) . The control on the transmitter side works within a value of mutual inductance higher than 5 μH. Lower values of mutual inductance mean a wider partialisation of the output voltage[1] in correspondence of which the control commands the turn-off (Fig. 8.4). As the value of M changes in function of the relative position between the vehicle and the active transmitter, the map of M versus the misalignment provides information about the working conditions of the systems (voltages and currents according to the relations (5.13) and (5.14)) indicating the points for which the system has to be considered active. In Fig. 8.5 are shown the curves of mutual induction for positive misalignment of the transmitter coil derived through the model described in Section 6.5. As demonstrated in [57] and [133], for distances of the coils larger than 15 cm, the vehicle chassis has no effect on the coupling so the map of M can be considered perfectly symmetric with respect to both x and y misalignments.

The worst case in terms of exposure is identified by computing the magnetic flux density in the inspection volume represented in Fig. 8.7. For every possible misalignment, the maximum field value in the volume and the number of points at which the

---

[1]Angle α close to π rad with ref. to Section 5.3
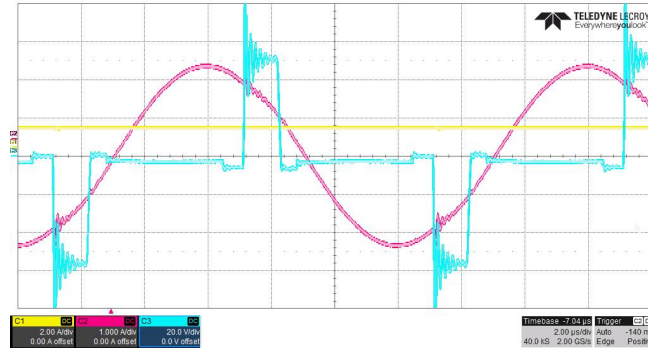
Figure 8.4: Shape of the output voltage of the DC/AC converter (cyan) for a condition of mutual coupling close to the limit of 5 μH. The scope screenshot refers to a test at limited values of DC voltage. Transmitter current in purple and the current at the diode bridge output in yellow are presented.
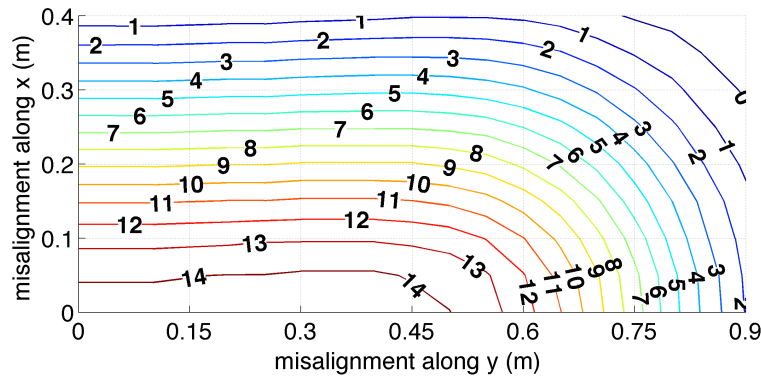
Figure 8.5: Contour lines representing the mutual inductance M (in microhenry) versus the misalignment of the coils axes for a gap of 25 cm.

limit is exceeded are registered. At the frequency of 85 kHz this limit is equal to 27 μT (Fig. 8.6). This procedure makes it possible to define the worst case not only considering the condition that gives place to the maximum magnetic flux density but also the one that presents the larger volume where B exceeds the limit. When the worst case is identified, the dosimetric analysis is carried out evaluating the induced electric field E in the human body. It is worth mentioning that the values of the currents are increased by 5% in order to take into account the possible transients in the currents due to the time required by the control to react against the vehicle misalignment during the motion. This increase is widely conservative as the typical bandwidth of the mechanical transient of the vehicle are much more slower than the dynamic of the converters control.

8.1.3 Problem formulation

The typical distances between the vehicle, the coils and the surrounding space where people could stay is in the order of some meters. For this reason it is necessary to use a suitable formulation of the 3D electromagnetic problem that does not require
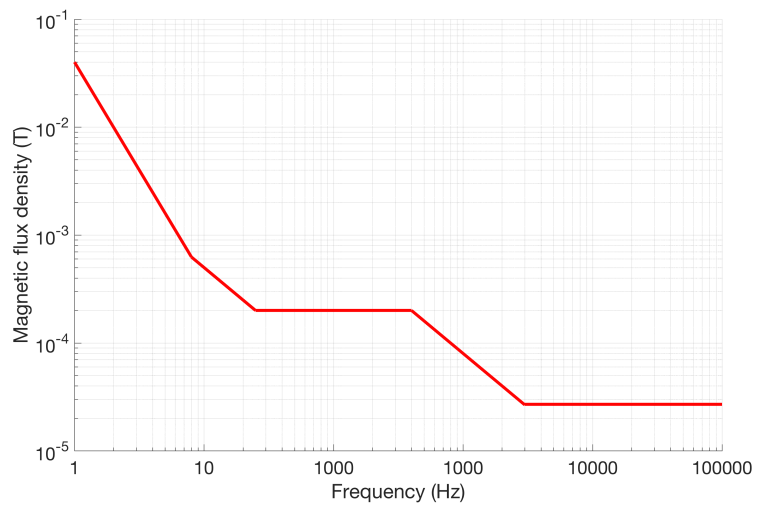
Figure 8.6: Reference levels for exposure to time-varying magnetic fields for general public exposure.
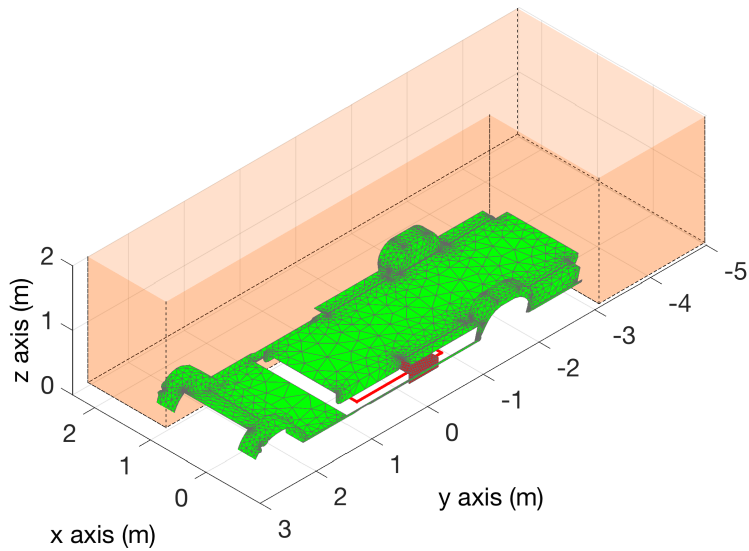
Figure 8.7: Volume for the evaluation of the magnetic flux density.
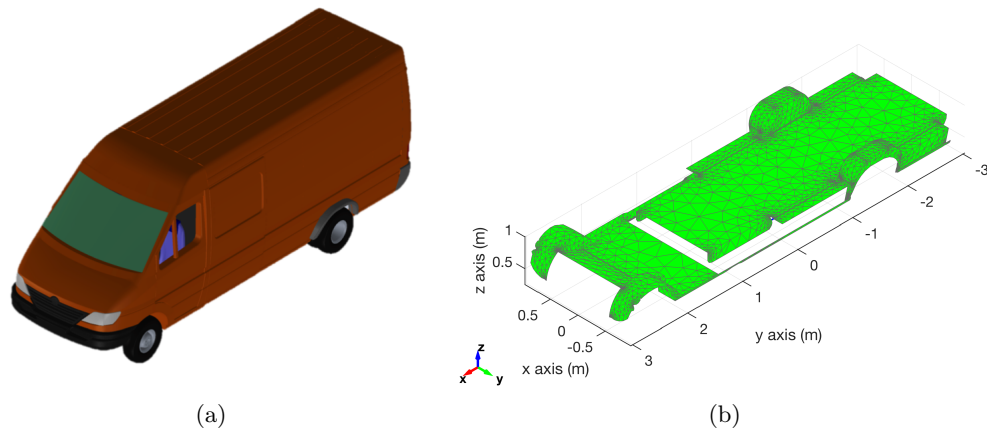
Figure 8.8: 3D CAD model of the complete vehicle (a) and extracted bottom part (b) after the simplification process already meshed.

to mesh the air and that simplifies the computation of the induced phenomena on the vehicle chassis. The selected formulation has relies on the surface impedance boundary conditions (SIBC) applied to the vehicle chassis (Section 6.5) coupled with the boundary element formulation to account for the magnetic field in the open space [132,143]. The magnetic flux density is evaluated in the inspection volume represented in Fig. 8.7. This volume remains in a fixed relative position with respect to the chassis.

The modelling of the vehicle chassis has been restricted to the bottom part only. This is in fact the part of the vehicle that mainly interacts with the magnetic field generated by the coils. The inner part of the vehicle has been proven to be not critical from the point of view of the exposure as the distance of the active parts from the passengers cabin and the presence of the vehicle framework and chassis assure safe conditions. The creation of the model for the simulation started from a complete 3D drawing that has been reduced, as illustrated in Fig. 8.8, eliminating the non conductive components and simplifying the complexities represented by holes, extremely thin and sharp objects as bolts, tether hooks etc. After some manual refinement of the mesh, the model resulted in about 19000 elements. The dosimetric analysis makes use of the human model Duke, a 34 years old male of the Virtual Population based on high resolution MRI scans [144]. The voxel resolution of $2 \times 2 \times 2$ mm^3 is used. This dimension is indicated by the reference standard as a compromise that satisfies the computational constraint maintaining a good correlation with the biological basis. Since the presence of the human body does not modify the external magnetic field, the exposure is assessed by means of the scalar potential finite difference technique expressed in its the algebraic form [145]. The compliance is checked at one representative voxel for each tissue. These voxels are the ones at which the electric field magnitude is the 99th percentile [124].

(a)

(b)
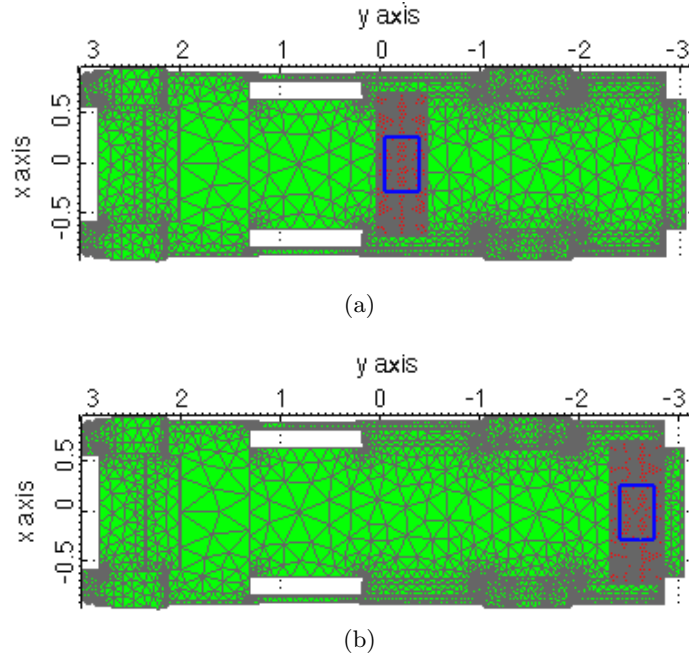
Figure 8.9: Analysed position for the receiver structure mounting. Receiver mounted on the centre of the chassis (a). Receiver on the rear (b). Receiver structure is coloured in red while the receiver coil is in blue.

8.2   Results

As already mentioned in Section 6.1, the adopted vehicle presented two possible mounting positions for the receiver structure, on the centre of the chassis or in the rear as illustrated in Fig. 8.12. Although the considered position for the design has been the one in the centre, both cases have been analysed.

8.2.1   Case 1: receiver on the centre

In this case, the active transmitter is always covered by the body of the vehicle. As shown in Fig. 8.10, the worst case condition in terms of maximum B occurs for a misalignment of -0.3 cm along x and 0.55 cm along y. The corresponding B value is 72 μT. This condition coincides also with the misalignment with maximum number of points exceeding the limit as shown in Fig. 8.11. Therefore, it represents the general worst case. The volume in which the magnetic flux density exceeds the limit is represented in Fig. 8.12a. The induced electric field is evaluated placing the human body in this volume (Fig. 8.12b). Fig. 8.13 shows the exposure indexes at some target tissues (i.e. the tissues in which the highest exposure indexes appear). It is apparent that the condition (8.1) is satisfied at all tissues. Therefore the exposure is compliant by a wide margin.
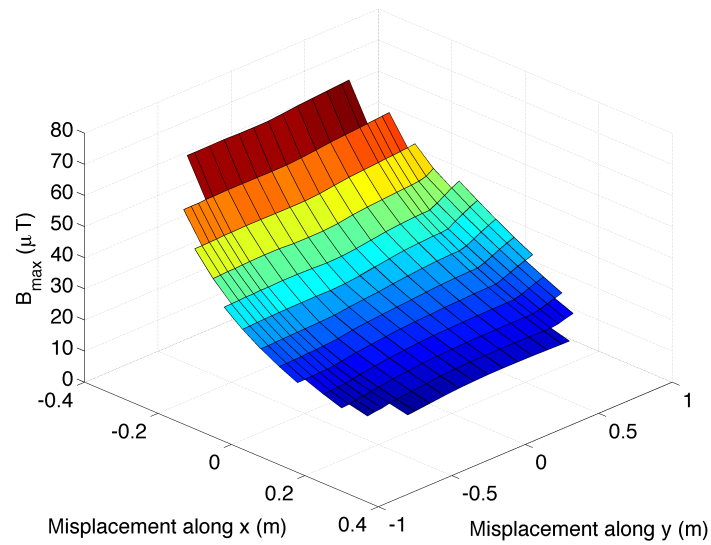
Figure 8.10: Maximum value of the magnetic flux density versus the coils misalignment in the case of receiver mounted on the center. Missing points correspond to condition of coupling in correspondence of which the system is turned off.
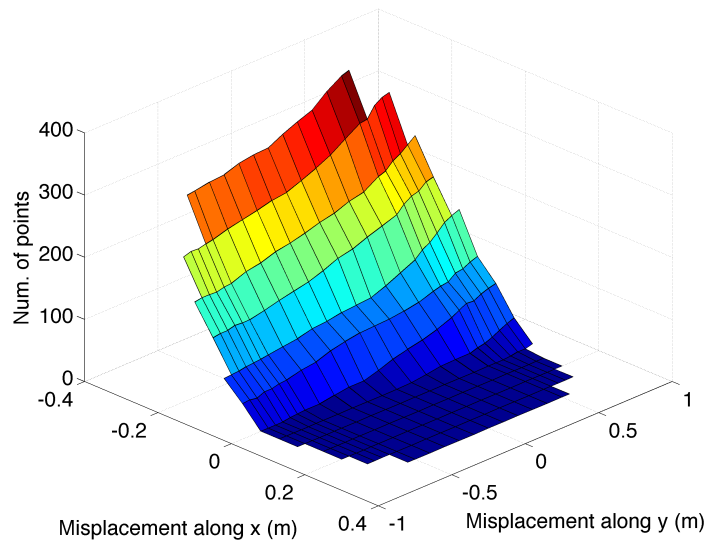
Figure 8.11: Dimension of the volume having magnetic flux density higher then the limit value of 27 μT. Missing points refer to conditions of coupling in correspondence of which the system is turned off.

(a)   (b)
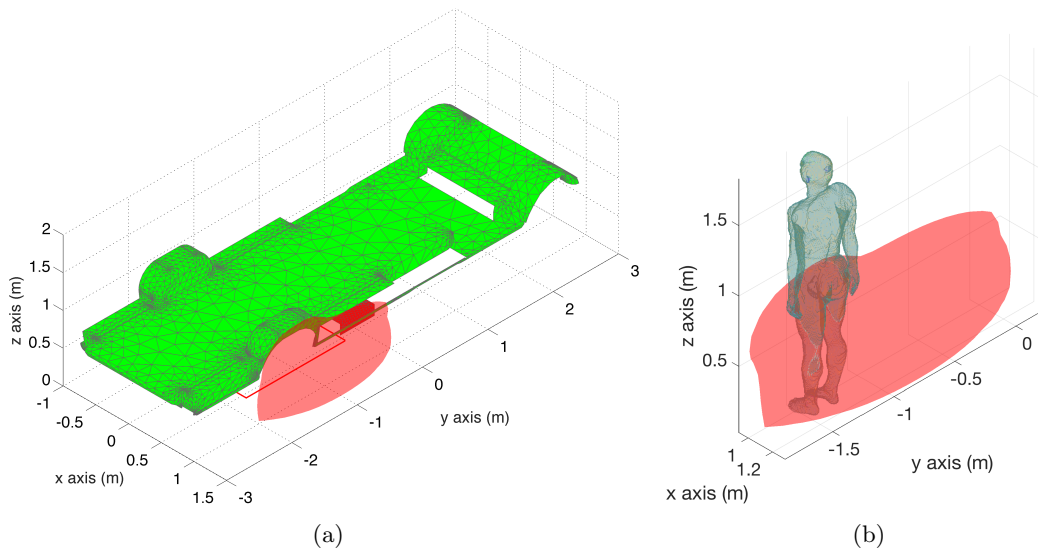
Figure 8.12: Surfaces at the limit value of 27 μT of magnetic field density in the worst cases (a) and positioning of the Duke model in the volumes exceeding the limit of magnetic flux density (b). Case 1.
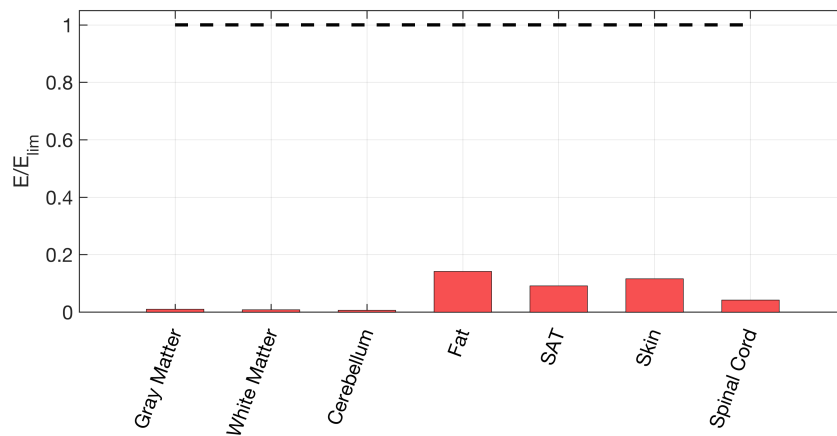
Figure 8.13: Exposure index on the target tissues for the analysed worst case (Case 1).
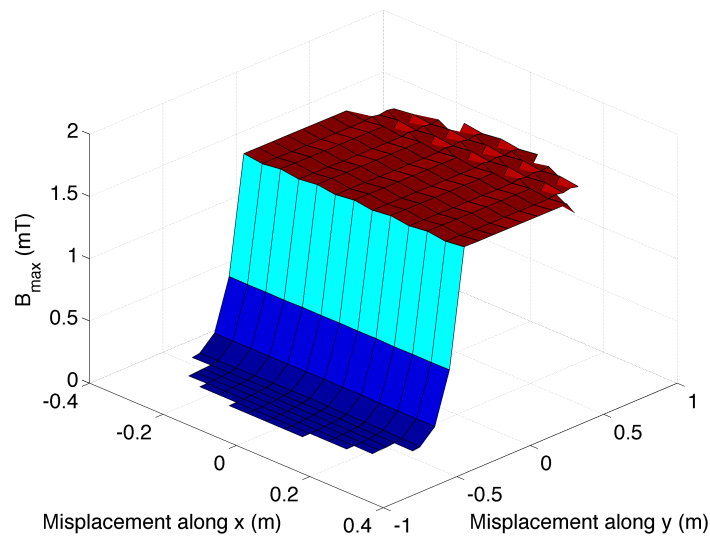
Figure 8.14: Maximum value of the magnetic flux density versus the coils misalignment in the case of receiver mounted on the rear. Missing points correspond to condition of coupling in correspondence of which the system is turned off.

8.2.2   Case 2: receiver on the rear

As visible in Fig. 8.14, this case is more critical because the transmitter can be completely uncovered by the vehicle. As shown in Fig. 8.14, after a given misalignment along y direction, the maximum B in the inspection value remains practically constant. In this case the worst case condition is identified by means of the extension of the volume where the limit of B is exceeded. The worst case occurs for a misalignment of 0.1 cm along x and 0.8 cm along y. The related volume where B exceeds the limit is represented in Fig. 8.15. The human model is placed at the point corresponding to the maximum intersection between this volume and the body as shown in Fig. 8.16b. Fig. 8.17 shows the exposure indexes at some target tissues.

In this case the exposure is not compliant (index >1). According to this result, this last mounting position is not advisable. A proposed way to protect people in this case is the definition of a safety distance. As depicted in Fig. 8.18, this distance has been evaluated by considering the borders of the volumes where the limit of B is exceeded for different positions of the vehicle. The safety distance is then defined as the minimum distance from the active transmitter along the x axis that guarantees the respect of the reference level (conservative condition). It has been fixed at 75 cm far from the transmitter.
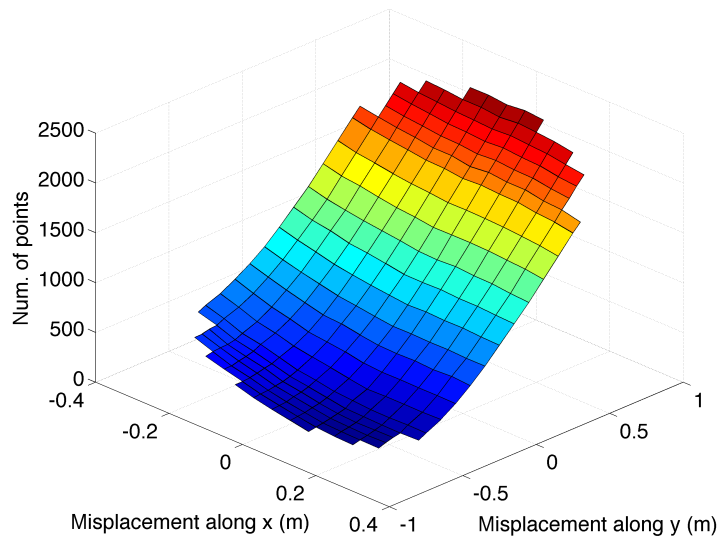
Figure 8.15: Dimension of the volume having magnetic flux density higher then the limit value of 27 μT. Missing points refer to conditions of coupling in correspondence of which the system is turned off.
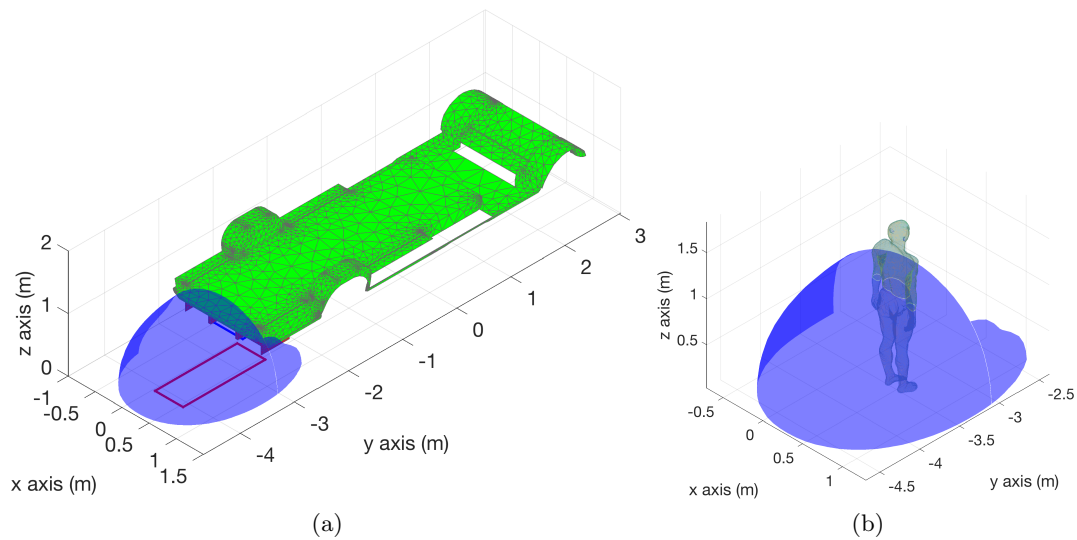
Figure 8.16: Surfaces at the limit value of 27 μT of magnetic field density in the worst cases (a) and positioning of the Duke model in the volumes exceeding the limit of magnetic flux density (b). Case 2.
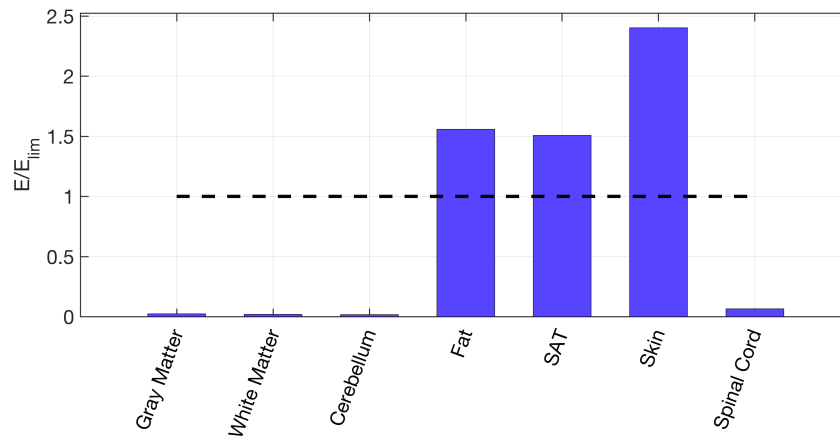
Figure 8.17: Exposure index on the target tissues for the analysed worst case (Case 2).
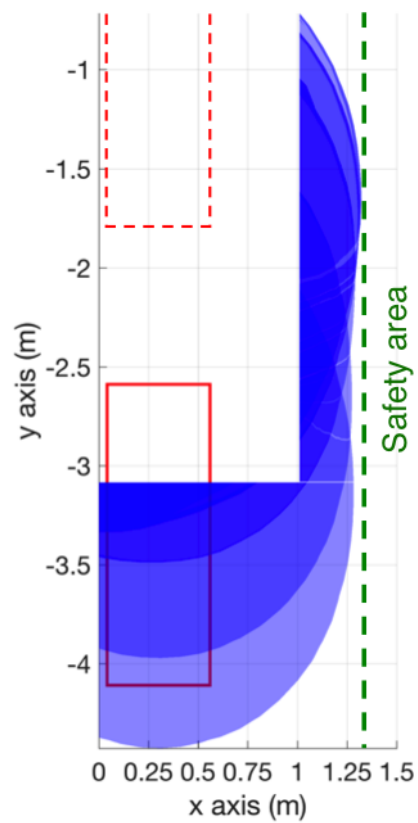
Figure 8.18: Definition of the safety area. Different volumes where the limit of B is exceeded in blue. Transmitters in red. The dashed one represents the subsequent not active transmitter. The dashed green line represents the border of the safety area.

Figure 8.19: Positioning of the vehicle on the wooden base for the emulation of a the condition of transmitter at 5 cm under the ground level.

8.3   Measurements

A test setup has been created in order to verify the consistency of the values of magnetic flux density provided by the model.

The test has been conducted in an outdoor environment. The adopted transmitter has been one of the transmitters resulted from the final design. It has been left movable and directly placed at the ground level. The receiver has been mounted on the vehicle rear. A measurement has been carried out to verify the inductive behaviour of the coil with the methods adopted in Chapter 7. The vehicle wheels have been placed over four wooden bases of height 5 cm (Fig. 8.19) in order to emulate the nominal conditions of distance between the coils of 25 cm with the transmitter embedded in the road. This solution is flexible and precise as it did not imply the movement of the vehicle for the coil positioning. The transmitter has been placed in order to be completely covered by the vehicle and in absence of lateral misalignment with respect to the receiver. The system has been supplied at one third of the rated currents (by using one third of the rated DC bus voltage) in order to guarantee the operation of measurements in safe conditions with respect to the exposure. The ELT 400 Exposure Level Tester [146] has been used to measure the rms value of the magnetic flux density. The instrument has been equipped with the three-axial ELT B-Field-Probe (the instrument is visible in Fig. 8.20a).

Taking as reference the lateral side of the vehicle and the effective ground floor, an inspection grid of $3 \times 3 \times 3$ points has been defined according to the representation of Fig. 8.20. The first point P_1 lies at 5 cm above the effective ground floor (in orange in Fig. 8.20) and 1 cm from the plane tangent to the vehicle and perpendicular to the ground floor (light blue plane in Fig. 8.20). The point P_2 is aligned with the centre of symmetry of the receiver structure. The magnetic flux density has been then measured in correspondence of the 27 inspection points that formes the grid. Hence, the same condition of test has been repeated in simulation. The measured and calculated values of magnetic flux density are collected in Table 8.1. The comparison indicates that the values provided by the model can be considered consistent with respect to the measured values.
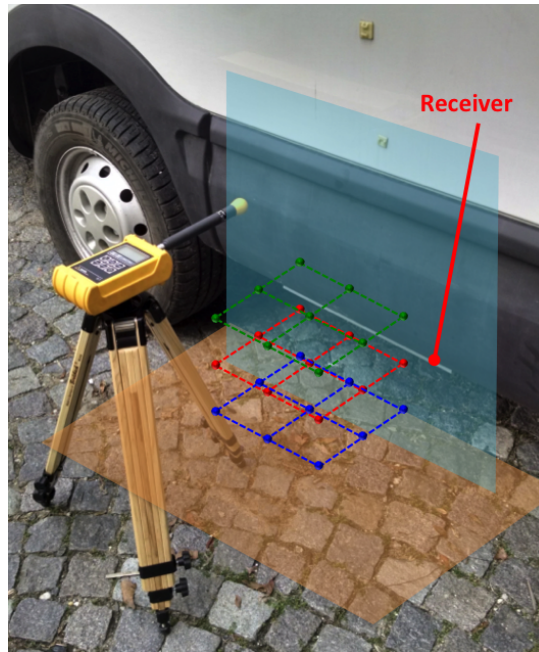
(a)
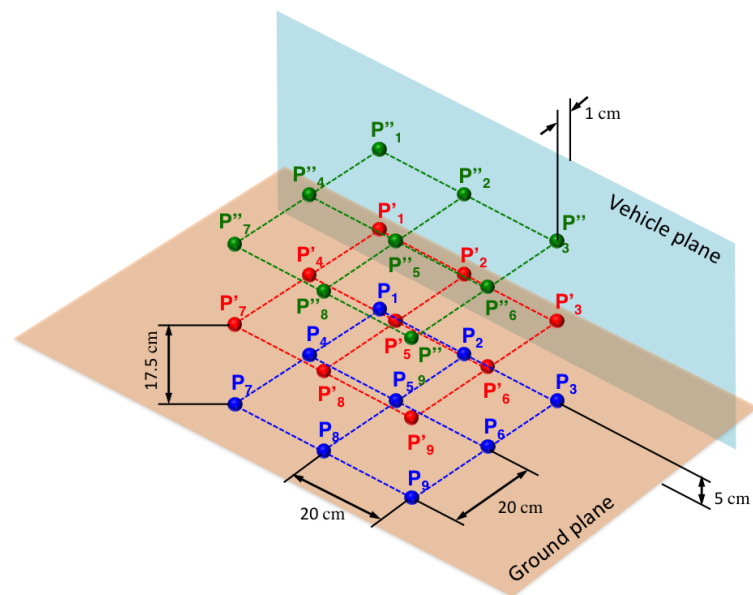
(b)

Figure 8.20: Inspection grid for the measurements of the magnetic flux density. The inter-distance between each layer is equal to 17.5 cm. The points in the plane are at a distance of 20 cm from each other.

Table 8.1: Comparison between calculated and measured values over the inspection grid of Fig. 8.20.

Point	Plane height (cm from the ground)	Calculated value (μT)	Measured value (μT)
P_1	5	6.4	6.1
P_2		7.2	6.3
P_3		7.5	6.3
P_4		3.6	3.4
P_5		3.9	3.4
P_6		4.0	3.4
P_7		2.2	1.9
P_8		2.4	2.0
P_9		2.4	2.0
P_1'	17.5	6.5	6.6
P_2'		7.5	6.9
P_3'		8.0	6.7
P_4'		3.7	3.2
P_5'		4.0	3.4
P_6'		4.2	3.4
P_7'		2.2	1.9
P_8'		2.4	2.2
P_9'		2.4	2.0
P_1''	35	6.3	5.4
P_2''		7.6	5.3
P_3''		8.2	5.2
P_4''		3.5	2.7
P_5''		3.8	2.8
P_6''		3.9	2.9
P_7''		2.1	1.7
P_8''		2.3	1.8
P_9''		2.3	1.8

8.4 Conclusions

In this chapter a methodology suitable to asses the human exposure to the magnetic fields created by dynamic and static IPT systems has been proposed. This methodology has been applied to the IPT system object of the present thesis. It has been shown that the pulsed magnetic fields can be assessed easily with a time-harmonic formulation in a way independent of the turn-on transient of the system. Moreover, two indicators are proposed to identify the worst case exposure scenario: the maximum value of magnetic flux density and the volume in which a given limit is exceeded. The use of two indicators has been particularly useful for the assessment in the case of receiver mounted on the vehicle rear. Finally, a test reproducing the final on-road system, has shown a good consistency of the results provided in simulation.

Chapter 9

Conclusion and future developments

The present work has tried to give an answer to some of the open issues in the domain of the dynamic IPT oriented to the transportation sector. The different activities aimed at the development of a prototype of IPT and its integration in a real infrastructure and on an existing vehicles. In this sense, all the developed methodologies and the proposed solutions are generally applicable to every IPT system.

The entire work has been based on the development of a simple circuital model able to describe the phenomena of magnetic induction between the main components represented by the transmitter and the receiver coils. The first harmonic approximation has been used to represent the source (a DC/AC converter) and the load (an AC/DC converter) connected to the coils using common elements of the electrical circuits theory. The same approximation has allowed the study of the model in the frequency domain.

The analyses based on this model have indicated the necessity to increase the frequency and compensate the reactances of the coils in order to improve the power transfer capability of the system and reduce the power rating of the source. Among the different possibilities for the connection of the capacitors, the series-series compensation has been considered the most suited for the application in dynamic IPT systems. For this compensation topology, both capacitors have to be chosen to resonate with the respective coil at a common frequency.

In resonance condition, the system shows a resistive behaviour to the source. This introduces a second advantage represented by the possibility of adopting soft switching techniques that reduce ideally to zero the commutation losses in the switches of the DC/AC converter. However, the analysis in the frequency domain has shown that, according to the tolerances in the components manufacturing, it is practically impossible to obtain a purely resistive behaviour. Moreover, under specific conditions of load and coupling, the phase of the systems can abruptly vary in a small interval of

frequency around the resonance. This phenomenon could be mitigated in the design phase but it can appear dynamically as a consequence of coupling variations. This variation is practically unavoidable in the dynamic application.

An H-bridge whose switches are based on the parallel of an IGBT and a SiC MOSFET has been proposed to overcome this problem. This hybrid architecture has allowed to handle both soft and hard switching with a good efficiency. A dedicated setup based on the opposition method has been developed and used to test the converter efficiency and the capability to handle conditions of slightly inductive or capacitive load. The management of the power on the receiver side has been provided by a diode bridge and a boost converter acting as voltage regulator toward the diode bridge. The frequency of switching has been fixed at 85 kHz to keep the compliance with the SAE J2954 standard as a base for future interoperability between static and dynamic systems.

A procedure for the design of the coils has been proposed in Chapter 6. It is based on the evaluation of a desired value of mutual inductance using the resonance frequency and the rated values of voltage and currents of source and load as preliminary information. A magnetic structure composed by ferrite and aluminium has been added to the coil in order to confine the magnetic flux in a better defined region and lower the leakage flux independently of the geometry of the underside of the vehicle. The shape of the structure has been optimised through a differential evolution strategy whose goals have been the maximisation of the coupling and the minimisation of the losses in the aluminium.

The dimensions of the transmitter have been chosen as a compromise between the stability of the transfer during the vehicle movement and the minimisation of the stray field. The transmitter has been designed to be placed in the road without the insertion of ferrite according to the goals of reduction of the costs per meter and the implementation of an object suited for the direct embedding in the road pavement.

The different tests related to the embedding of the transmitter in the road pavement represent the part of the work that provided the larger amount of information useful for the integration of the future dynamic IPT systems in the road infrastructure. The problem of the capacitive coupling of the coil with the ground turned out to be a challenging issue for systems working at frequencies higher than 15-20 kHz. A solution to overcome this problem has been proposed based on the insertion of a non conductive material acting as a dielectric between the coil and the ground. The insertion of this dielectric layer has allowed the reduction of the capacitance toward the ground moving the phenomena of resonance at higher frequencies far from the working frequency.

Finally, the problem of the human exposure to the magnetic field involved in the IPT has been treated. A methodology suitable to asses the human exposure to the pulsed magnetic fields created by dynamic IPT systems has been proposed. It has

been based on the ICNIRP 2010 guidelines and the application of the weighted peak method. The methodology applied to the developed system indicated the installation of the receiver on rear of the vehicle as not advisable.

Different aspects have not been analysed in the present work. The more important is surely the control of the system in dynamic conditions. The researches on this topic are conducted in parallel by other colleagues of the POLITO team. The results have been partially published and others will be available in the next months. The tests on the complete system, that will begin next year, will provide the conclusive results about the proposed solutions providing also the informations for future refinements and developments.

Appendix A

Equivalent representations of coupled inductors

In the present thesis, the magnetic coupling between transmitter and receiver has been represented through the model of the mutual coupled inductances recalled in Fig. A.1. However, different models can be used to represent the same phenomenon. The mainly used models in the literature on IPT are here briefly summarised. The correlation with the mutual coupled inductances model is pointed out.

A.1 Transformer model

One of the most used two-port representations, treats the coupled inductors as a transformer. To properly define its parameters it is necessary to chose a transformation ratio n. The value of n can be chosen arbitrarily among the positive real numbers that respect the conditions [147]:

$$L_1 - nM \geq 0, n^2 L_2 - nM \geq 0 \tag{A.1}$$

$$\frac{M}{L_2} \leq n \leq \frac{L_1}{M} \tag{A.2}$$
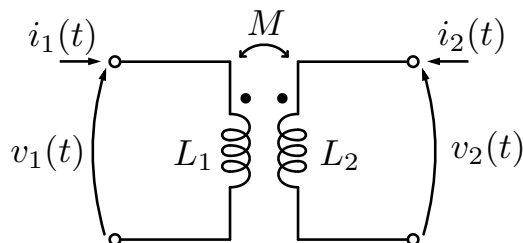
Figure A.1: Representation mutually coupled circuits
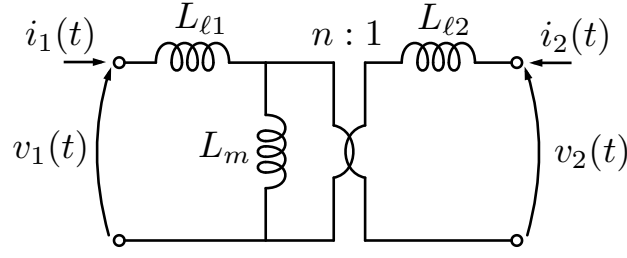
Figure A.2: Equivalent transformer circuit

This partial arbitrariness of the value of n permits different definitions that lead to different circuit representation. Choosing n as in (A.3), it is possible to express the transformer ratio as function of the only self-inductances.

$$n = \sqrt{\frac{L_1}{L_2}} \tag{A.3}$$

With this definition of n, it is possible to define two leakage inductances $L_{\ell 1}$ and $L_{\ell 2}$ and an inductance of magnetisation L_m, as in (A.4), with the circuital representation of Fig. A.2.

$$\begin{cases} L_{\ell 1} = L_1 - nM \\ L_{\ell 2} = n^2 L_2 - nM \\ L_m = nM \end{cases} \tag{A.4}$$

With respect to a classical transformer (for which the coupling factor k is ≈ 1), the coupled inductors of an IPT systems are weekly coupled. This mirrors in the condition

$$L_{\ell 1} L_{\ell 2} \gg L_m \tag{A.5}$$

This implies that the voltage drop over the leakage inductances cannot be neglected and the same happens for the magnetising current. On the contrary this approximation is practically always possible for classical transformers. Under these conditions, the transformer ratio n is far from being equal to the ratio of the voltages v_1 and v_2. Following the simple steps of (A.6), it is possible to note that, the voltage v_m at the input of the ideal transformer is much lower the lower is the coupling.

$$v_m = v_1 \left(\frac{L_m}{L_m + L_1} \right) = v_1 \left(\frac{nM}{nM + L_1 - nM} \right) = v_1 \frac{nM}{L_1} =$$

$$= v_1 \left(\sqrt{\frac{L_1}{L_2}} \frac{M}{L_1} \right) = \tag{A.6}$$

$$= v_1 \left(\sqrt{\frac{L_1}{L_2}} \frac{M}{L_1} \sqrt{\frac{L_1}{L_1}} \right) = v_1 \left(\frac{M}{\sqrt{L_2 L_1}} \right) = k v_1$$
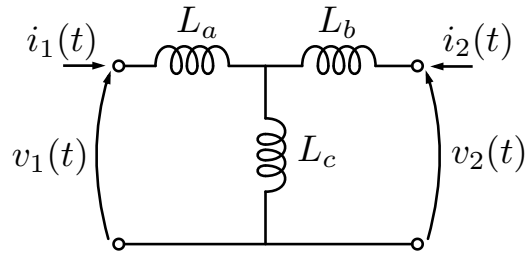
Figure A.3: Equivalent T circuit

Moreover, for a classical transformer, the transformer ratio can be expressed as in (A.7) since the reluctance of the primary and the secondary magnetic circuit is the same.

$$\frac{N_1}{N_2} = \sqrt{\frac{L_1}{L_2}} \tag{A.7}$$

In the case of IPT systems this assumption is no more generally valid. All these considerations underline as, in the IPT systems, the turns ratio is far from being assimilable to a classical transformer ratio loosing the direct correlation between geometry, magnetic parameters and electrical quantities at the model ports.

A.2   T-model

The T-*model* is another frequently used way to transform the two distinct circuits of the mutual coupled inductances model in a single two-port model. It can be directly derived form the last mentioned model. Moreover, it can be seen as a particular case of the transformer model for which $n = 1$. It is represented as in Fig. A.3 and described by the equation set

$$\begin{cases} L_a = L_1 - M \\ L_b = L_2 - M \\ L_c = M \end{cases} \tag{A.8}$$

This representation is simpler than the previous one as it eliminates the ideal transformer component. However, also if the components can be assimilated to leakage and magnetisation inductances, their meaning is not strictly physical. As example, let consider a case with a transmitter having much more turns than the receiver. For equal geometries of the coils, this case leads to the condition

$$L_1 \gg L_2 \tag{A.9}$$

In the same time, the condition (A.10) can be verified.

$$M > L_2 \tag{A.10}$$
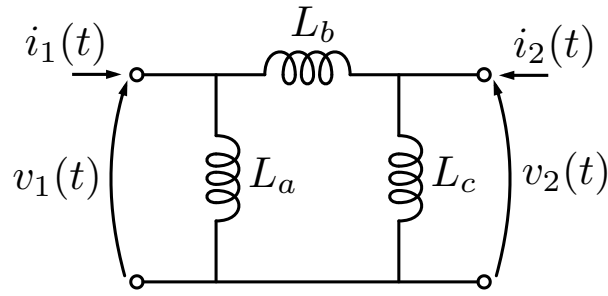
Figure A.4: Equivalent Π circuit

According to (A.8), this case implies a value of $L_b < 1$ that has no physical meaning. Nevertheless, nothing changes for the voltages and currents at the system terminals. This means that, also if the model does not provide physical information about voltages and currents on the real magnetic components, it can provide a good description about the interface with the other components (power electronics).

A.3   Π-model

A third possible representation called π-*model* is reported for the sake of completeness. It takes its name from the shape depicted in Fig. A.4. Its correlation with the mutual coupled inductors model is expressed as:

$$\begin{cases} L_a = \dfrac{L_1 L_2 - M^2}{L_2 - M} \\[3mm] L_b = \dfrac{L_1 L_2 - M^2}{L_1 - M} \\[3mm] L_c = \dfrac{L_1 L_2 - M^2}{M} \end{cases} \tag{A.11}$$

This model is the less used as their parameters are not directly linked to the physical phenomena of the IPT. As happens for the T-model, one of the cross parameters can be negative.

A.4   Adopted model

In the present work, the mutual coupled inductors model has been chosen to represent the IPT system as it has been considered the one more directly linked to the physics of the problem. Moreover, it provided the higher quantity of informations as the voltages and currents on the magnetic elements are the quantities really present in the

components. Its mathematical manipulation has allowed to provide useful parameters as the total and reflected impedances in a compact way.

Appendix B

Maximum power transfer on the receiver side

This appendix is dedicated to the demonstration of the relation for the selection of the compensation capacitor connected receiver. Both cases introduced in Chapter 3 of parallel and series connection are analysed.

Fig. B.1 shows a circuit representation of the series compensated receiver. The induced voltage $\hat{V}_{oc}$ and the receiver self-inductance L_2, included in the blue box, can be seen as the source and the impedance of a Thevenin equivalent circuit. Then, the impedance of L_2 can be indicated as a source impedance $\hat{Z}_S$. In the same way it is possible to consider an equivalent load $\hat{Z}_L$ composed by the series of the load resistor and the compensation capacitance:

$$\hat{Z}_L = \frac{R_L \dfrac{1}{j\omega C_2}}{R_L + \dfrac{1}{j\omega C_2}} \tag{B.1}$$

In this case, the application of the principle of maximum power transfer to the load
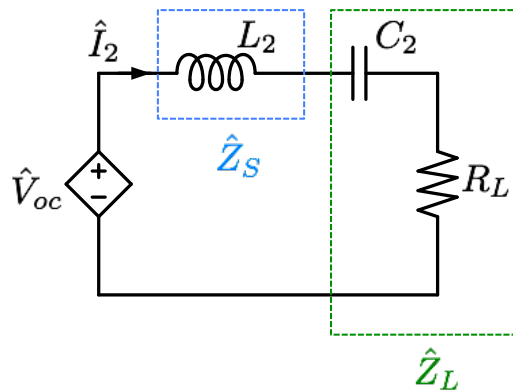
Figure B.1: Model of the series compensated receiver.
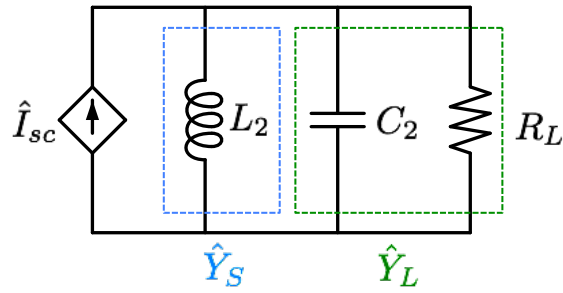
Figure B.2: Model of the parallel compensated receiver.

R_L. implies the respect of the relation

$$Im(\hat{Z}_L) = -\frac{1}{\omega C_2} = Im(\hat{Z}_S) = \omega L_2 \tag{B.2}$$

that means to operate at the resonance condition

$$\omega_0^2 L_2 C_2 - 1 = 0 \tag{B.3}$$

In the case of parallel compensation, the Norton representation shown in Fig. B.2 is more useful. In that case the maximum power transfer to the load happens if the imaginary part of the load admittance $\hat{Y}_L$ is equal to the source admittance $\hat{Y}_S$. This implies again the condition (B.3). In the resonance condition, the equivalent admittance composed by the parallel of L_2 and C_2 is equal to zero meaning that the current flows only toward the load.

Both compensations indicate the same condition for the selection of the compensation capacitors indicated in Section 3.3. It is worth noting that the extracted relationships are approximated and valid under the conditions of negligible resistances of coils and capacitor.

Bibliography

[1] W. Bernhart, T. Schlick, D.-K. I. Olschewski, D.-I. M. Thoennes, and J. Garrelfs, "E-mobility index for Q3 2013," 2013.

[2] R. Shepard, "Tesla motors." https://ryansheppard.me/static/files/tesla.pdf. Accessed in March 2016.

[3] "European Parliament legislative resolution of 15 april 2014 on the proposal for a directive of the European Parliament and of the Council on the deployment of alternative fuels infrastructure (COM(2013)0018 - C7-0022/2013 - 2013/0012(COD))," Apr. 15 2014.

[4] "eCo-FEV project website." https://www.eco-fev.eu/. Accessed in October 2016.

[5] "FABRIC project website." http://www.fabric-project.eu/. Accessed in October 2016.

[6] M. Faraday, "Experimental researches in electricity," *Philosophical Transactions of the Royal Society of London*, vol. 122, pp. 125–162, 1832.

[7] D. J. Cichon and W. Wiesbeck, "The Heinrich Hertz wireless experiments at Karlsruhe in the view of modern communication," in *100 Years of Radio., Proceedings of the 1995 International Conference on*, pp. 1–6, IET, 1995.

[8] N. Tesla, "The transmission of electrical energy without wires," *Electrical World and Engineer*, vol. 1, 1904.

[9] S. S. Valtchev, E. N. Baikova, and L. R. Jorge, "Electromagnetic field as the wireless transporter of energy," *Facta universitatis-series: Electronics and Energetics*, vol. 25, no. 3, pp. 171–181, 2012.

[10] N. Tesla, "World system of wireless transmission of energy," *Telegraph and Telephone Age*, 1927.

[11] N. Tesla, "Apparatus for transmission of electrical energy," May 15 1900. US Patent 649,621.

[12] G. I. Babat, "Electrodeless discharges and some allied problems," *Electrical Engineers - Part III: Radio and Communication Engineering, Journal of the Institution of*, vol. 94, pp. 27–37, January 1947.

[13] George Iljitch Babat, "High frequency electric transport system with contactless transmission of energy," September 1951. Application number GB926946A.

[14] D. V. Otto, "Power supply equipment for electrically-driven vehicle," June 19 1974. JP Patent 49 063 111.

[15] G. A. Covic and J. T. Boys, "Inductive power transfer," *Proceedings of the IEEE*, vol. 101, no. 6, pp. 1276–1289, 2013.

[16] S. E. Shladover *et al.*, "Path at 20-history and major milestones," *IEEE Transactions on intelligent transportation systems*, vol. 8, no. 4, pp. 584–592, 2007.

[17] J. Boys and A. Green, "Inductive power pick-up coils," Apr. 27 1995. WO Patent App. PCT/NZ1994/000,115.

[18] J. Boys and A. Green, "Flux concentrator for an inductive power transfer system," Oct. 13 1998. US Patent 5,821,638.

[19] "Award for conductix-wampfler: Wireless charging of electric vehicles." http://www.conductix.com/sites/default/files/downloads/PR%2011-02-14%20Award%20for%20Conductix-Wampfler.pdf. Accessed in October 2016.

[20] "WAVE website." http://www.waveipt.com/. Accessed in October 2016.

[21] "PRIMOVE Bombardier website." http://primove.bombardier.com/applications/e-bus.html. Accessed in October 2016.

[22] I. Suh, "Application of shaped magnetic field in resonance (SMFIR) technology to future urban transportation," in *CIRP design conference*, 2011.

[23] S. Ahn and J. Kim, "Magnetic field design for high efficient and low EMF wireless power transfer in on-line electric vehicle," in *Antennas and Propagation (EUCAP), Proceedings of the 5th European Conference on*, pp. 3979–3982, IEEE, 2011.

[24] J. Huh, S. W. Lee, W. Y. Lee, G. H. Cho, and C. T. Rim, "Narrow-width inductive power transfer system for online electrical vehicles," *Power Electronics, IEEE Transactions on*, vol. 26, no. 12, pp. 3666–3679, 2011.

[25] "HaloIPT to provide induction charging system for Phantom EE." http://www.greencarcongress.com/2011/03/haloipt-to-provide-induction-charging-system-for-phantom-ee.html, Mar. 2 2011. Accessed in march 2016.

[26] "Toyota licenses WiTricity patent portfolio for wireless power." http://witricity.com/news/toyota-licenses-witricity-patent-portfolio-for-wireless-power/, Dec. 5 2013. Accessed in march 2016.

[27] R. W. Carlson and B. Normann, "Test results of the plugless inductive charging system from evatran group, inc," *SAE Int. J. Altern. Powertrains*, vol. 3, pp. 64–71, 2014.

[28] J. Schneider, "SAE J2954 overview and path forward," 2013.

[29] A. Gil and J. Taiber, "A literature review in dynamic wireless power transfer for electric vehicles: Technology and infrastructure integration challenges," in *Sustainable Automotive Technologies 2013*, pp. 289–298, Springer, 2014.

[30] "SAE international web site." http://standards.sae.org/wip/j2954/, Mar. 31 2016. Accessed in October 2016.

[31] M. Emre, P. Vermaat, D. Naberezhnykh, Y. Damousuis, T. Theodoropoulos, V. Cirimele, and A. Doni, "D 3.3.1 - Review of existing power transfer solutions," *Public Deliverable EU FABRIC project (605405)*, 2014.

[32] "IEC 61980-1:2015 Electric vehicle wireless power transfer (WPT) systems – Part 1: General requirements." https://webstore.iec.ch/publication/22951. Accessed in October 2016.

[33] "ISO/DPAS 19363. Electrically propelled road vehicles – Magnetic field wireless power transfer – Safety and interoperability requirements." hhttp://www.iso.org/iso/catalogue_detail.htm?csnumber=64700. Accessed in October 2016.

[34] C. Kalialakis and A. Georgiadis, "The regulatory framework for wireless power transfer systems," *Wireless Power Transfer*, vol. 1, no. 02, pp. 108–118, 2014.

[35] J. Taiber, "Electric vehicle wireless power transfer," *Industry connections activity initiation document (ICAID). Version*, vol. 1, p. 12, 2013.

[36] "Road standards and paving standards." http://www.astm.org/Standards/road-and-paving-standards.html. Accessed in march 2016.

[37] J. M. Miller, O. C. Onar, C. White, S. Campbell, C. Coomer, L. Seiber, R. Sepe, and A. Steyerl, "Demonstrating dynamic wireless charging of an electric vehicle: The benefit of electrochemical capacitor smoothing," *Power Electronics Magazine, IEEE*, vol. 1, no. 1, pp. 12–24, 2014.

[38] "UNPLUGGED project website." http://unplugged-project.eu/wordpress/. Accessed in march 2016.

[39] "Fastincharge project website." http://www.fastincharge.eu/index.php. Accessed in march 2016.

[40] V. Cirimele, M. Diana, N. El Sayed, F. Freschi, and P. Guglielmi, "An innovative next generation E-mobility infrastructure: The eCo-FEV project," in *Electric Vehicle Conference (IEVC), 2014 IEEE International*, pp. 1–7, Dec 2014.

[41] "ENDESA develops wireless en-route charging for electric buses in malaga." http://www.endesa.com/en/saladeprensa/noticias/wireless-en-route-charging-electric-buses. Accessed October 2016.

[42] A. Amditis, G. Karaseitanidis, I. Damousis, P. Guglielmi, and V. Cirimele, "Dynamic wireless charging for more efficient FEVS: The fabric project concept," in *MedPower 2014*, pp. 1–6, Nov 2014.

[43] S. Choi, J. Huh, W. Lee, S. Lee, and C. Rim, "New cross-segmented power supply rails for roadway-powered electric vehicles," *Power Electronics, IEEE Transactions on*, vol. 28, pp. 5832–5841, Dec 2013.

[44] G. Covic and J. Boys, "Modern trends in inductive power transfer for transportation applications," *Emerging and Selected Topics in Power Electronics, IEEE Journal of*, vol. 1, pp. 28–41, March 2013.

[45] O. C. Onar, J. M. Miller, S. L. Campbell, C. Coomer, C. White, L. E. Seiber, *et al.*, "A novel wireless power transfer for in-motion EV/PHEV charging," in *Applied Power Electronics Conference and Exposition (APEC), 2013 Twenty-Eighth Annual IEEE*, pp. 3073–3080, IEEE, 2013.

[46] J. Meins and K. Vollenwyder, "System and method for transferring electric energy to a vehicle," Jan. 29 2013. US Patent 8,360,216.

[47] G. Nagendra, L. Chen, G. Covic, and J. Boys, "Detection of EVs on IPT Highways," *Emerging and Selected Topics in Power Electronics, IEEE Journal of*, vol. 2, pp. 584–597, Sept 2014.

[48] I. Laakso, A. Hirata, and O. Fujiwara, "Computational dosimetry for wireless charging of an electrical vehicle," in *Electromagnetic Compatibility, Tokyo (EMC'14/Tokyo), 2014 International Symposium on*, pp. 202–205, IEEE, 2014.

[49] P.-P. Ding, L. Bernard, L. Pichon, and A. Razek, "Evaluation of electromagnetic fields in human body exposed to wireless inductive charging system," *Magnetics, IEEE Transactions on*, vol. 50, pp. 1037–1040, Feb 2014.

[50] L. Lu, J. Nadakuduti, and P. Guckian, "Compliance assessment of human exposure from wireless electric vehicle charging system," Dec. 17 2014. US Patent App. 14/574,095.

[51] C. Alexander and M. Sadiku, *Fundamentals of Electric Circuits: Fifth Edition.* McGraw-Hill Higher Education, 2012.

[52] M. Repetto and S. Leva, *Elettrotecnica. Elementi di teoria ed esercizi.* CittàStudi, 2014.

[53] J. Sallan, J. Villa, A. Llombart, and J. Sanz, "Optimal design of ICPT systems applied to electric vehicle battery charge," *Industrial Electronics, IEEE Transactions on*, vol. 56, pp. 2140–2149, June 2009.

[54] A. Pevere, R. Petrella, C. Mi, and S. Zhou, "Design of a high efficiency 22 kW wireless power transfer system for EVs fast contactless charging stations," in *Electric Vehicle Conference (IEVC), 2014 IEEE International*, pp. 1–7, Dec 2014.

[55] W. Li, H. Zhao, J. Deng, S. Li, and C. Mi, "Comparison Study on SS and Double-sided LCC Compensation Topologies for EV/PHEV Wireless Chargers," *Vehicular Technology, IEEE Transactions on*, vol. PP, no. 99, pp. 1–1, 2015.

[56] J. Villa, J. Sallan, J. Sanz Osorio, and A. Llombart, "High-misalignment tolerant compensation topology for ICPT systems," *Industrial Electronics, IEEE Transactions on*, vol. 59, pp. 945–951, Feb 2012.

[57] M. Ibrahim, L. Pichon, L. Bernard, A. Razek, J. Houivet, and O. Cayol, "Advanced modeling of a 2-kW series-series resonating inductive charger for real electric vehicle," *IEEE Transactions on Vehicular Technology*, vol. 64, pp. 421–430, Feb 2015.

[58] U. K. Madawala, M. Neath, and D. J. Thrimawithana, "A Power-Frequency Controller for Bidirectional Inductive Power Transfer Systems," *IEEE Transactions on Industrial Electronics*, vol. 60, pp. 310–317, Jan 2013.

[59] A. Caillierez, D. Sadarnac, A. Jaafari, and S. Loudot, "Dynamic inductive charging for electric vehicle: Modelling and experimental results," in *Power Electronics, Machines and Drives (PEMD 2014), 7th IET International Conference on*, pp. 1–7, April 2014.

[60] H. H. Wu, J. T. Boys, and G. A. Covic, "An AC processing pickup for IPT systems," *IEEE Transactions on Power Electronics*, vol. 25, pp. 1275–1284, May 2010.

[61] N. Mohan, T. Undeland, and W. Robbins, *Power Electronics: Converters, Applications and Design.* And Its Applications, Wiley, 1989.

[62] R. Erickson and D. Maksimovic, *Fundamentals of Power Electronics.* Power electronics, Springer US, 2001.

[63] J. Boys, G. Covic, and A. Green, "Stability and control of inductively coupled power transfer systems," *Electric Power Applications, IEE Proceedings -*, vol. 147, pp. 37–43, Jan 2000.

[64] C.-S. Wang, G. Covic, and O. Stielau, "Power transfer capability and bifurcation phenomena of loosely coupled inductive power transfer systems," *Industrial Electronics, IEEE Transactions on*, vol. 51, pp. 148–157, Feb 2004.

[65] M. Budhia, G. A. Covic, and J. T. Boys, "Design and optimization of circular magnetic structures for lumped inductive power transfer systems," *IEEE Transactions on Power Electronics*, vol. 26, pp. 3096–3108, Nov 2011.

[66] X. del Toro García, J. Vázquez, and P. Roncero-Sánchez, "Design, implementation issues and performance of an inductive power transfer system for electric vehicle chargers with series–series compensation," *IET Power Electronics*, vol. 8, no. 10, pp. 1920–1930, 2015.

[67] A. Bucher and T. Duerbaum, "Analysis and design of a contactless power transmission system based on the extended first harmonic approximation," in *Industry Applications Society Annual Meeting (IAS), 2012 IEEE*, pp. 1–7, IEEE, 2012.

[68] S.-H. Lee and R. D. Lorenz, "Development and validation of model for 95%-efficiency 220-W wireless power transfer over a 30-cm air gap," *Industry Applications, IEEE Transactions on*, vol. 47, no. 6, pp. 2495–2504, 2011.

[69] J. J. Casanova, Z. N. Low, and J. Lin, "Design and optimization of a class-E amplifier for a loosely coupled planar wireless power system," *Circuits and Systems II: Express Briefs, IEEE Transactions on*, vol. 56, no. 11, pp. 830–834, 2009.

[70] D. Kürschner, C. Rathge, and U. Jumar, "Design methodology for high efficient inductive power transfer systems with high coil positioning flexibility," *Industrial Electronics, IEEE Transactions on*, vol. 60, no. 1, pp. 372–381, 2013.

[71] M. Ghovanloo and S. Atluri, "A wide-band power-efficient inductive wireless link for implantable microelectronic devices using multiple carriers," *Circuits and Systems I: Regular Papers, IEEE Transactions on*, vol. 54, no. 10, pp. 2211–2221, 2007.

[72] K. Tomita, R. Shinoda, T. Kuroda, and H. Ishikuro, "1-W 3.3–16.3-V boosting wireless power transfer circuits with vector summing power controller," *Solid-State Circuits, IEEE Journal of*, vol. 47, no. 11, pp. 2576–2585, 2012.

[73] V. Cirimele, F. Freschi, and P. Guglielmi, "Wireless power transfer structure design for electric vehicle in charge while driving," in *Electrical Machines (ICEM), 2014 International Conference on*, pp. 2461–2467, Sept 2014.

[74] C. Desoer and E. Kuh, *Basic Circuit Theory.* McGraw-Hill Education, 2009.

[75] C. B. Aiken, "Two-mesh tuned coupled circuit filters," *Proceedings of the Institute of Radio Engineers*, vol. 25, pp. 230–272, Feb 1937.

[76] A. Liberatore and A. Stianti, *Manuale Cremonese di meccanica, elettrotecnica, elettronica (1) - Manuale Cremonese di elettrotecnica.* Cremonese, 1999.

[77] F. Terman, *Radio Engineer's Handbook.* McGraw-Hill handbooks, McGraw-Hill Book Company, Incorporated, 1943.

[78] "ISO 18164:2005 Passenger car, truck, bus and motorcycle tyres – Methods of measuring rolling resistance." http://www.iso.org/iso/catalogue_detail.htm?csnumber=33328. Accessed in October 2016.

[79] S. de Technologie Michelin, "System and method for transferring electric energy to a vehicle," 2003.

[80] J. Y. Wong, *Theory of Ground Vehicles.* Wiley-Interscience, 3 ed., 2001.

[81] G. Fontaras and Z. Samaras, "On the way to 130 g CO2/km - Estimating the future characteristics of the average European passenger car," *Energy Policy*, vol. 38, no. 4, pp. 1826 – 1833, 2010.

[82] F. Kost, "Basic principles of vehicle dynamics," in *Fundamentals of Automotive and Engine Technology*, pp. 114–129, Springer, 2014.

[83] F. Deflorio, P. Guglielmi, I. Pinna, L. Castello, and S. Marfull, "Modeling and Analysis of Wireless "Charge While Driving" Operations for Fully Electric Vehicles," *Transportation Research Procedia*, vol. 5, pp. 161–174, 2015.

[84] E. Gati, G. Kampitsis, and S. Manias, "Variable frequency controller for inductive power transfer in dynamic conditions," *IEEE Transactions on Power Electronics*, vol. PP, no. 99, pp. 1–1, 2016.

[85] J. M. Miller, O. C. Onar, and M. Chinthavali, "Primary-side power flow control of wireless power transfer for electric vehicle charging," *IEEE Journal of Emerging and Selected Topics in Power Electronics*, vol. 3, pp. 147–162, March 2015.

[86] T. Diekhans and R. W. D. Doncker, "A dual-side controlled inductive power transfer system optimized for large coupling factor variations and partial load," *IEEE Transactions on Power Electronics*, vol. 30, pp. 6320–6328, Nov 2015.

[87] B. Singh, B. N. Singh, A. Chandra, K. Al-Haddad, A. Pandey, and D. P. Kothari, "A review of three-phase improved power quality AC-DC converters," *IEEE Transactions on Industrial Electronics*, vol. 51, pp. 641–660, June 2004.

[88] D.-C. Lee, G.-M. Lee, and K.-D. Lee, "DC-bus voltage control of three-phase AC/DC PWM converters using feedback linearization," *IEEE Transactions on Industry Applications*, vol. 36, no. 3, pp. 826–833, 2000.

[89] J. Shin, S. Shin, Y. Kim, S. Lee, B. Song, and G. Jung, "Optimal current control of a wireless power transfer system for high power efficiency," in *2012 Electrical Systems for Aircraft, Railway and Ship Propulsion*, 2012.

[90] R. Fosler, "PSoC®3 and PSoC 5LP - Phase-Shift Full-Bridge Modulation and Control - Application Note AN76439." http://www.cypress.com/file/121286/download, 2013. Accessed in October 2016.

[91] Z. Emami, M. Nikpendar, N. Shafiei, and S. R. Motahari, "Leading and lagging legs power loss analysis in ZVS Phase-Shift Full Bridge converter," in *Power Electronics, Drive Systems and Technologies Conference (PEDSTC), 2011 2nd*, pp. 632–637, Feb 2011.

[92] M. Petersen and F. W. Fuchs, "Development of a 5 kW Inductive Power Transfer System Including Control Strategy for Electric Vehicles," in *PCIM Europe 2014; International Exhibition and Conference for Power Electronics, Intelligent Motion, Renewable Energy and Energy Management; Proceedings of*, pp. 1–8, 2014.

[93] P. Ning, J. M. Miller, O. C. Onar, C. P. White, and L. D. Marlino, "A compact wireless charging system development," in *2013 Twenty-Eighth Annual IEEE Applied Power Electronics Conference and Exposition (APEC)*, 2013.

[94] STMicroelectronics, "MOSFET body diode recovery mechanism in a phase-shifted ZVS full bridge DC/DC converter - Application Note AN 2626." http://www.ti.com/lit/an/slua159/slua159.pdf, 2007. Accessed in October 2016.

[95] A. Huang, "Hard Commutation of Power MOSFET - Application Note AN 2014-03." http://www.ti.com/lit/an/slua159/slua159.pdf, 2014. Accessed in October 2016.

[96] B. Andreycak, "Zero Voltage Switching Resonant Power Conversion - Application Note U-138." http://www.ti.com/lit/an/slua159/slua159.pdf, 1999. Accessed in October 2016.

[97] S. Keeping, "A Review of Zero-Voltage Switching and its Importance to Voltage Regulation." http://www.digikey.it/en/articles/techzone/2014/aug/a-review-of-zero-voltage-switching-and-its-importance-to-voltage-regulation, 2014. Accessed in October 2016.

[98] Y. Cui, M. Chinthavali, and L. M. Tolbert, "Temperature dependent Pspice model of silicon carbide power MOSFET," in *2012 Twenty-Seventh Annual IEEE Applied Power Electronics Conference and Exposition (APEC)*, pp. 1698–1704, IEEE, 2012.

[99] G. Ortiz, C. Gammeter, J. Kolar, and O. Apeldoorn, "Mixed MOSFET-IGBT bridge for high-efficient medium-frequency dual-active-bridge converter in solid state transformers," in *Control and Modeling for Power Electronics (COMPEL), 2013 IEEE 14th Workshop on*, pp. 1–8, IEEE, 2013.

[100] K. F. Hoffmann and J. P. Karst, "High frequency power switch-improved performance by MOSFETs and IGBTs connected in parallel," in *Power Electronics and Applications, 2005 European Conference on*, pp. 11–pp, IEEE, 2005.

[101] M. L. G. Kissin, C. Y. Huang, G. A. Covic, and J. T. Boys, "Detection of the Tuned Point of a Fixed-Frequency LCL Resonant Power Supply," *IEEE Transactions on Power Electronics*, vol. 24, pp. 1140–1143, April 2009.

[102] I. Josifović, J. Popović-Gerber, and J. A. Ferreira, "Improving SiC JFET Switching Behavior Under Influence of Circuit Parasitics," *IEEE Transactions on Power Electronics*, vol. 27, pp. 3843–3854, Aug 2012.

[103] V. Cirimele, S. G. Rosu, P. Guglielmi, and F. Freschi, "Performance evaluation of wireless power transfer systems for electric vehicles using the opposition method," in *Research and Technologies for Society and Industry Leveraging a better tomorrow (RTSI), 2015 IEEE 1st International Forum on*, pp. 546–550, Sept 2015.

[104] C. Turpin, F. Richardeau, T. Meynard, and F. Forest, "Evaluation of high power converters by the opposition method," *EPE Journal*, vol. 12, no. 1, pp. 26–32, 2002.

[105] F. Forest, J.-J. Huselstein, S. Faucher, M. Elghazouani, P. Ladoux, T. Meynard, F. Richardeau, and C. Turpin, "Use of opposition method in the test of high-power electronic converters," *IEEE Transactions on Industrial Electronics*, vol. 53, no. 2, pp. 530–541, 2006.

[106] I. Widjaja, A. Kurnia, D. Divan, and K. Shenai, "Conductivity modulation lag during IGBT turn on in resonant converter applications," in *Device Research Conference, 1994. 52nd Annual*, pp. 35–36, 1994.

[107] P. Ranstad and H. P. Nee, "On Dynamic Effects Influencing IGBT Losses in Soft-Switching Converters," *IEEE Transactions on Power Electronics*, vol. 26, pp. 260–271, Jan 2011.

[108] P. Ranstad, H. P. Nee, J. Linnér, and D. Peftitsis, "An Experimental Evaluation of SiC Switches in Soft-Switching Converters," *IEEE Transactions on Power Electronics*, vol. 29, pp. 2527–2538, May 2014.

[109] J. Shin, S. Shin, Y. Kim, S. Ahn, S. Lee, G. Jung, S. J. Jeon, and D. H. Cho, "Design and implementation of shaped magnetic-resonance-based wireless power transfer system for roadway-powered moving electric vehicles," *IEEE Transactions on Industrial Electronics*, vol. 61, pp. 1179–1192, March 2014.

[110] M. Yilmaz, V. T. Buyukdegirmenci, and P. T. Krein, "General design requirements and analysis of roadbed inductive power transfer system for dynamic electric vehicle charging," in *2012 IEEE Transportation Electrification Conference and Expo (ITEC)*, pp. 1–6, June 2012.

[111] A. Caillierez, P. A. Gori, D. Sadarnac, A. Jaafari, and S. Loudot, "2.4 kW prototype of on-road wireless power transfer: Modelling concepts and practical implementation," in *Power Electronics and Applications (EPE̒15 ECCE-Europe), 2015 17th European Conference on*, pp. 1–9, Sept 2015.

[112] "Car dimensions of any make and model in the European market with the photo of each automobile size showing length, width and height." http://www.automobiledimension.com/. Accessed in October 2016.

[113] E. B. Rosa and F. W. Grover, *Formulas and tables for the calculation of mutual and self-inductance*. No. 169, US Government Printing Office, 1948.

[114] C. Paul, *Inductance: Loop and Partial*. Wiley, 2011.

[115] "Litz Wire and Formed Cables — New England Wire Technologies." http://www.newenglandwire.com/products/litz-wire-and-formed-cables/. Accessed in October 2016.

[116] "Litz Wire." https://en.wikipedia.org/wiki/Litz_wire. Accessed in October 2016.

[117] S. H. Lee and R. D. Lorenz, "Development and Validation of Model for 95%-Efficiency 220-W Wireless Power Transfer Over a 30-cm Air Gap," *IEEE Transactions on Industry Applications*, vol. 47, pp. 2495–2504, Nov 2011.

[118] M. Scudiere and J. McKeever, "Wireless power transfer for electric vehicles," tech. rep., SAE Technical Paper, 2011.

[119] J. Frankeny, R. Frankeny, J. Haj-ali Ahmadi, K. Hermann, and R. Imken, "High density interconnect strip," Aug. 6 1991. US Patent 5,037,311.

[120] A. Canova, F. Freschi, M. Repetto, and M. Tartaglia, "Description of power lines by equivalent source system," *COMPEL-The international journal for computation and mathematics in electrical and electronic engineering*, vol. 24, no. 3, pp. 893–905, 2005.

[121] D. Dunavant, "High degree efficient symmetrical gaussian quadrature rules for the triangle," *International journal for numerical methods in engineering*, vol. 21, no. 6, pp. 1129–1148, 1985.

[122] B. A. Szabo and I. Babuška, *Finite element analysis*. John Wiley & Sons, 1991.

[123] "MatWeb - Material property data." http://matweb.com/. Accessed in October 2016.

[124] ICNIRP, "Guidelines for limiting exposure to time-varying electric and magnetic fields (1 Hz to 100 kHz)," *Health Phys*, vol. 99, no. 6, pp. 818–836, 2010.

[125] R. Storn and K. Price, *Differential Evolution - A simple and efficient adaptive scheme for global optimization over continuous spaces*, vol. 3. International Computer Science Institute Berkeley, 1995.

[126] P. G. Alotto, C. Eranda, B. Brandstatter, G. Furntratt, C. Magele, G. Molinari, M. Nervi, K. Preis, M. Repetto, and K. R. Richter, "Stochastic algorithms in electromagnetic optimization," *IEEE Transactions on Magnetics*, vol. 34, no. 5, pp. 3674–3684, 1998.

[127] V. Arunachalam, *Optimization Using Differential Evolution*. Department of Civil and Environmental Engineering, The University of Western Ontario, 2008.

[128] D. Meeker, "Finite Element Method Magnetics, Version 4.2." http://www.femm.info/wiki/HomePage. Accessed in November 2016.

[129] "COMSOL website." https://www.comsol.it/. Accessed in Novemeber 2016.

[130] S. Babic, C. Akyel, and S. Salon, "New procedures for calculating the mutual inductance of the system: filamentary circular coil-massive circular solenoid," *Magnetics, IEEE Transactions on*, vol. 39, pp. 1131–1134, May 2003.

[131] L. Krahenbuhl and D. Muller, "Thin layers in electrical engineering-example of shell models in analysing eddy-currents by boundary and finite element methods," *IEEE Transactions on Magnetics*, vol. 29, no. 2, pp. 1450–1455, 1993.

[132] V. Cirimele, F. Freschi, L. Giaccone, and M. Repetto, "Finite formulation of surface impedance boundary conditions," *IEEE Transactions on Magnetics*, vol. 52, no. 3, pp. 1–4, 2016.

[133] W. Zhang, J. C. White, A. M. Abraham, and C. C. Mi, "Loosely coupled transformer structure and interoperability study for ev wireless charging systems," *IEEE Transactions on Power Electronics*, vol. 30, no. 11, pp. 6356–6367, 2015.

[134] M. Mitolo, *Electrical Safety of Low-Voltage Systems.* McGraw-Hill Education, 2009.

[135] R. Ruffo, V. Cirimele, P. Guglielmi, and M. Khalilian, "A coupled mechanical-electrical simulator for the operational requirements estimation in a dynamic IPT system for electric vehicles," in *2016 IEEE Wireless Power Transfer Conference (WPTC)*, pp. 1–4, May 2016.

[136] C. Szász and G. Husi, "Novel multimodal communication skills implementation on the ni-9631 robot," in *Industrial Electronics Society, IECON 2013 - 39th Annual Conference of the IEEE*, pp. 7837–7842, Nov 2013.

[137] G. Husi, P. T. Szemes, E. Dávid, and T. I. Erdei, "Development of simulation and research toolset for domestic energy utilization," in *Energy (IYCE), 2013 4th International Youth Conference on*, pp. 1–7, June 2013.

[138] M. Marzouk, J. P. Ferrieux, D. Frey, and B. Sarrazin, "A shared traction drive and battery charger modes for Plug-In Hybrid Electric Vehicle application," in *Power Electronics and Applications (EPE'14-ECCE Europe), 2014 16th European Conference on*, pp. 1–10, Aug 2014.

[139] "HIOKI LCR HiTESTER 3532-50 - Instruction manual," 2015.

[140] "Technical guide - The MV/LV transformer substations (passive users)," 2015.

[141] K. Jokela, "Restricting exposure to pulsed and broadband magnetic fields.," *Health Physics*, vol. 79, no. 4, pp. 373–388, 2000.

[142] ICNIRP, "Guidance on determining compliance of exposure to pulsed and complex non-sinusoidal waveform below 100 kHz with ICNIRP guidelines," *Health Phys*, vol. 84, no. 3, pp. 383–387, 2003.

[143] A. Canova, G. Gruosso, and M. Repetto, "Integral methods for analysis and design of low-frequency conductive shields," *IEEE transactions on magnetics*, vol. 39, no. 4, pp. 2009–2017, 2003.

[144] A. Christ, W. Kainz, E. G. Hahn, K. Honegger, M. Zefferer, E. Neufeld, W. Rascher, R. Janka, W. Bautz, J. Chen, *et al.*, "The Virtual Family–development of surface-based anatomical models of two adults and two children for dosimetric simulations," *Physics in medicine and biology*, vol. 55, no. 2, p. N23, 2009.

[145] A. Canova, F. Freschi, L. Giaccone, and M. Repetto, "Exposure of Working Population to Pulsed Magnetic Fields," *IEEE Transactions on Magnetics*, vol. 46, pp. 2819–2822, Aug 2010.

[146] "ELT 400 Product page web site." https://www.narda-sts.com/en/emc-products/elt-400/. Accessed in Novemeber 2016.

[147] C. P.P., *Elettrotecnica Tomo I seconda edizione*, vol. 1. Levrotto & Bella, 2005.